The Flow Development in Jet-Driven Vortex Chambers

Ali Jawarneh

A Thesis

in

The Department

of

Mechanical and Industrial Engineering

Presented in Partial Fulfillment of the Requirements

for the Degree of Doctor of Philosophy at

Concordia University

Montreal, Quebec, Canada

July 2004

Your file Votre référence
ISBN: 0-612-96961-4
Our file Notre référence
ISBN: 0-612-96961-4

ABSTRACT

The Flow Development in Jet-Driven Vortex Chambers

Ali Jawarneh, Ph.D.

Concordia University, 2004

This work presents the study of the flow in a jet-driven vortex chamber over a wide range of Reynolds numbers, contraction ratios, inlet angles, area and aspect ratios. Dimensional analysis furnishes the general functional relationships between the fundamental dimensionless quantities. Application of the integral equations of continuity and energy over the control volume, along with the minimum-pressure-drop or maximum flow rate postulate, provide the required analytical means to relate the predominant non-dimensional parameters such as the chamber geometry, the core size, pressure drop, Reynolds number, and viscous losses. Both the n=2 vortex model, with reverse and non-reverse flow, and the free vortex model have been used at the vortex chamber exit plane. The theoretical results are found to successfully capture most of the salient properties of the flow. The influence of vortex chamber geometry, such as contraction ratio, inlet angle, area ratio, aspect ratio, and Reynolds number, on the flow field has been analyzed and compared with the present experimental data. A parametric study explores how the pressure coefficient and the core size vary with the different dimensionless properties. The observations show the pressure drop to decrease with the length. At first this appears to be counterintuitive since one habitually expects the pressure drop to be larger for

longer pipes. A closer examination however, reveals that in addition to the radial-axial plane flow there is also a substantial centrifugal force, which decays with the length, thus shaping the development of the overall flow-field. The pressure drop across the vortex chamber differs from that in pipe flow, due to the mechanism of swirl flow. It depends mainly on intensity of tangential velocity. If the chamber length is increased, the vortex decay factor decreases, which leads to less pressure drop. The current theory confirms that the previous published models are only applicable for high Reynolds numbers where the inertia dominates the viscous forces. Based on the present theory, a new approach to determine the tangential velocity and radial pressure profiles inside the vortex chamber is developed and compared with the available experimental data. The n=2 vortex model with reverse flow gives better results for strongly swirling flow.

Acknowledgments

All praises are due to Allah, we praise Him, seek His Aid and beg for His Forgiveness.

I would like to express my deepest gratitude and appreciation to Dr. Vatistas and Dr. Hong who have helped in putting this thesis together with knowledge, helpful comments, wisdom, technical help, supplies, and finances.

This work would not have been possible without the kindness, patience, and assistance of many people. I would like to thank those who encourage me and were kind enough during my study, especially my wife Lana, my children Mohammad and Nada, my father, my mother, my sisters, my brothers and my friends.

Thanks to the people in the Mechanical and Industrial Engineering Department for helping and assistance to facilitate the research.

CONTENTS

List of Figures

Nomenclature

A_{axial}	axial inertial term
A_o	cross sectional area of the vortex chamber
A_{in}	total inlet area
C_p	pressure coefficient ($2\,\Delta P / \rho q_{in}^2$)
D_e	diameter of the exit port ($2\,R_e$)
D_h	hydraulic diameter
D_{in}	diameter of the inlet port
D_o	chamber diameter ($2\,R_o$)
$F_{friction}$	fricrtion term
k	specific heat ratio
L	chamber length
P	static pressure
P_{in}	static pressure at the inlet
P_a	ambient static pressure
Q_{in}	inlet volumetric flow rate
Q_{out}	outlet volumetric flow rate
Q_{rev}	reverse volumetric flow rate
q_{in}	total velocity vector at the inlet
r, θ, z	radial, tangential and axial coordinate respectively

$\bar{r}$ normalized radius (r / R_o)

R gas constant

R_c core radius

R_e radius of exit port

R_{eo} Reynolds number ($R_{eo} = \frac{4Q_{in}}{\nu \pi D_o}$)

R_o radius of the chamber

S swirl number

S_{swirl} swirl term

T temperature

V_{cin} vortex strength at the inlet ($V_{cin} = \frac{\Gamma}{2\pi R_c}$)

V_{cout} vortex strength at the outlet ($V_{cout} = \delta V_{cin}$)

V_{zout} axial velocity component at exit

V_{zrev} reverse axial velocity

V_r, V_θ, V_z radial, tangential and axial velocity components

$V_{\varphi in}$ inlet tangential velocity component

Greek Symbols

α area ratio (A_{in} / A_o)

γ_1 reverse volumetric fraction

γ_2 outlet volumetric fraction

Γ vortex circulation

ΔP static pressure difference ($P_{in} - P_a$)

$\Delta \overline{P}$ radial pressure $\left(\frac{2[p(\bar{r}) - p_a]}{\rho q_{in}^2} \right)$

δ vortex decay factor

κ_{in} vortex strength at the inlet ($R_o V_{\varphi in}$)

κ_{out} vortex strength at the outlet ($\delta R_o V_{\varphi in}$)

Π radial pressure $\left(\frac{2[p(\bar{r}) - p_{wall}]}{\rho q_{in}^2} \right)$

υ kinematics viscosity

ρ density of the fluid

σ effective outlet area $\left(\frac{1 - \chi^2}{\xi^2} \right)$

φ angle between the total velocity vector and the tangential velocity component at the inlet (inlet angle)

χ dimensionless core size at exit (R_c / R_e)

χ_o dimensionless core size (R_c / R_o)

ζ aspect ratio (L / D_o)

ξ diameter ratio (D_o / D_e)

Chapter 1: Introduction

1-1: General

The vortices are present in several natural phenomena such as, dust-devil, tornadoes, fire whirls and water spouts. The advantageous properties of swirling flow in cylindrical confinements have long been put into use in several technological devices and industrial processes. Most notable of them include vortex separators [1], Ranque-Hilsh vortex tube [2], pumps, gas turbine combustors, incinerators, furnaces, the spray dryer, the liquid atomizer, the vortex valve, the vortex combustor [3], and gas-core nuclear rocket. In the range of intermediate aspect ratios (length/ diameter), the vortex separator is one of the most widespread of the applications. The vortex combustor [3] can provide easy ignition, efficient and stable combustion and low level of emissions for a wide range of air to fuel ratios. In furnaces and incinerators, swirl keeps the solid fuel in suspension, increases its residence time, and compels to burn completely even the most difficult (low calorific value) fuel. Energy separation can be achieved in vortex tubes. The vortex valve has been used in fluidics, as means to prevent floods, and as flow rate sensors. The supporting effects of swirling fluid motion have also found applications in magneto-hydrodynamic power generation and the stabilization of electric arcs. In addition vortex tubes have become the laboratory tool to study the phenomenon of vortex-breakdown and to examine the main properties of high Rossby number geophysical vortices. The general area is also of value to ion flow dynamics, low temperature physics, and to several other related fields. The plethora of journal articles, monographs, and industrial/laboratory

reports on the subject has shown this area to be under continuous scientific scrutiny since the late 1940's.

Problems of heat and mass transfer in swirl flows are practical important in designing different heat and mass transfer exchangers, submerged burners, heat transfer promoters and chemical reactors. Better utilization of swirl flows may lead to the heat and mass transfer enhancements, see Martemianov [4 and 5], Algifri [6], Legentilhomme [7] and De Sa et al. [8].

The presence of the vortex is an essential element for the proper operation, but in others, its presence reduces the efficiency of the equipment and produces vibration and noise. For instance, vortices generated in the intakes of liquid pump, draft tubes of water turbines, weirs, draining of reservoirs and in the case of trailing vortices those resulting from helicopter blades.

Fluid vortices can be of different sizes, shapes, and strengths. Their size ranges from the smallest turbulent eddy to planetary vortices. Depending on their aspect ratio (radius of maximum tangential velocity/height) they may assume a disk- or a columnar-like shape. Vortices that have most of the axial vortices component residing within their core are known as concentrated vortices. If a tangential velocity is several orders of magnitude larger than the radial and axial components they may be called intense or strong vortices.

The bulk of experimental work has dealt primarily with specific applications. Consequently, the data are restricted to the geometry and flow conditions of the individual study. The main obstacle to reliably compare results is the lack of lucid rules with which dynamic similarity among flows can be secured. The experimental studies can be divided into two categories; those directed towards the characterization of the overall flow behavior concentrating on the pressure drop and flow rate through the device, meanwhile the other is aimed at the elaboration of the internal flow structure. Tests to explain the flow features include visualizations, pitot-probe, hot wire, as well as Laser Doppler Anemometer (LDA) measurements. Yet the experimental side of the problem is not free from impediments. Intrusive measuring techniques tend to slowdown the vortex thus altering the flow structure [9]. The visualization on the other hand can only be limited to low Reynolds numbers because the tracer particles at high flow rates are prone to diffusion producing a fussy picture of the flow field. Due to centrifugal instability and depending on the flow conditions, vortices are known to host a variety of waves [10,11]. These are generated near the axis of rotation and are then are diffused outwards. The last action modulates the main flow properties, in the vicinity of axis of rotation, causing a temporal variation. Consequently, the location of the vortex center may vary significantly with time. If this is the case, even the LDA data will not provide the actual magnitude of the tangential velocity but rather an averaged value.

1-2: The problem

In confined vortices, it is important to understand the swirling flow properties and the geometrical parameters of the swirl devices in order to design or improve the performances of the vortex devices. One of the most important operational characteristics in vortex chambers is the pressure drop and aim of the vortex chamber designer is to produce swirl with minimum pressure drop.

The theoretical analysis of vortex flow is extremely difficult, and relatively little progress has been made. Capturing the flow details requires solution of full Navier-Stokes equations, the complexities associated mainly with the unknown boundary conditions and the high non-linearity of these equations.

The physics of strongly vortex flows, particularly the confined type, are theoretically cumbersome since in addition to the usual forces they also include a powerful centrifugal acceleration and complex boundary conditions (often times unknown), which exacerbate the situation. These complications have prevented analytical, or even numerical solutions able to capture the physics adequately. For this reason the majority of the theoretical studies have been limited on either simple solutions of the equations of motion, or numerical flow descriptions using very approximate exit boundary conditions.

Closed-form solutions for vortex flows can only be obtained by further simplifying the governing equations. Several semi-empirical models (Rankine 1858, Oseen-Lamb 1932,

Burgers 1948, etc) have been developed to explore the vortex flow. However, the above models yield only the radial distribution of the tangential component of a velocity vector and the axial component does not depend on the radius, which is inconsistent with the numerous experimental data.

1-3: Vortex Chamber Flow

It is well known that, the tangent velocity of the confined fluid changes from free to forced vortex as the flow approaches the axis of rotation and the confined fluid with sufficient swirl, its pressure inside the core may be below the ambient pressure. The reverse flow, which takes place in the vortex core is attributed to a local static pressure reduction to values that are below the ambient pressure.

Vortex chambers in general have a cylindrical configuration with a centrally located outlet located on the top or the bottom plate. Fluid entering the tube acquires swirl via either; (i) inlets placed tangentially around the circumferential wall, (ii) rotation of a porous wall, or (iii) admission through radial or axial vanes. The inlet(s) may be located near the top plate, the opposite end, both, or cover the entire length of the chamber. Both inlet(s) with rectangular or circular cross-section(s) have been used in the past. The present paper will focus on jet driven vortex chambers, i.e. case (i).

The swirling motion, imparted to the fluid by the inlet ports, generates a strong centrifugal force –field which gives rise to the complex flow-pattern of figure (1-3-1) which is taken from reference [12].

As the fluid enters the vortex chamber it immediately faces a strong centrifugal force. In its attempt to find paths to the exit with a minimum opposition it divides itself into two streams. The first propagates along the circumferential wall where the centrifugal force is constant, and is then directed to the outlet at a point near the top plate. The second, flows towards the center through the bottom plate. In both plates the presence of Ekman's boundary layers reduce the velocity thus diminishing the centrifugal force. Because the path through the top plate the tangential velocity has undergone decay it presents the least centrifugal opposition of the two streams. Consequently the first stream is stronger than the second. A large toroidal recirculation flow area that exists between the exit radius and the cylindrical wall (see Baluev and Troyankin [12], Georgantas et al [13], Escudier et al [14]) attributes its origin to Taylor-Göertler instability. However, a recent study by Mattner et al [15] indicated otherwise. Depending on flow conditions and chamber geometry, the axial velocity near the core could develop a distribution resembling that of a pure jet, a jet-like with a velocity deficit at the axis of rotation, or even a wake-like profile. The latter flow state is characterized by the development of an entrained flow.

However, the static pressure in this region has dropped below the pressure of the exterior to the chamber ambient air, and the induced reverse flow, forces the stream to reach the outlet at a larger radius. The reverse flow taking place in the vortex core is already

attributed to the static pressure reduction within the chamber to values which are below the ambient.

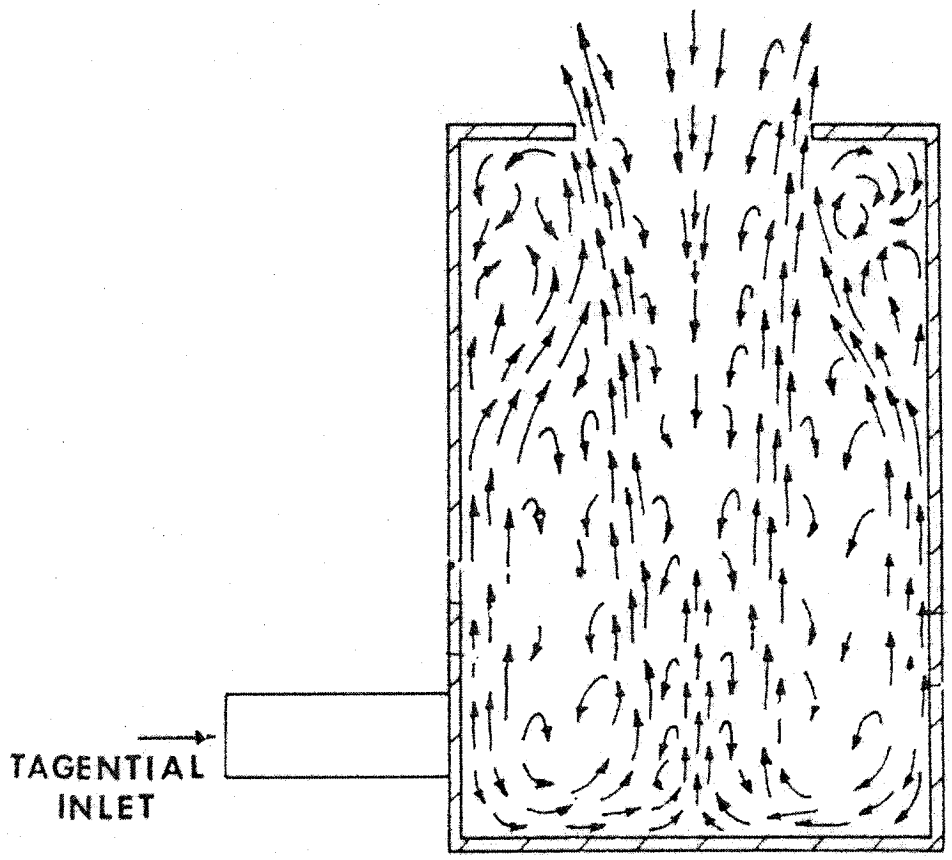

Figure (1-3-1): Flow pattern in a vortex chamber [12]

1-4: Literature Survey

The most elementary of vortex model is by Rankine [16]. This model assumes a linear tangential velocity distribution inside the core, with a hyperbolic variation outside the core, the discontinuity of the velocity derivatives at the point of transition from free to forced mode and the overestimation of the velocity near the core, have led many to seek better approximation. In addition, both the radial and axial velocities are required to be zero. Scully [19] proposed an empirical tangential-velocity distribution, where the model simulates the effects of viscosity near the core and assumes no zero radial and axial velocity components. However, his model underestimates most of the measured values of the tangential velocity near the core. Burgers [18] vortex model improves on the correlation between the observed and predicted values for the tangential velocity, but assumes a linear profile for the radial velocity and a constant axial velocity. Lamb [20] model is a solution to the one-dimensional laminar Navier-Stokes equation, with the assumption that viscous vortex core on the basis of several models, the axial and radial velocities are zero.

Vatistas [21] reported a model for single- or double-celled intense vortices, depending on the values of scaling constants. It was shown that the axial velocity component may attain profiles ranging from jet-like to wake-like. Sullivan [22] proposed a two-celled vortex characterized by a direction reversal of the radial and axial velocity components near the axis of rotation.

Two interesting features of the flow of practical importance are the pressure drop of the fluid as it flows through the chamber and the dimensions of the viscous core region. The pressure drop across vortex chamber has been the subject of several papers [23-26].

The early studies of Binnie and Hookings [27] focused on the discharge of water through trumpet-shaped circular weirs. Lewellen [25] utilized the maximum flow rate hypothesis to determine the core size. Shakespear and Levy [28] reported on experimental findings with respect to the pressure drop and the core size in a vortex chamber with a rotating permeable inlet assuming a potential flow. Their analytical development veers away from the last hypothesis and unfortunately creates a theoretical contradiction. Vatistas et al [26,29] used also the extremum assumption to analyze the flow inside vortex chambers. Vatistas [30] has shown experimentally the pressure drop across the chamber can be reduced by preventing the stagnant air from entering the chamber using conical plug and conical plug with diffuser. The most recent work by Vatistas [31] has examined the static pressure drop across a vortex chamber with two outlets. The theory suggests that the flow is controlled by the larger diameter exit, where the axial velocity at the exit was assumed constant outside the core regime. Vyas [32] has shown analytically that the pressure drop and the core size are function of the aspect ratio and Reynolds number. Li [33] has demonstrated experimentally the decay of swirl and the pressure distributions along a smooth pipe with high aspect ratio ζ =162 , using a three-holed spherical-head probe to measure the axial, tangent velocities and pressure profiles at different pipe sections, Reynolds number and inlet swirlers. The characteristics of swirling flow are function of swirl number, Reynolds number and the aspect ratio. Yang [34] has studied the vortex

throttles, and has found that the pressure drop across the vortex throttles occurs through the axial throttling port by the dissipation of the high tangential velocity. Escudier et al [35] demonstrated experimentally the axial and swirl velocities distributions using LDA measurements. The experiments were performed with water at $\zeta = 3.8$ for a range of exit diameters between ξ=1 to 5.5. The experiments revealed a remarkable change in the vortex structure as the exit diameter is reduced, where the vortex core size changes from a thick core to a thin core. In addition, the axial velocity is able to develop profiles ranging from jet-like to wake-like shapes.

Kreith [36] studied the decay of swirl in a long pipe. The swirl was induced by tangential jets along the periphery of the pipe. The experiments indicated that the vortex decay increases as the Reynolds number decreases.

The vortex flow field in a tube has been experimentally studied by Chang [37]. The experiments were conducted by injecting air through four injectors placed on the periphery of vortex tube with aspect ratio equal to 17. The swirl intensity decays as the axial distance from the injection location increases. The axial velocity profile shows the existence of a flow reversal region in the central portion of the tube and an increased axial velocity near the wall. The tangential velocity profiles have a local maximum, and the location of which moves radially inwards with distance.

The core size structure inside a vortex chamber has a wavy variation, see Darmofal et al [38]. Meanwhile the core structure based on Laser Doppler Anemometry (LDV)

measurements of Escudier [39, 40] confirm that the variations are very small. In addition, the visualization experimental results of Lam [41] and Alekseenko et. al [42] showed that the core of the vortex remains approximately the same throughout the chamber, and the amplitude of the oscillations was found to be small in comparison with the size of the vortex core.

Love [43] indicated that the energy losses observed for swirling flow can be orders of magnitude greater than that computed for comparable nonswirling flow. The losses are explained due not only to the decay of the swirl, but also as a function of the axial flow area restriction caused by the swirl induced recirculating core.

Osami [44] has shown experimentally that the swirl intensity decays downstream as a result of wall friction and the reverse flow appears at the centre when the swirl intensity is high. The core size is dependent upon the upstream conditions in the annular region. The skewness of the velocity vector is noticeable and highly anisotropic so that the turbulent viscosity model does not work well here. Steenbergen [45] has shown that the vortex decay appears to vary with the Reynolds number in the same way as the friction factor in a pipe flow.

Nejad [46] showed that the $k-\varepsilon$ turbulent model is inadequate for representing the complex turbulent structure of confined swirling flows, where the reason may be due to severe bending of streamlines. Jakirlic [47] has shown numerically using three versions of the second-momentum closure and two eddy-viscosity models that the second-

momentum models are superior. However, challenges still remain in predicting accurately some specific flow features, such as capturing the transition from a free vortex to solid-body rotation in a swirl pipe, or reproducing the normal stress components in the core region. Flow in vortex chamber at low Reynolds number using direct numerical simulations was investigated by Orland [48]. Jones [49] and Hoekstra et al [50] used the $k-\varepsilon$ turbulent model and a Reynolds stress transport equation model of a strong confined swirling flow. A comparison of the results with measurement shows the superiority of the transport equation model, where $k-\varepsilon$ gave large discrepancies between the measured and calculated mean velocity field. Therefore, the experimental approach is still a most suitable method for studying the confined vortex flow structure.

As seen from the literature, there is no comprehensive study to explore the effects of all vortex chamber parameters. They are: aspect ratio (ζ), diameter ratio (ξ), area ratio (α), swirl angle (φ), and Reynolds number (R_{eo}) on the pressure drop and the core size. The purpose of this thesis is to study the pressure drop and the core size experimentally and analytically in a flow having different vortex chamber parameters and different Reynolds numbers. In addition, the tangential velocity and the radial pressure profiles can be obtained, since the core size and the circulation are given.

1-5: The Study and New Findings

This work introduces experimental and theortical study of the flow in a jet-driven vortex chamber over a wide range of Reynolds numbers, contraction ratios, aspect ratios, inlet angles, and area ratios. Dimensional analysis establishes the functional relationships between the fundamental dimensionless quantities.

The integral approach of continuity and energy equations, along with the minimum-pressure-drop or maximum flow rate, are used in this study to provide an analytical means to relate the non-dimensional parameters such as the chamber geometry, core size, pressure drop, Reynolds number, and viscous losses.

Both the free vortex model and the n=2 vortex model, with reverse and non-reverse flow have been used at the chamber exit plane. The effect of vortex chamber geometry, such as contraction ratio, inlet angle, area ratio, aspect ratio, and Reynolds number, on the flow field has been analyzed and compared with the present experimental data.

The observations show the pressure drop to decrease with the length. At first this appears to be counterintuitive since one habitually expects the pressure drop to be larger for longer pipes. A closer examination however, reveals that in addition to the radial-axial plane flow there is also a substantial centrifugal force, which decays with the length, thus shaping the development of the overall flow-field. The pressure drop across the vortex

chamber differs from that in pipe flow, due to the mechanism of swirl flow. It depends mainly on the intensity of the tangential velocity. If the chamber length is increased, the vortex decay factor decreases, lowering the tangential velocity, which leads to less pressure drop.

A new approach to determine the tangential velocity and radial pressure profiles inside the vortex chamber is developed and compared with the available experimental data. The n=2 vortex model with reverse flow gives better results for strongly swirling flow.

Chapter 2: The Experimental Apparatus and Procedure

2-1: General

Swirling flows are classified into two types: continuous swirl flow, which maintains their characteristics over the entire axial length, and decaying swirl flow where the swirling is imparted from specific locations on the chamber and then the tangential velocity decays with the axial length. For the following experiments, the second type was used by using a vortex generator which is mounted at one end of the vortex chamber.

Compressed air is supplied to the inlets of the vortex generator. A control valve is mounted on the air supply line in order to set the desired volumetric flow rate. A rotameter is used to measure the volumetric flow rate. When the air flow passes through the vortex generator to the vortex chamber, a swirl is imparted to the field. That is, the vortex flow is generated inside the vortex chamber. Finally, the air flow passes through the central exit hole to the atmosphere.

The objective of the present experiment was to obtain the static pressure difference ($P_{in} - P_a$), and the flow rate (Q_{in}) through the vortex chamber with different Reynolds number and geometry parameters.

2-2: Vortex Chamber and Vortex Generator

The chamber used in the investigation consists of a cylindrical shape with circumferential inlets to introduce the fluid tangentially inside the chamber. The flow departs the chamber from an exit plate which is located at the end of the chamber. The chamber is made of plexiglass.

A strong swirling fluid motion is generated within the chamber via a set of inlet ports which are arranged near the bottom plate. Many researcher have studied the swirl flow using different swirl generators: axial blades placed in the pipe inlet [51]; tangential injectors [52 and 53]; tangential vane swirler generators [54 and 55]; radial blade cascade [6], etc. These studies show essential distinction in influence of different swirls on the flow field characteristics.

The present experiments have been conducted using a jet-driven vortex chamber similar to the one utilized by Vatistas et al [29]. The latest version, is shown schematically in figure (2-2-1), which offers a wider flexibility in the selection of inlet condition.

The geometrical characteristics of the vortex chamber used for the present experiments are given in table (2-2-1). The vortex chamber has a cylindrical shape with constant cross-sectional area ($r_o = 7cm$). Its length can be varied from 22, 42, 83, 128, 164, to 225 cm. The exit plate which has a hole (r_e) in the center. The exit area of the vortex chamber depends on the size of the hole, and by replacing the exit plates with hole sizes, the exit

area can be adjusted. For the experiments reported here, the diameter of the exit hole varies from 1.8 to 5.5 cm. The axis of the vortex chamber was horizontal with respect to the ground.

A modular vortex generator assembly makes the variation of the area ratio (A_{in}/A_0) and inlet flow angle φ easier. The required set of inlet conditions is obtained by the insertion of the appropriate vortex generator blocks (swirler) into the vortex generator assembly along the periphery of the vortex generator block, where a number of openings of a circular cross section are drilled at a specified angle φ. The vortex generator was made from aluminum and it has four perpendicular air inlets where the compressed air is induced. Inside the vortex generator, there is a vortex generation block (swirler). When the air flow passes through the swirler, it is guided to enter the vortex chamber in the tangential direction so that swirl is formed inside the vortex chamber. Its inlet angle can be varied at $20^o, 30^o$, 40^o, and 60^o. The swirler with inlet angle 20^o has 16 holes with diameter 0.7874 cm, at inlet angle 30^o has 16 holes with diameter 1.267 cm, at inlet angle 40^o has 8 holes with a diameter 1.905 cm, at inlet angle 60^o also has 8 holes with a diameter 1.905 cm. The geometric conditions in the vortex chamber were varied by changing the swirler angle, inlet area, chamber length, and displacing the outlet orifice.

Table 2-2-1: Geometrical Characteristics of the Vortex Chamber

φ (deg)	$D_{in}(cm)$	No. of inlet ports	$A_{in}(cm^2)$	$D_e(cm)$	$L(cm)$
20	0.7874	16	7.787	1.879, 1.976,	
30	1.267	16	20.177	2.164, 2.413,	22, 42,
40	1.905	8	22.79	2.649, 2.794,	83,128,
40	1.905	4	11.395	3.175, 3.81, 4.191, 5.588	164, 225
60	1.905	8	22.79		

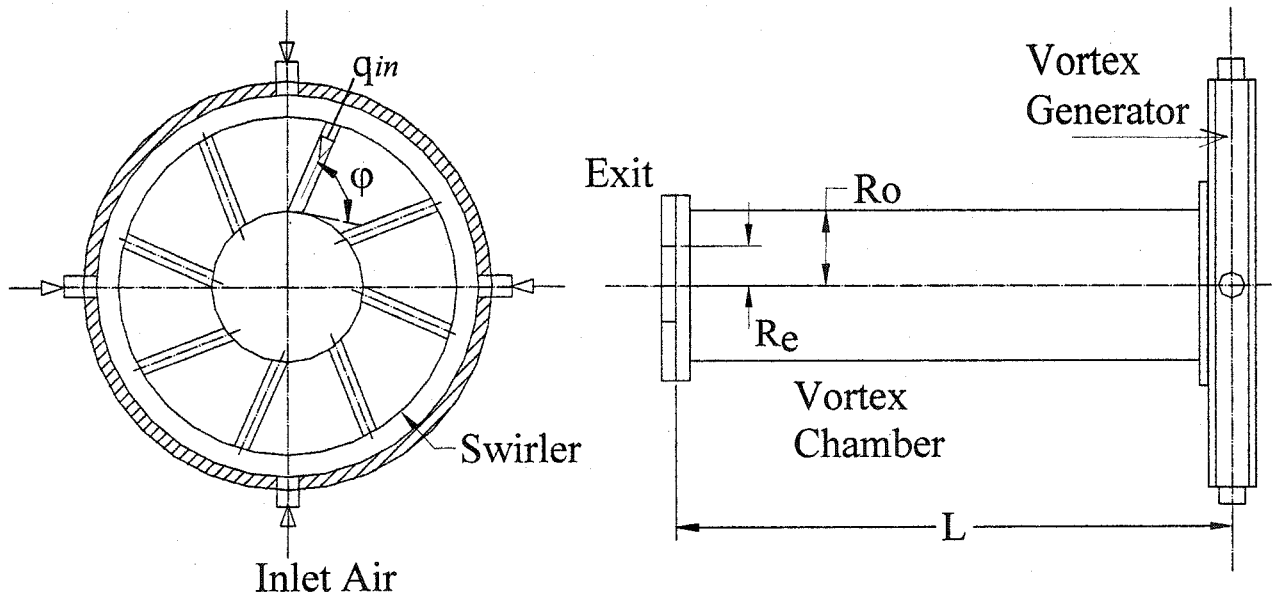

Figure (2-2-1): Schematic of the vortex chamber

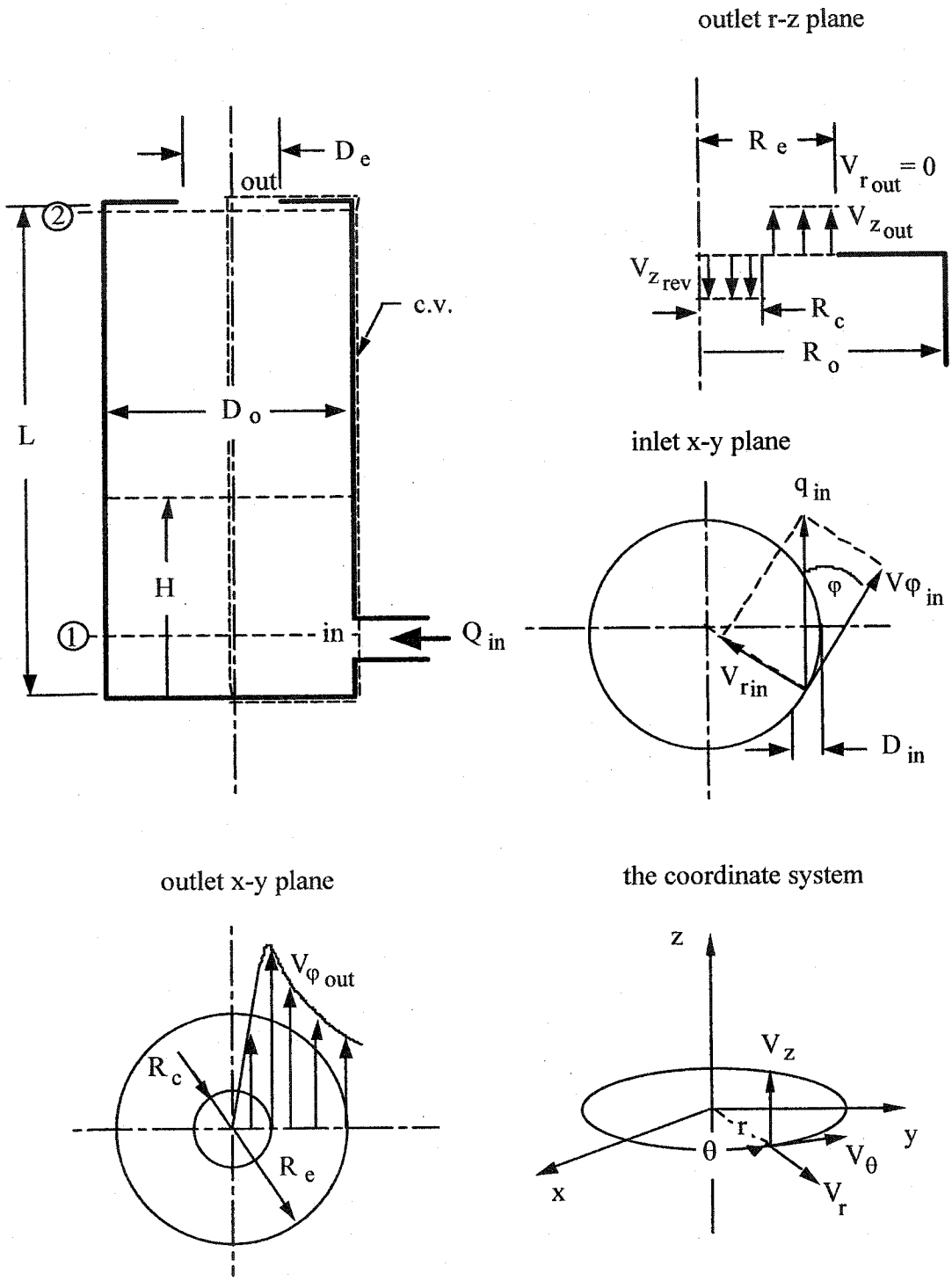

Figure (2-2-2): Schematic of the Problem

2-3: Experimental Variables and Procedures

The measurements were made at different inlet air flow rates: 0.0117 m^3/s (25 cfm), 0.014 m^3/s (30 cfm), 0.0163 m^3/s (35 cfm), and 0.0187 m^3/s (40 cfm) respectively, which are corresponding to four Reynolds numbers R_{eo} based on the average bulk velocity: 7245, 8694, 10143, and 11592 defined as:

$$R_{eo} = \frac{4Q_{in}}{\pi D_o \nu}$$

where

Q_{in} = inlet flow rate

D_o = Chamber Diameter

ν = kinematics viscosity

Chamber diameter ratio (ξ) which is defined as the ratio of the diameter of a vortex chamber (D_o) to the diameter of the exit hole (D_e), was varied from ξ = 2.51, 3.34, 3.67, 4.41, 5.01, 5.29, 5.80, 6.47, 7.08 to 7.45.

Chamber aspect ratio (ζ) which is defined as the ratio of the chamber length L to the diameter of a vortex chamber (D_o) was varied from ζ = 1.57, 3.00, 5.93, 9.14, 11.71 to 16.07.

Area ratio (α) which is defined as the ratio of the total inlet area (A_{in}) to the cross sectional area of the vortex chamber A_o was varied from $\alpha = 0.074, 0.05, 0.131$ to 0.148.

For the pressure drop experiments, the static pressure in each tangential inlet port was averaged by connecting in parallel all the pressure pick-up tubes into a common tube. The measurements of the mean gage pressure, $P_{in} - P_a$, were obtained using a U-tube filled with Meriam oil, having a specific gravity equal to 1.00. The estimated uncertainty for the pressure drop measurements is between 8-10 %. A rotameter was used to measure the volumetric flow rate of the inlet air. This was calibrated at standard conditions (1 atmosphere and 0^o C). For the flowrates used, the uncertainty was estimated to be from 1.4 % to 2.0 %.

Air at standard temperature was the working fluid. A typical experimental run involved the following simple routine: at specific length and an inlet angle i.e $\varphi = 20^o$, the flow rate was set at Q_{in}=0.011 m^3/s (25 cfm), the static pressure was recorded at different sizes of the chamber exit D_e, then at the same inlet angle and length repeat the measuerments at different flow rates (i.e Q_{in}=30, 35, and 40 cfm). Repeat the procedures again for another length and an inlet angle (i.e $\varphi = 30^o, 40^o$, and 60^o).

Chapter 3: Analytical Development of the Problem

3-1: Dimensional Analysis

In order to reduce the experimental effort and at the same time to present results in a general form, dimensional analysis was performed.

Consider the steady, incompressible, swirling flow within the vortex chamber of Fig. 2-2-2. Experiments have shown the pressure drop across the vortex chamber ($\Delta P = P_{in} - P_a$) to depend on the vortex strengths at the inlet (κ_{in}) and outlet (κ_{out}), the flow rate (Q), the inlet area (A_{in}), the length of the chamber (L), its radius (R_o), the radius of the outlet (R_e), the vortex core radius (R_c), the fluid density, (ρ), and its viscosity (μ), or

$$P_{in} - P_a = fn\{\kappa_{in}, \kappa_{out}, L, R_o, R_e, R_c, A_{in}, Q, \rho, \mu\}$$

Therefore, there are 11 variables and three basic dimensions involved with the problem. The same phenomenon must be equivalently described by the 8 dimensionless parameters,

$$C_p = fn\{\chi, \xi, \varphi, \zeta, \alpha, \delta, R_{eo}\}$$

where

$$C_p = \frac{2(P_{in} - P_a)}{\rho q_{in}^2},\quad \chi = \frac{R_c}{R_e},\quad \xi = \frac{R_o}{R_e},\quad \varphi = \cos^{-1}\left(\frac{V_{\theta in}}{q_{in}}\right),\quad \zeta = \frac{L}{D_o},\quad \alpha = \frac{A_{in}}{A_o},\quad \delta = \frac{\kappa_{out}}{\kappa_{in}},$$

$$R_{eo} = \frac{4Q}{\nu \pi D_o}$$

The above analysis provides the expected functional relations among the main dimensionless parameters involved with the problem.

All the experimental observations were treated using the above functional relationship that was suggested by dimensional analysis considerations. The results are shown in figure (3-1-1) for swirles with two inlet angles; $\varphi = 30^o$ and 40^o. It is indeed evident that given the aspect ratio, the corresponding test data collapse into a single curve. As it is expected, the dimensionless pressure drop depends strongly on the chamber's aspect ratio. The latter confirms the original hypothesis. In addition it makes available through a chart the generalized relationship among the most important geometrical and fluid properties.

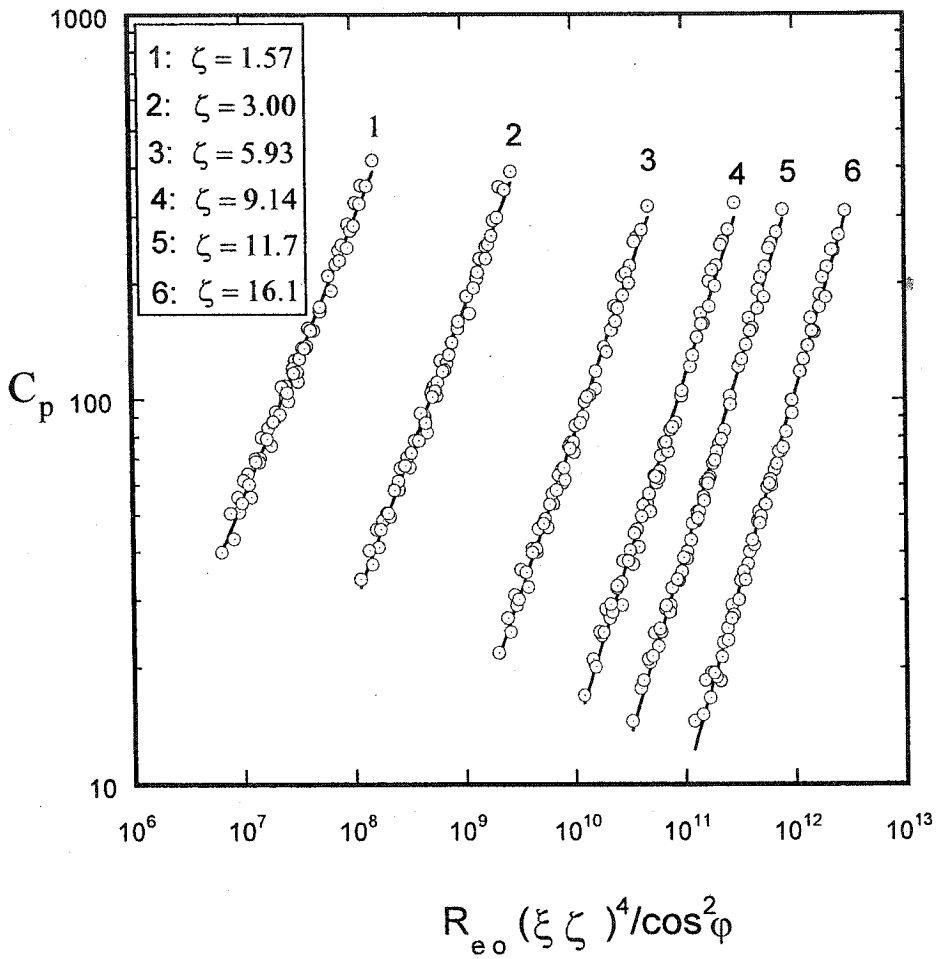

Figure (3-1-1): Pressure Coefficient vs the Dimensional Groups

3-2: Pressure Drop and Core Size Based on n=2 Vortex Model

A thorough theoretical study of swirling flow requires a differential characterization of the internal flow through the solution of the Navier Stokes and continuity equations, which is difficult. Often however, an acceptable description can be achieved by concentrating on the overall features (integral approach) and thus bypassing the particular details of the interior flow. The present research will use the second method.

The energy equation will be solved for strongly swirling, steady, constant viscosity, axi-symmetric, and incompressible flow. To simplify the problem several assumptions are used. These are: the pressure and the total velocity at the inlet are both uniform; the radial velocity at the exit is neglected since it does not have the space and time to develop; and at the exit the pressure is ambient.

Energy balance over the control volume enclosing the chamber yields

$$\oint_{c.s.}\left\{\frac{P}{\rho}+\frac{1}{2}\vec{q}^{\,2}\right\}\vec{q}\circ\vec{n}\,dA+E_{\varphi}=0 \qquad (3\text{-}1)$$

or

$$\left[\frac{P_{in}}{\rho}+\frac{1}{2}q_{in}^2\right]Q_{in} = \int_{R_c}^{R_e}\left[\frac{P_a}{\rho}+\frac{1}{2}\left\{V_{\varphi out}^2+V_{z out}^2\right\}\right]V_{z out}\ 2\pi r\,dr$$
$$-\int_{0}^{R_c}\left[\frac{P_a}{\rho}+\frac{1}{2}\left\{V_{\varphi out}^2+V_{z rev}^2\right\}\right]V_{z rev}\ 2\pi r\,dr + E_\varphi \qquad (3\text{-}2)$$

Vatistas et al. [56] reported on vortex model that produced a family of bounded velocity distribution which depends on the value of an exponent n. For the case of n=2 this particular velocity profile was found to provide good agreement with measured velocities, see references [57, 58, 59]. The model is given by

$$V_\varphi = V_c\ \frac{\hat{r}}{\left[1+\hat{r}^{2n}\right]^{1/n}} \text{ where } \hat{r}=\frac{r}{R_c} \text{ and } V_c=\frac{\Gamma}{2\pi R_c}$$

For the case n = 2, the tangential velocity at plane 1 (see fig.2-2-2) is given by:

$$V_{\varphi 1} = V_{c\,in}\,R_c\,\frac{r}{\left[R_c^4+r^4\right]^{1/2}} \qquad (3\text{-}3)$$

where

$$V_{cin}=\frac{\Gamma}{2\pi R_c}\ ,\ \Gamma=V_{\varphi in}\,2\pi R_o\text{, and } V_{\varphi in}=q_{in}\cos(\varphi)$$

The essence of the present analysis lies in the application of the energy equation, where the bulk of the loss is assumed to occur across the vortex chamber. For engineering purposes it is important to understand the decay process of swirl intensity across a vortex chamber. The vortex decay factor δ is expected to vary with the Reynolds number, aspect ratio, swirl angle, and area ratio. It is evident from the experimental results of Yan et al [60] that the vortex decay factor value is between zero and one. When δ is set to one, this means that the swirl velocity at the outlet of the chamber is equal to the swirl velocity at the inlet of the chamber. Mathematically, it can be given by

$$\delta = \frac{V_{c\ out}}{V_{c\ in}}$$

The outlet swirl velocity at the vortex chamber exit is given by

$$V_{\varphi out} = V_{c\ out} R_c \frac{r}{\left[R_c^4 + r^4\right]^{1/2}} \tag{3-4}$$

And note that

$$V_{\varphi 2} \approx V_{\varphi out}$$

For strong swirling flow the pressure drops to values less than the atmospheric pressure inside the core region, which leads to the suction of flow back towards the vortex

chamber, see Osami [44]. Uniform axial reverse flow inside the core and uniform axial outlet flow outside the core are assumed at the exit port of the chamber, see figure (2-2-2), and are given by

$$V_{z\,rev} = \frac{Q_{rev}}{\pi R_c^2}$$

and

$$V_{z\,out} = \frac{Q_{out}}{\pi (R_e^2 - R_c^2)}$$

E_φ being the loss due to vortex decay will be made here to include it through the reduction of the swirl kinetic energy between planes 1 and 2, see figure (2-2-2).

$$E_\varphi = \frac{\Delta K.E_{\theta:1\to 2}}{\rho} = \frac{1}{2}\int_{R_c}^{R_o}\left[V_{\varphi 1}^2 - V_{\varphi 2}^2\right] V_{zo}\; 2\pi r\, dr$$

where the axial velocity inside the chamber is given by:

$$V_{zo} = \frac{Q_{in}}{\pi (R_o^2 - R_c^2)}$$

From the mass conservation

$$Q_{in} + Q_{rev} = Q_{out}$$

or

$$1 + \gamma_1 = \gamma_2$$

where

$$\gamma_1 = \frac{Q_{rev}}{Q_{in}},\ \gamma_2 = \frac{Q_{out}}{Q_{in}},\ Q_{in} = q_{in}\ A_{in}$$

Performing the integration of equation (3-2), then the following equation for the pressure drop coefficient (C_p) is obtained:

$$C_p = \gamma_2 \delta^2 \cos^2(\varphi)\, \xi^2 \frac{Ln\left[\frac{1}{2}\left\{1+\frac{1}{\chi^4}\right\}\right]}{2(1-\chi^2)} + \gamma_2^3 \alpha^2 \xi^4 \frac{1}{(1-\chi^2)^2}$$

$$- \left[\gamma_2 - 1\right]\delta^2 \cos^2(\varphi)\, \xi^2 \frac{Ln(2)}{2\chi^2} - \left[\gamma_2 - 1\right]^3 \alpha^2 \xi^4 \frac{1}{\chi^4} \qquad (3\text{-}5)$$

$$+ \gamma_2 \cos^2(\varphi)\left[1-\delta^2\right] \frac{Ln\left[\frac{1}{2}\left\{1+\left(\frac{\xi}{\chi}\right)^4\right\}\right]}{2\left[1-\left(\frac{\chi}{\xi}\right)^2\right]} - 1$$

where

$$C_p = \frac{2\Delta P}{\rho q_{in}^2},\ \Delta P = P_{in} - P_a,\ \chi = \frac{R_c}{R_e},\ \xi = \frac{R_o}{R_e},\ \varphi = \cos^{-1}\left(\frac{V_{\varphi in}}{q_{in}}\right),\ \zeta = \frac{L}{D_o},\ \alpha = \frac{A_{in}}{A_o}$$

The Reynolds number (R_{eo}) based on the average bulk velocity is defined as:

$$R_{eo} = \frac{4Q_{in}}{\nu \pi D_o}$$

At a given design geometry parameters (ξ, φ, α, ζ) and the vortex decay factor (δ), then

$$C_p = f_n(\chi, \gamma_2)$$

Equation (3-5) reveals that C_p is unbounded when χ tends to zero or one, therefore, there must exist $0 < \chi < 1$ such that C_p is minimum. The later requires that:

$$\frac{\partial C_p}{\partial \gamma_2} = 0$$

or

$$\gamma_2^2\left[3\alpha^2\xi^4\left\{\frac{1}{\left[1-\chi^2\right]^2}-\frac{1}{\chi^4}\right\}\right]+\gamma_2\left[6\frac{\alpha^2\xi^4}{\chi^4}\right]+\delta^2\cos^2(\varphi)\xi^2\frac{Ln\left[\frac{1}{2}\left\{1+\frac{1}{\chi^4}\right\}\right]}{2(1-\chi^2)}$$

$$-\delta^2\cos^2(\varphi)\xi^2\frac{Ln[2]}{2\chi^2}-3\frac{\alpha^2\xi^4}{\chi^4} \qquad (3\text{-}6)$$

$$+\cos^2(\varphi)\left[1-\delta^2\right]\frac{Ln\left[\frac{1}{2}\left\{1+\left(\frac{\xi}{\chi}\right)^4\right\}\right]}{2\left[1-\left(\frac{\chi}{\xi}\right)^2\right]}=0$$

From equation (3-6) one root of two has physical meaning, then

$$\gamma_2 = g(\chi)$$

If γ_2 is substituted into equation 3-5, then

$$C_p = h(\chi)$$

The minimum C_p principle yields,

$$\frac{\partial C_p}{\partial \chi}=0 \qquad (3\text{-}7)$$

Given the values of ξ, φ, α, and δ, equation (3-7) can be solved numerically for χ using any traditional root finding method. In order to know the value of δ one must know how the vortex decays. Since this knowledge is not available its value will be found based on the experimental results using a modified version of least squares technique.

The observations will provide the data of C_p across a vortex chamber operating under specific conditions. The above theory will then be applied to curve-fit the results assuming different values of δ and calculating the square error according to the formula:

$$E = \sum_{i=1}^{N} \left[C_{p\ \exp\ i} - C_{p\ theor\ i} \right]^2 \qquad (3\text{-}8)$$

Equation (3-8) will generate a graph as the one shown in figure (3-2-1). The optimum δ for a given set of data will then be the one that produces the least square error (E).

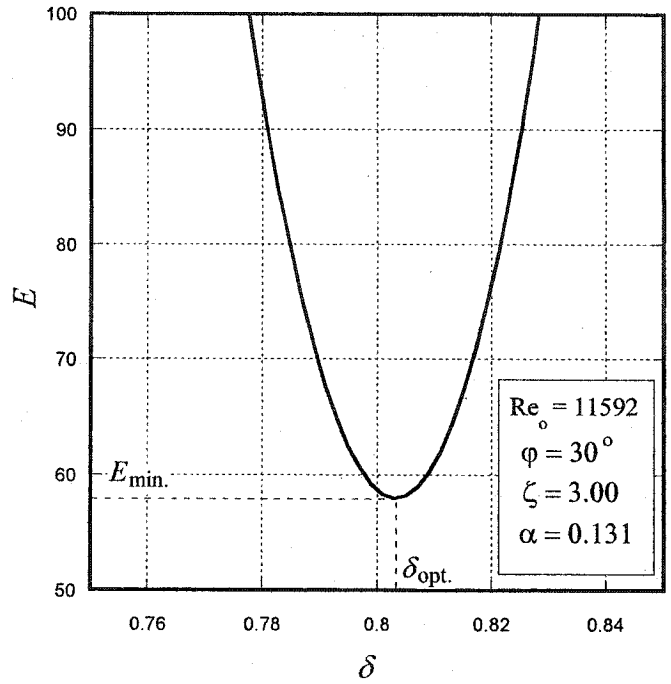

Figure (3-2-1): The least square error criteria for n=2 vortex model.

3-3: Pressure Drop and Core Size Based on Free Vortex Model

The flow field is assumed to be axi-symmetric, the radial velocity component at the exit is considered to be negligibly small in comparison to the other two while the total inlet velocity and static pressure are both uniform, and the exit pressure is equal to the ambient, then equation (3-1) simplifies into:

$$\left[\frac{P_{in}}{\rho}+\frac{1}{2}q_{in}^2\right]Q = P_a\int_{R_c}^{R_e} V_{z\,out}\,2\pi r\,dr + \int_{R_c}^{R_e}\frac{1}{2}\left[V_{\varphi out}^2+V_{z out}^2\right]V_{z\,out}\,2\pi r\,dr + E_\varphi \qquad (3\text{-}9)$$

In order to evaluate the integrals in equation (3-9), the variations of both tangential and axial velocity components as a function of the radius must be provided. Based on the work of Vatistas et al [26] the axial velocity at the exit is regarded to be uniform

$$V_{z\,out} = \frac{Q}{\pi[R_e^2 - R_c^2]}$$

whereas the tangential velocity is as in a *free vortex* given by

$$V_{\varphi\,out} = \frac{\delta \kappa_{in}}{r} \tag{3-10}$$

The anticipated diminishing strength of the tangential velocity evident from the LDA results of Yan et al [60] is denoted by the factor δ that takes on values between zero and one, the vortex decay factor is defined as

$$\delta = \frac{\kappa_{out}}{\kappa_{in}} = \frac{V_{c\,out}}{V_{c\,in}}$$

where

$$Q = q_{in} A_{in},\ \kappa_{in} = V_{\varphi in} R_o, \text{ and } V_{\varphi in} = q_{in} \cos(\varphi)$$

Energy losses E_φ can be taken into account if the detailed flow field inside the chamber is known. Since the latter is presently not available an attempt will be made here to include it through the reduction of the swirl kinetic energy between planes 1 and 2, see figure (2-2-2),

$$E_\varphi = \frac{\Delta k.e_{\theta\,1\to2}}{\rho} = \frac{1}{2}\int_{R_c}^{R_o}\left[V_{\varphi1}^2 - V_{\varphi2}^2\right]V_{z\,o}\,2\pi r\,dr$$

where

$$V_{\varphi1}^2 - V_{\varphi2}^2 = (1-\delta^2)\;V_{\varphi1}^2 = (1-\delta^2)\left[\frac{\kappa_{in}}{r}\right]^2$$

and the axial velocity inside the chamber is given by:

$$V_{z\,o} = \frac{Q}{\pi(R_o^2 - R_c^2)}$$

In view of the above-mentioned simplifications, equation 3-9 reduces to:

$$C_p = \frac{\alpha^2\xi^4}{(1-\chi^2)^2} - 2\frac{\delta^2\xi^2\cos^2(\varphi)\ln(\chi)}{(1-\chi^2)} - 2\,\frac{(1-\delta^2)\cos^2(\varphi)\ln\left(\frac{\chi}{\xi}\right)}{1-\left[\frac{\chi}{\xi}\right]^2} - 1 \qquad (3\text{-}11)$$

The minimum C_p principle yields,

$$\left\{2a_1\chi^2 - a_2\left(1-\chi^2\right)\left(\chi^2\left[2\ln(x)-1\right]+1\right)\right\}\left(1-\left[\frac{\chi}{\xi}\right]^2\right)$$
$$+a_3\left(1-\chi^2\right)^3\left\{1-\left[\frac{\chi}{\xi}\right]^2\left[2\ln\left(\frac{\chi}{\xi}\right)-1\right]\right\}=0 \qquad (3\text{-}12)$$

where

$$a_1=\alpha^2\xi^4,\ a_2=\delta^2\xi^2\cos^2(\varphi),\ \text{and}\ a_3=\left(1-\delta^2\right)\cos^2(\varphi)$$

Given the values of α, φ, ξ, and δ the above equation can be solved numerically for χ using any of the traditional root finding methods. The optimum δ for a given set of data will be obtained from equation (3-11) that produces the least square error (E), see figure (3-3-1).

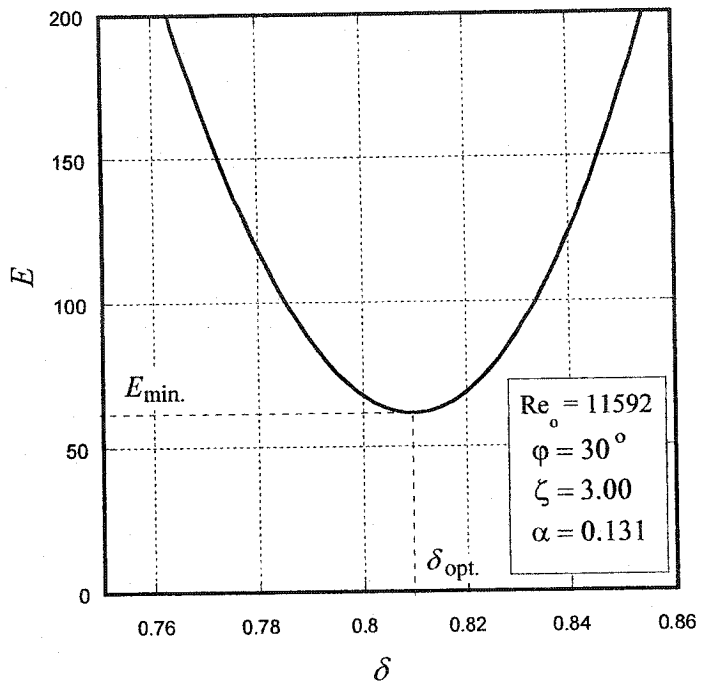

Figure (3-3-1): The least square criteria for free vortex model.

3-4: Minimum Flowrate and Maximum Pressure Drop Criteria

In view of the above-mentioned simplifications, equation (3-5) or (3-11) reduces to:

$$\Delta P = P_{in} - P_a = \frac{\rho C_p}{2 A_{in}^2} Q^2 \qquad (3\text{-}13)$$

Given the geometry of the chamber and δ are fixed, and taking the derivative of equation (3-13) with respect to χ, results in

$$\frac{d\Delta P}{d\chi} = \frac{\rho}{A_{in}^2}\left\{C_p Q\frac{dQ}{d\chi} + \frac{Q^2}{2}\frac{dC_p}{d\chi}\right\} \tag{3-14}$$

For a given flow rate Q the above equation yields:

$$\frac{d\Delta P}{d\chi} = \frac{\rho}{A_{in}^2}\frac{Q^2}{2}\frac{dC_p}{d\chi}$$

If now one fixes ΔP, equation (3-14) gives:

$$\frac{dQ}{d\chi} = -\frac{Q}{2C_p}\frac{dC_p}{d\chi}$$

At the extreme, for χ = 0 and 1 ΔP will be unbounded while Q will be zero. Between these values of χ, there is a critical value χ_c where ΔP and Q attain exrema, an absolute minimum for the former and an absolute maximum for the latter, see figure (3-4-1). Therefore, the last principle can be used, as the supplementary condition required for the determination of the vortex core size. Binie and Hookins [27] first introduced the previous postulate in their investigations with regard to the discharge of swirling flow through trumpet-shaped circular weirs. A similar approach was also taken by Lewellen [25] and Vatistas et al [26] in their analysis of vortex flows confined in tubes.

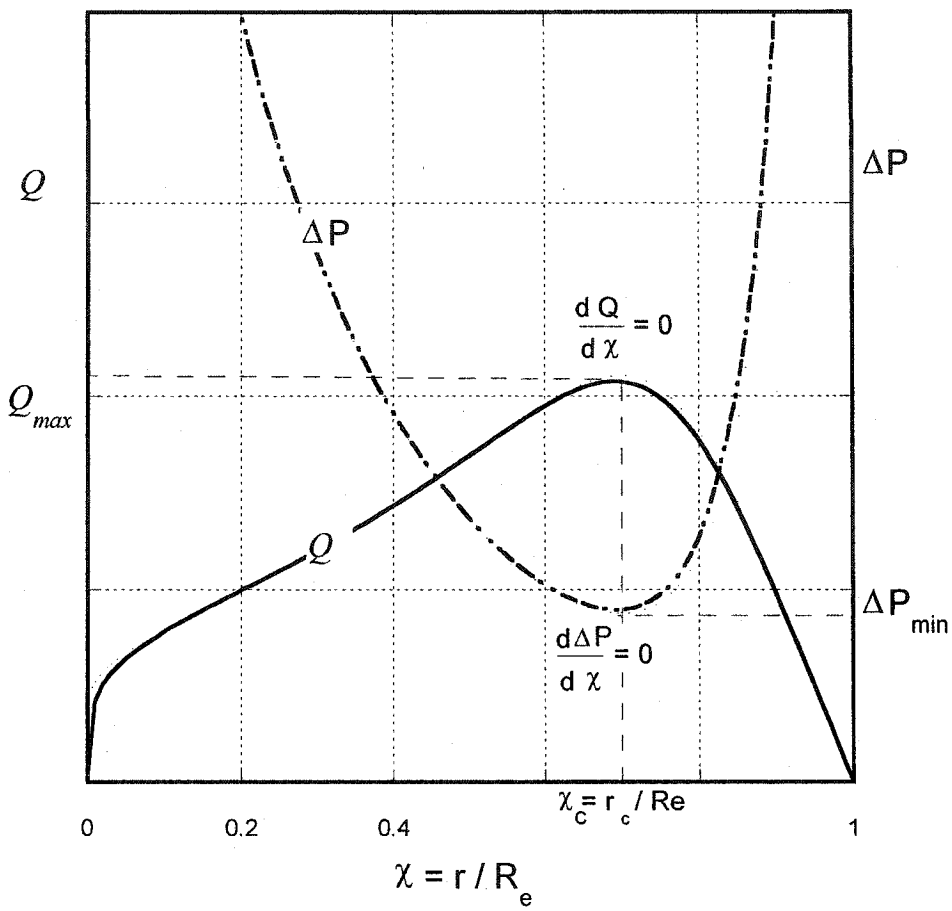

Figure (3-4-1): The extremum condition

Chapter 4: Discussion of the Results

4-1: The n=2 Vortex Model for Reverse Flow

Figures (4-1-1) to (4-1-4) compare the experimental data with the present theory of the pressure drop coefficient (C_p) for aspect ratio $\zeta=3.0$ and inlet angles $\varphi=20^\circ, 30^\circ, 40^\circ, 60^\circ$ respectively. It is clear that as the diameter ratio (ξ) and the Reynolds number (R_{eo}) increase, the pressure coefficient (C_p) increases. Stronger vortices will be produced by increasing the diameter ratio and/or Reynolds number, resulting in a higher tangential velocity and hence a higher pressure drop. A good correlation between the experiment and the present theory is less than 10 %. Figures (4-1-1) and (4-1-2) show a good agreement when $\xi>3.67$, and in the case of figures (4-1-3) and (4-1-4) when $\xi>4.4$. This is expected because the present model is based on intense swirl conditions, where at low contraction ratios and large inlet angle the swirl intensity is reduced. Figure (4-1-5) shows the percentage difference error at $R_{eo}=10143$. For low contraction ratio (i.e $\xi=2.5$) the error reach 40%, while at contraction ratio between (4-5) the percentage error is less than 10%, and when the contraction ratio >5 the percentage error is less than 5%. It is because the condition of the strong vortex does not exist under the small diameter ratios.

Any of the previous figures (4-1-1) to (4-1-4) point out that δ increases with R_{eo} tending towards one for larger R_{eo} values. The last makes the pressure profiles to approach the formulation of Vatistas et al [26] which assumes a $\delta = 1.00$. This propensity is amply evident for configuration ($\varphi = 40^o$, $\alpha = 0.148$, $\zeta = 3.00$), see figure (4-1-3), where the pressure coefficient is seen to come within the reach of Vatistas et al [26]. The preceding does not however imply that friction is less for higher R_{eo} numbers but rather that under these conditions the inertia being considerably larger overshadows the viscous effects. After all, this is precisely the definition of the Reynolds number. Hence the theoretical development of Ref. 25 and Ref. 26 must be limited to the high Reynolds number region where the inertia dominates and as such ignoring friction (one of their main assumptions) will not produce large discrepancies. This by no means suggests that the present development is free of limitations. Since the frictional losses due to the secondary flow, taking place in the r-z plane have not been considered, discrepancies in the flow regime where these are no longer insignificant are anticipated.

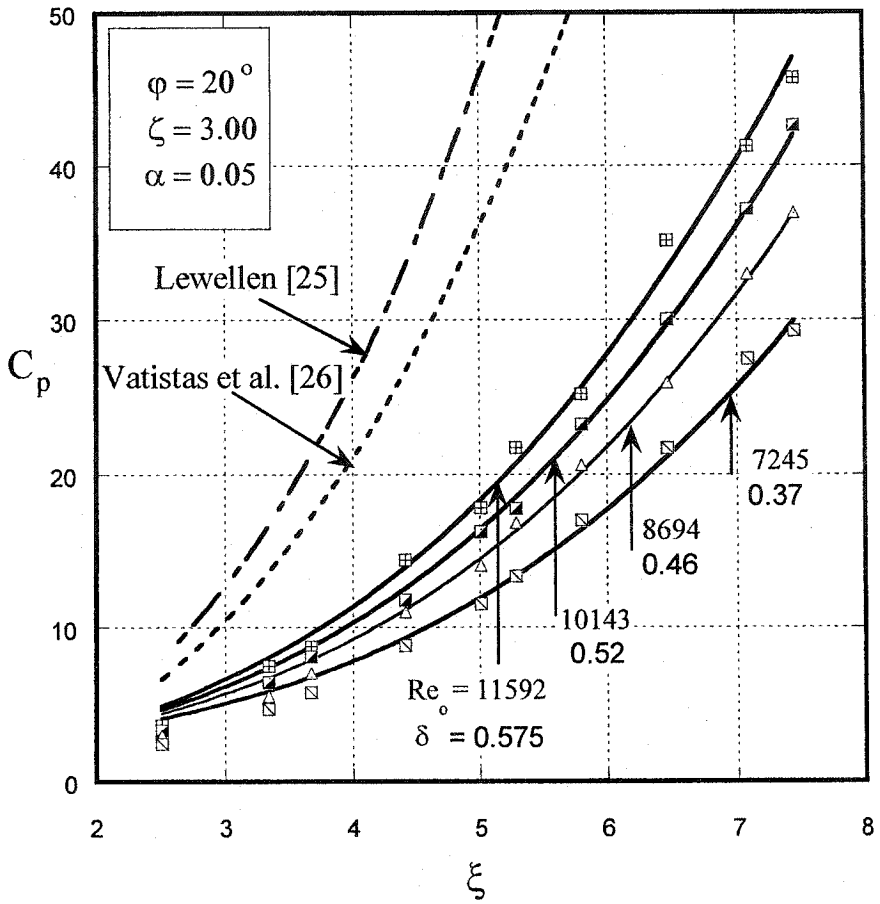

Figure (4-1-1): Pressure drop coefficient based on n=2 reverse vortex model in an intermediate aspect ratio chamber for a small inlet angle ($\varphi = 20°$) for different Reynolds numbers. The symbols refer to present experiment while the solid lines refer to present theory.

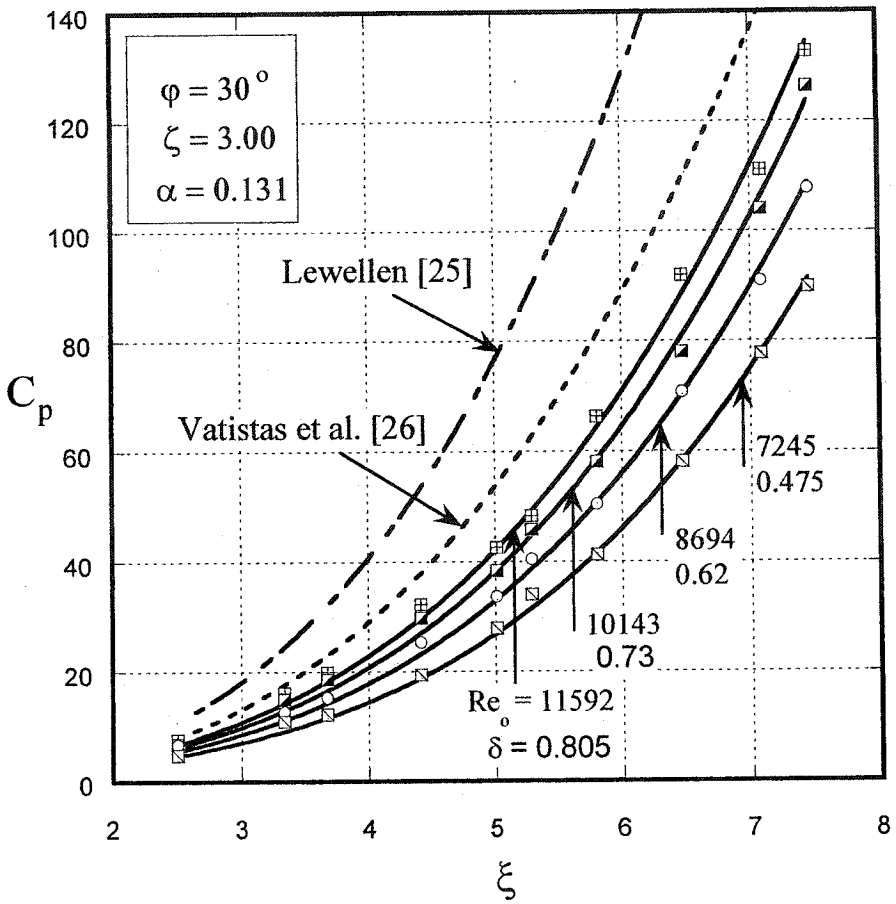

Figure (4-1-2): Pressure drop coefficient based on n=2 reverse vortex model in an intermediate aspect ratio chamber and inlet angle ($\varphi = 30°$) for different Reynolds numbers. The symbols refer to present experiment while the solid lines refer to present theory.

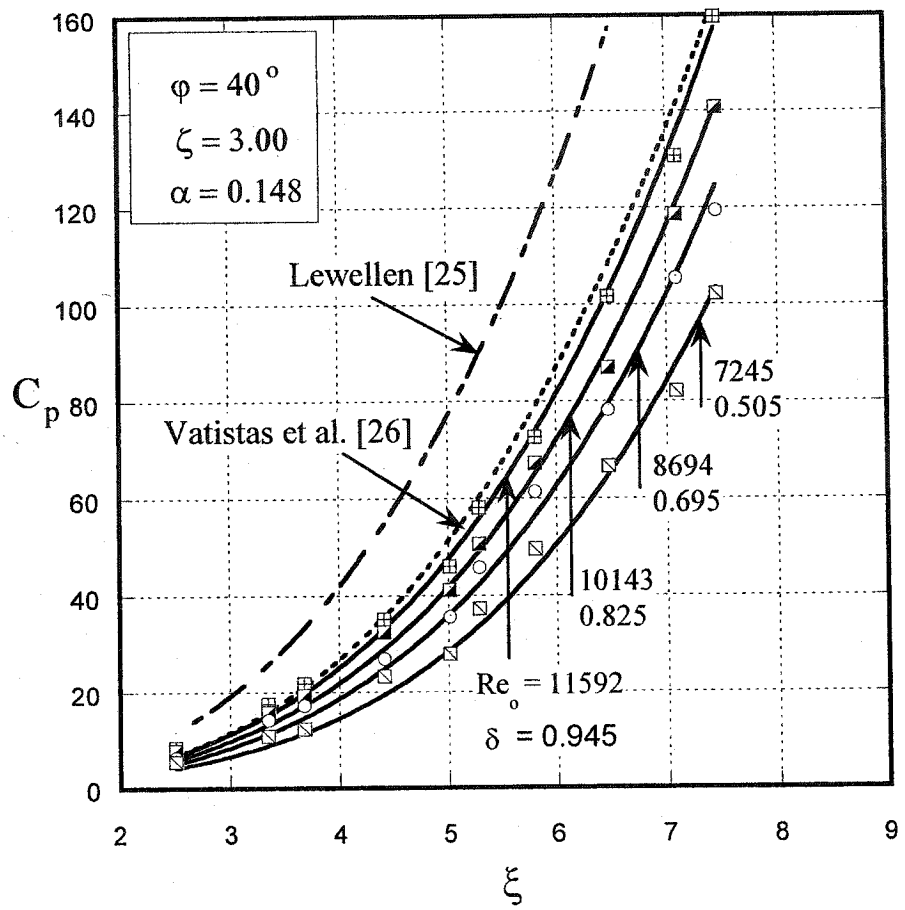

Figure (4-1-3): Pressure drop coefficient based on n=2 reverse vortex model in an intermediate aspect ratio chamber and inlet angle ($\varphi = 40°$) for different Reynolds numbers. The symbols refer to present experiment while the solid lines refer to present theory.

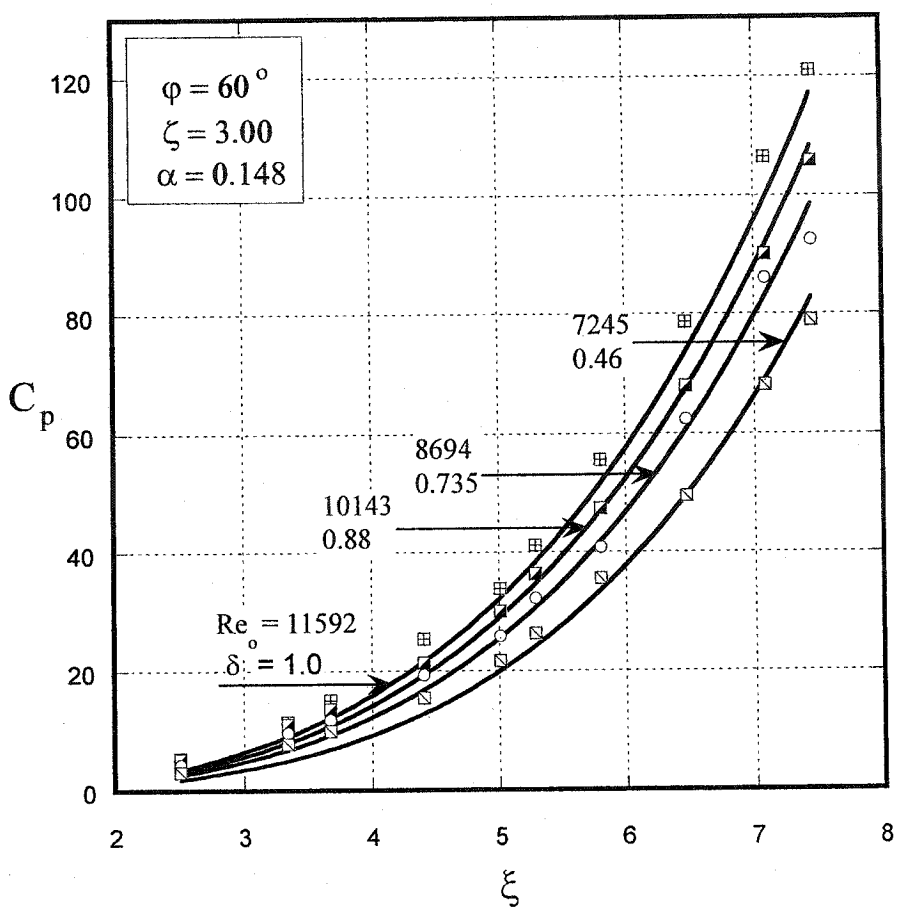

Figure (4-1-4): Pressure drop coefficient based on n=2 reverse vortex model in an intermediate aspect ratio chamber for large inlet angle (φ=60°) for different Reynolds numbers. The symbols refer to present experiment while the solid lines refer to present theory.

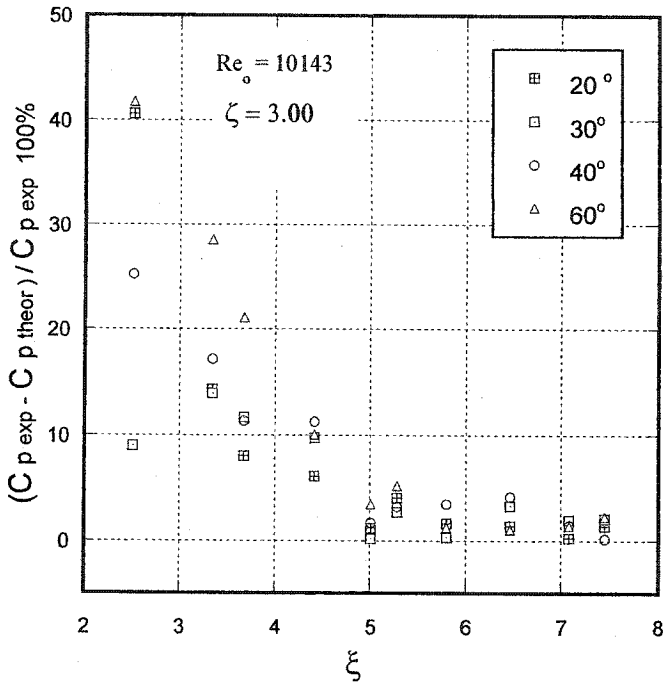

Figure (4-1-5): Percentage error criteria.

It is of interest to investigate the contributions of the axial inertial term (A_{axial}), swirl term (S_{swirl}), and the friction term ($F_{friction}$) on the pressure drop. From equation (3-5) they can be written respectively as:

$$A_{axial} = \gamma_2^3 \alpha^2 \xi^4 \frac{1}{(1-\chi^2)^2} - \left[\gamma_2 - 1\right]^3 \alpha^2 \xi^4 \frac{1}{\chi^4}$$

$$S_{swirl} = \gamma_2 \delta^2 \cos^2(\varphi) \xi^2 \frac{Ln\left[\frac{1}{2}\left\{1+\frac{1}{\chi^4}\right\}\right]}{2(1-\chi^2)} - \left[\gamma_2 - 1\right] \delta^2 \cos^2(\varphi) \xi^2 \frac{Ln(2)}{2\chi^2}$$

$$F_{friction} = \gamma_2 \cos^2(\varphi)\,(1-\delta^2)\,\frac{Ln\left[\frac{1}{2}\left\{1+\left(\frac{\xi}{\chi}\right)^4\right\}\right]}{2\left[1-\left(\frac{\chi}{\xi}\right)^4\right]}$$

To characterize the degree of flow swirling in a vortex chamber a swirl number S is introduced. Various ways of determining this parameter exist. The simplest expressions represent the ratios of maximum tangential velocity to a maximum axial one, or the averaged tangential velocity to an averaged axial one. The most widespread is based on the Gupta et al [1] definition:

$$S = \frac{2\,G_{\theta o}}{G_{z o}\,D_h}$$

where $G_{\theta o}$ is the axial flux of swirl momentum,

$$G_{\theta o} = \int_{R_c}^{R_o} \rho V_{z o} V_{\varphi 2}\, r^2\, dr$$

$G_{z o}$ is the axial flux of axial momentum,

$$G_{zo} = \int_{R_c}^{R_o} \rho V_{zo}^2 \, r \, dr$$

and D_h is the hydraulic diameter of the vortex chamber,

$$D_h = 2 R_o \left[1 - \frac{\chi}{\xi}\right]$$

Therefore the swirl number (S) is given by:

$$S = \frac{\delta \cos(\varphi) \left\{ \left[\left(\frac{\chi}{\xi} \right)^4 + 1 \right]^{1/2} - \sqrt{2} \left(\frac{\chi}{\xi} \right)^2 \right\}}{\gamma_2 \, \alpha \left[1 - \frac{\chi}{\xi}\right]}$$

The curves in figure (4-1-6) show the axial, swirl, and dissipation contributions to the flow field. It is clear that as ξ increases, the swirl number (S) increases, the core size (χ) decreases, and then the effective outlet area σ

$$\sigma = \frac{A_e}{A_o} = \frac{1 - \chi^2}{\xi^2}$$

contract, which physically represents an annular ring where the flow passes through it. Then the axial inertial term (A_{axial}) increases and the swirl term (S_{swirl}) and the friction term ($F_{friction}$) also increase.

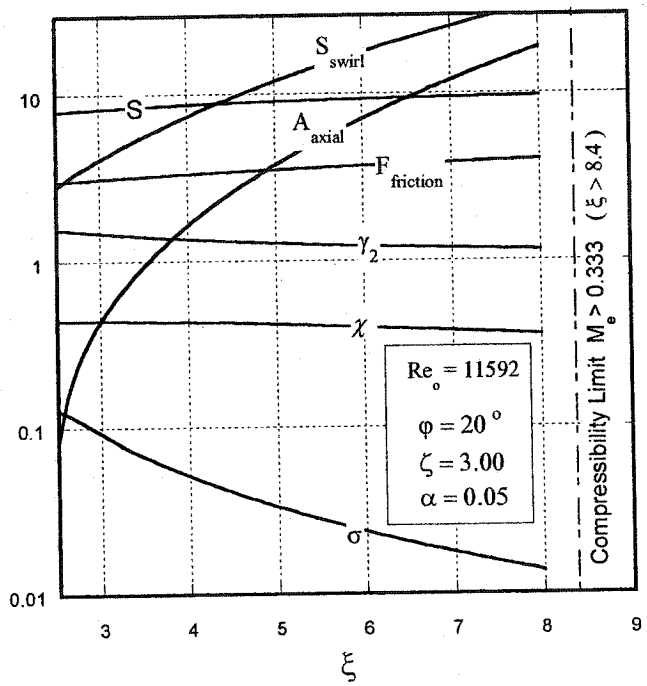

Figure (4-1-6): Variation of various flow terms.

The pressure drop coefficients for different configurations for n=2 reverse vortex model are given in figures (4-1-7) to (4-1-15). All figures show that as the aspect ratio (ζ) increases, the pressure drop coefficient decreases and the friction increases (δ decreases).

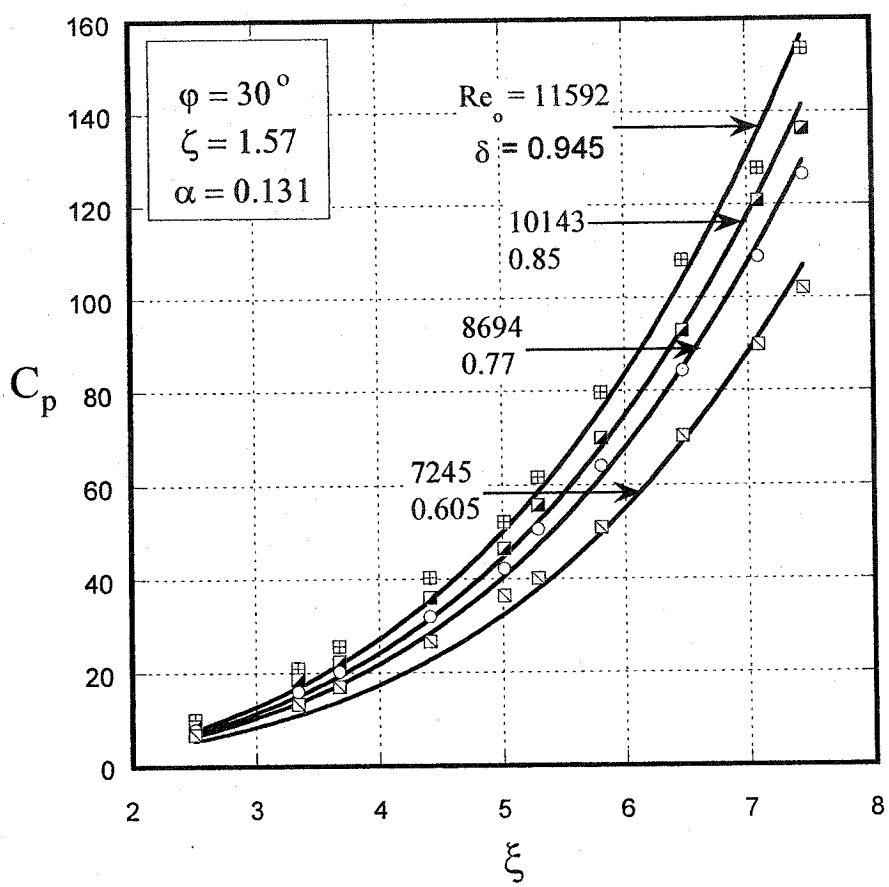

Figure (4-1-7): Pressure drop coefficient based on n=2 reverse vortex model in short aspect ratio chamber for an intermediate inlet angle (φ=30°) for different Reynolds numbers. The symbols refer to present experiment while the solid lines refer to present theory.

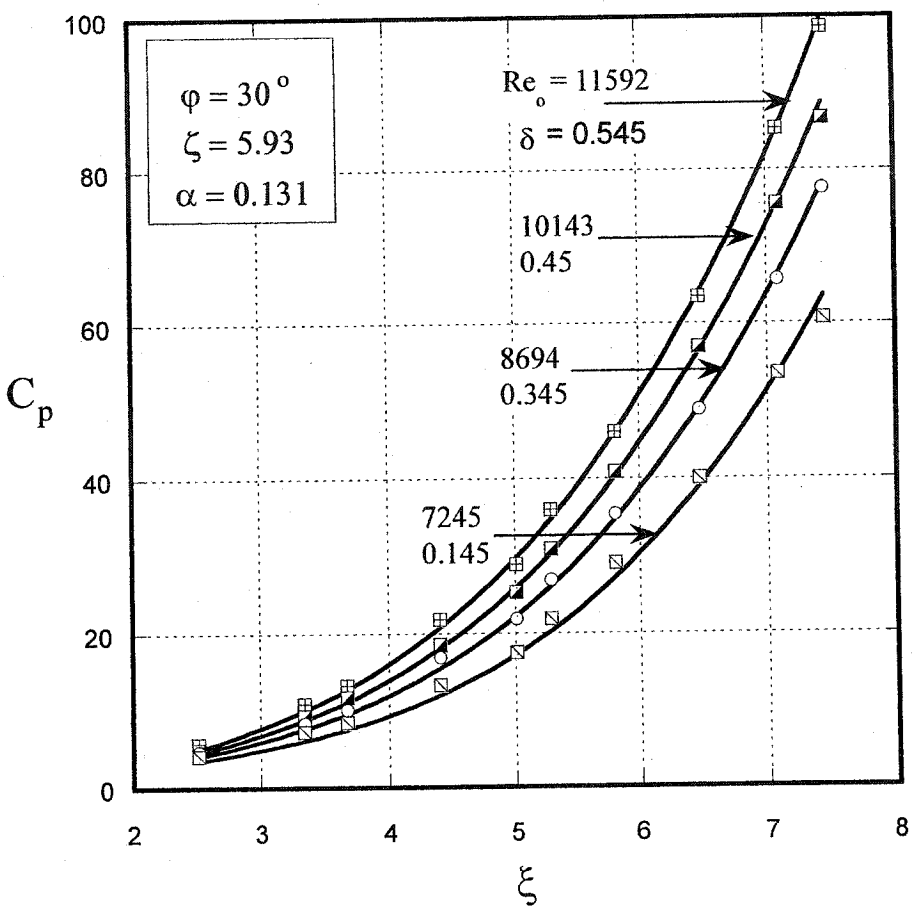

Figure (4-1-8): Pressure drop coefficient based on n=2 reverse vortex model in an intermediate aspect ratio and inlet angle (φ=30°) chamber for different Reynolds numbers. The symbols refer to present experiment while the solid lines refer to present theory.

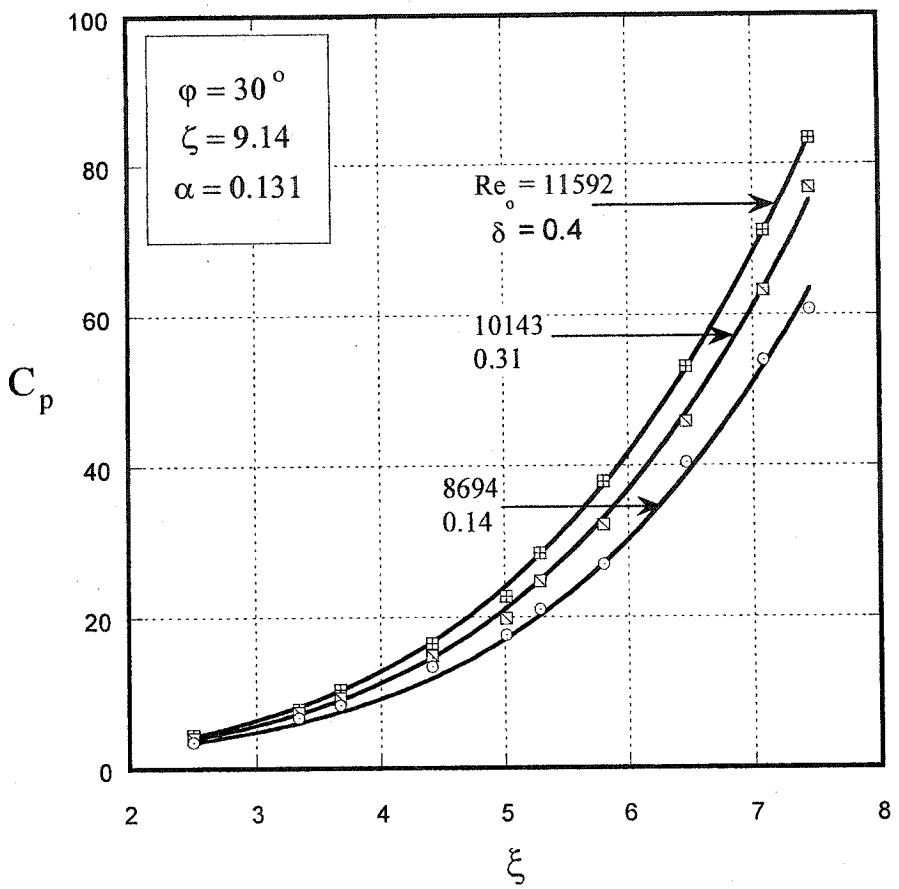

Figure (4-1-9): Pressure drop coefficient based on n=2 reverse vortex model for long aspect ratio and an intermediate inlet angle ($\varphi = 30^\circ$) chamber for different Reynolds numbers. The symbols refer to present experiment while the solid lines refer to present theory.

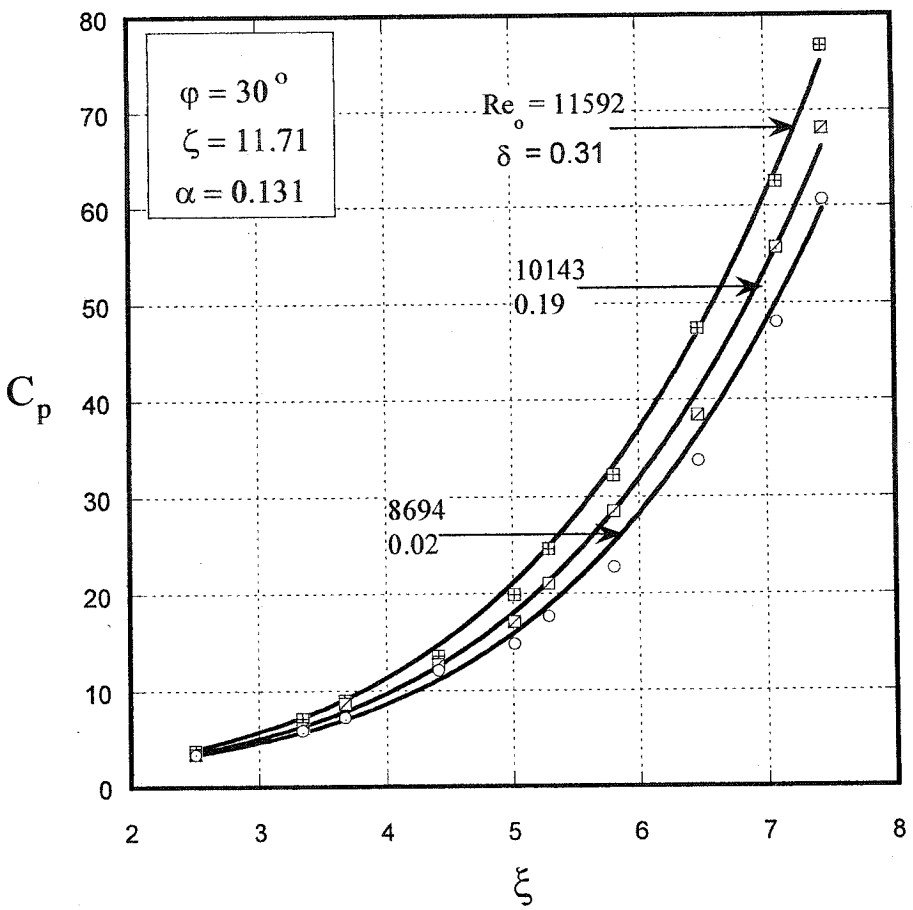

Figure (4-1-10): Pressure drop coefficient based on n=2 reverse vortex model for very long aspect ratio and an intermediate inlet angle ($\varphi = 30°$) chamber for different Reynolds numbers. The symbols refer to present experiment while the solid lines refer to present theory.

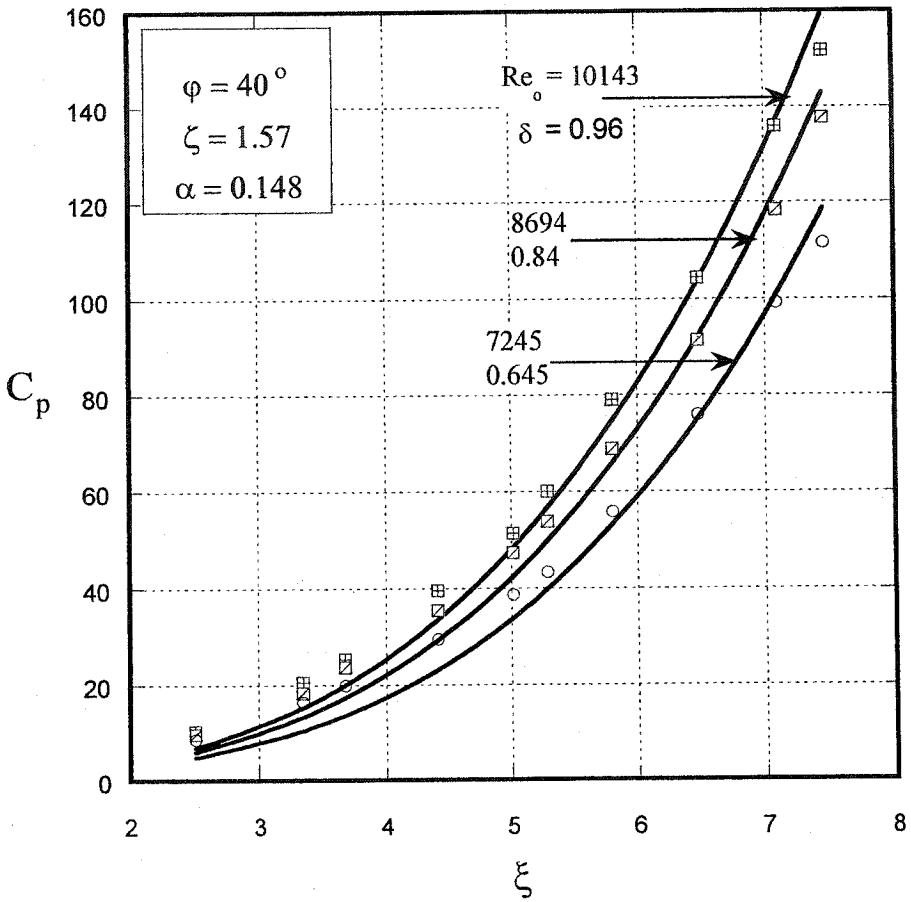

Figure (4-1-11): Pressure drop coefficient based on n=2 reverse vortex model in short aspect ratio chamber for an intermediate inlet angle (φ=40°) for different Reynolds numbers. The symbols refer to present experiment while the solid lines refer to present theory.

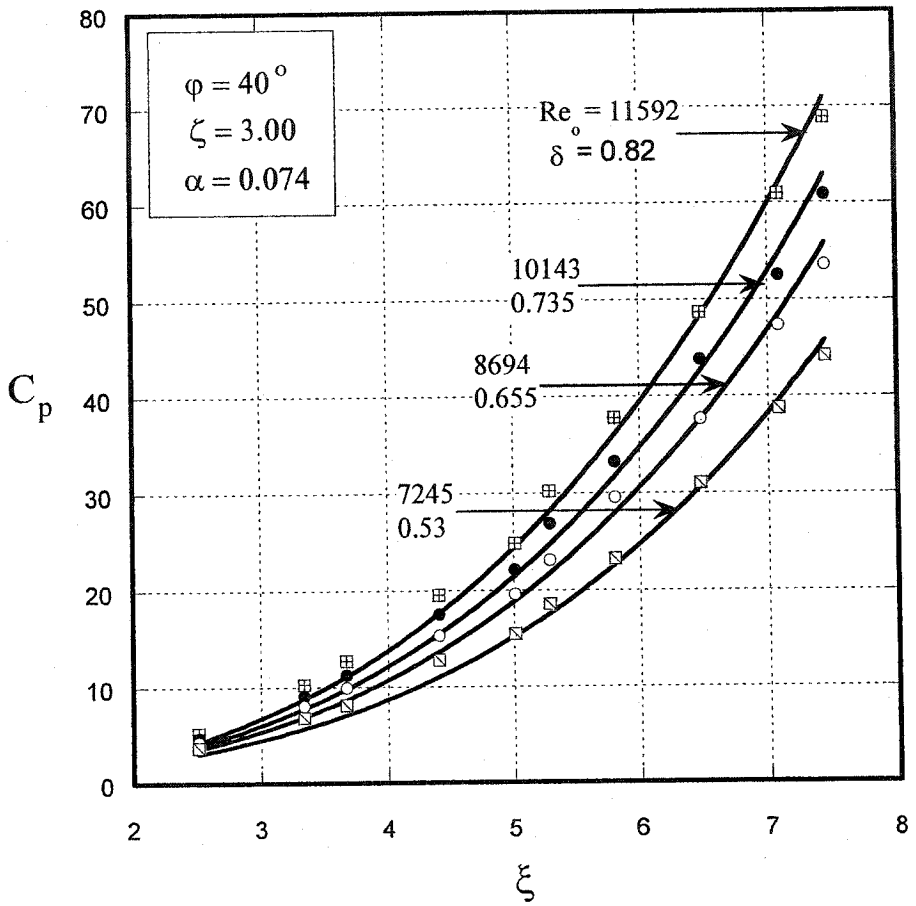

Figure (4-1-12): Pressure drop coefficient based on n=2 reverse vortex model in an intermediate aspect ratio chamber for an intermediate inlet angle ($\varphi = 40°$) for different Reynolds numbers. The symbols refer to present experiment while the solid lines refer to present theory.

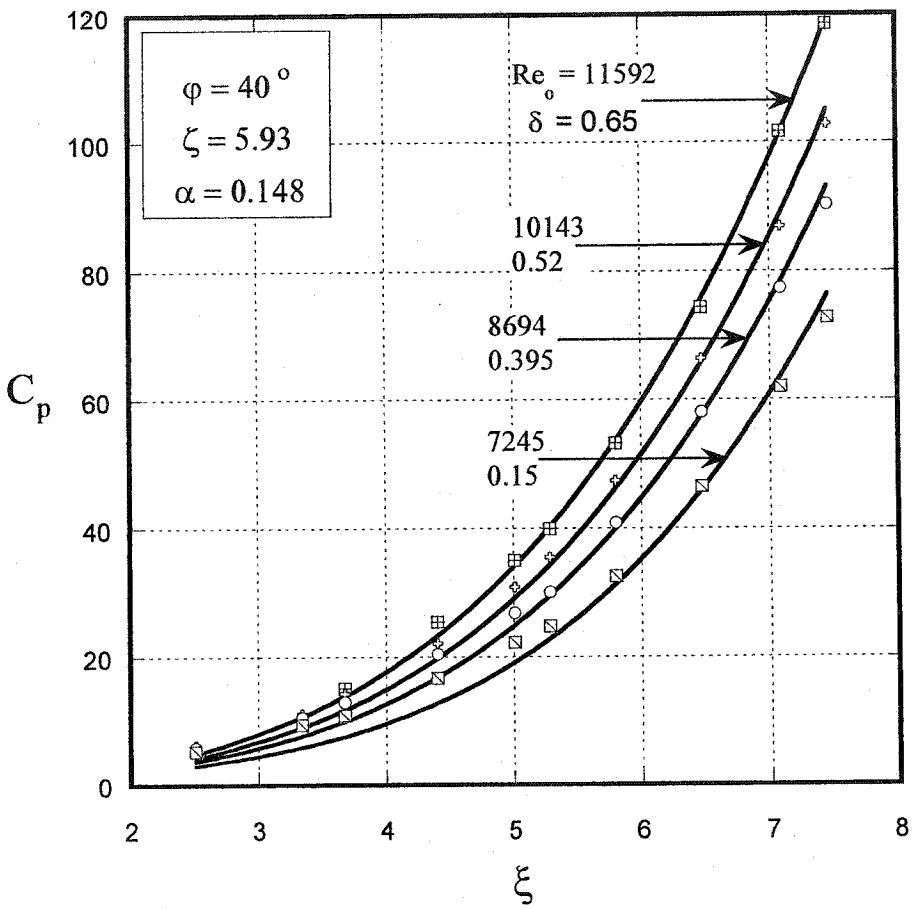

Figure (4-1-13): Pressure drop coefficient based on n=2 reverse vortex model in an intermediate aspect ratio and inlet angle ($\varphi = 40°$) chamber for different Reynolds numbers. The symbols refer to present experiment while the solid lines refer to present theory.

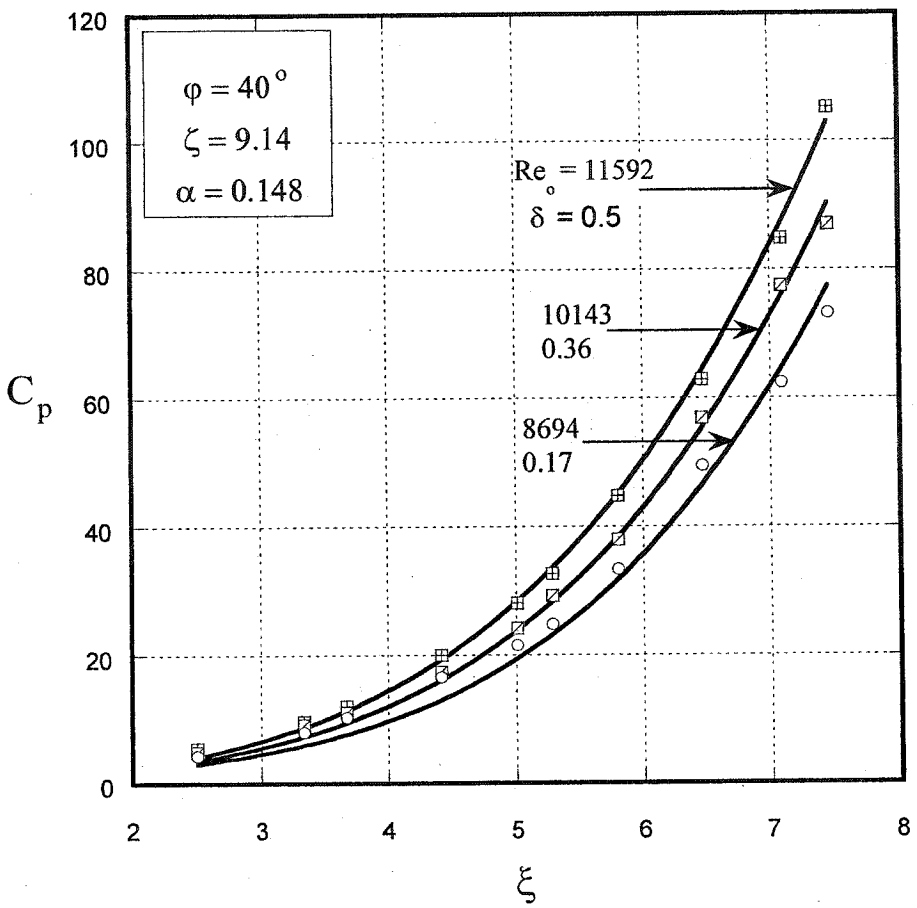

Figure (4-1-14): Pressure drop coefficient based on n=2 reverse vortex model for long aspect ratio and an intermediate inlet angle ($\varphi = 40°$) chamber for different Reynolds numbers. The symbols refer to present experiment while the solid lines refer to present theory.

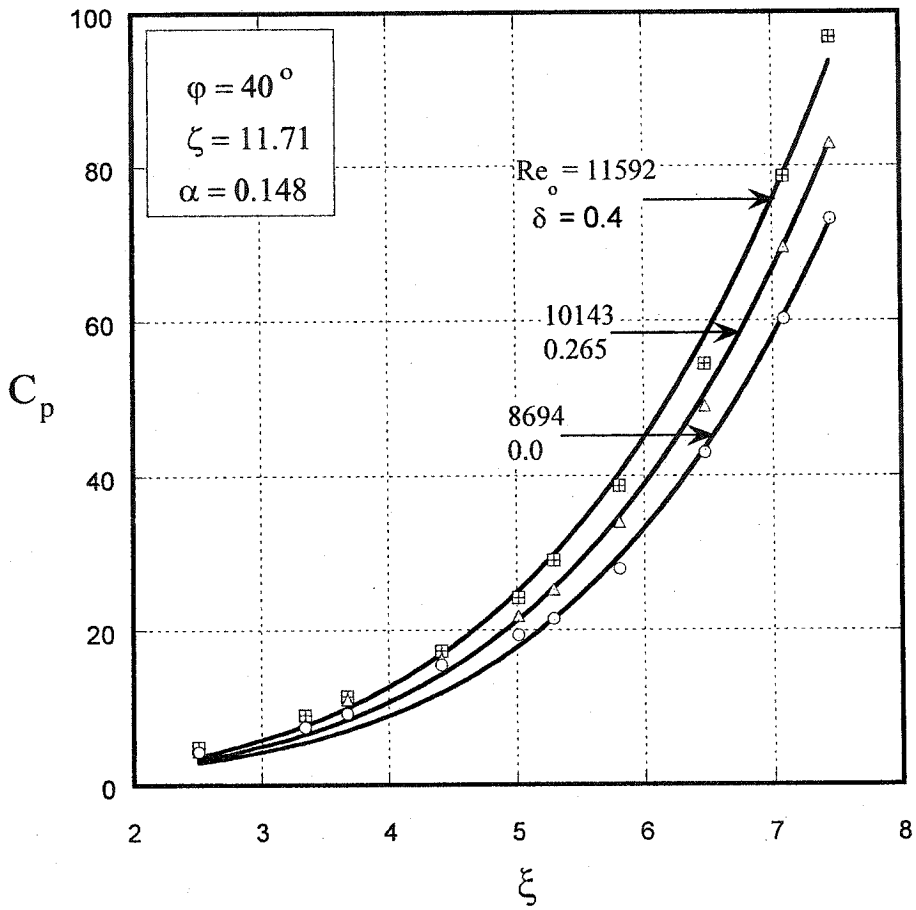

Figure (4-1-15): Pressure drop coefficient based on n=2 reverse vortex model for very long aspect ratio and an intermediate inlet angle ($\varphi = 40^\circ$) chamber for different Reynolds numbers. The symbols refer to present experiment while the solid lines refer to present theory.

There are no considerable changes in the pressure drop coefficient values for very long chambers and low Reynolds number. This conclusion is shown in figures (4-1-16) and (4-1-17) for configurations ($\varphi = 30^o, \alpha = 0.131$) and ($\varphi = 40^o, \alpha = 0.148$), at two aspect ratios ($\zeta = 11.71$ and $\zeta = 16.00$) and Reynolds number ($R_{eo} = 8694$). In this case the swirl intensity is very low, the swirl term effects almost approach zero, and the friction effect is very high. The flow field is controlled by the effects of the friction losses more than the swirl effects.

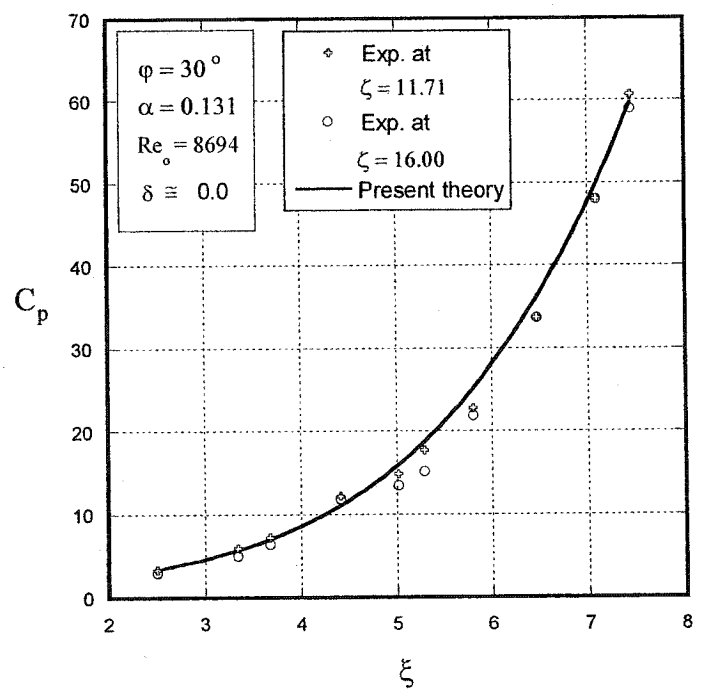

Figure (4-1-16): Pressure drop coefficient for very long chamber, low Reynolds number for $\varphi = 30^o$ swirler.

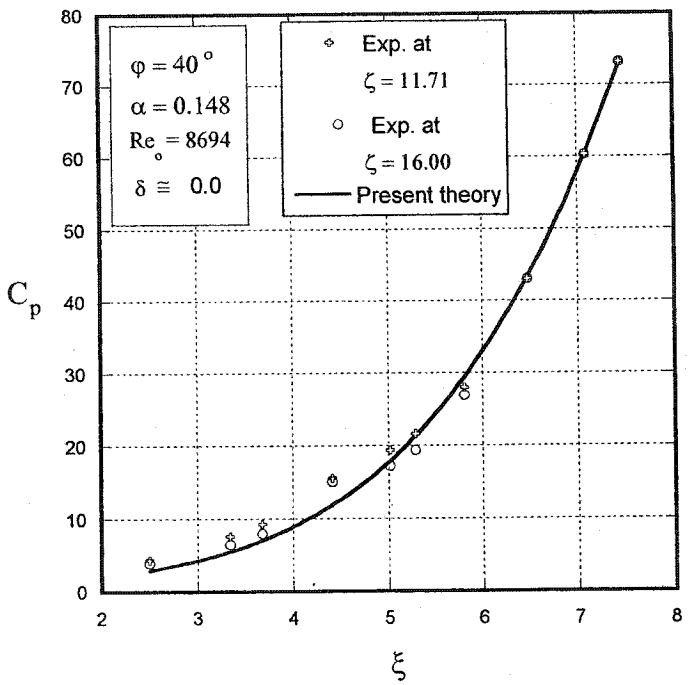

Figure (4-1-17): Pressure drop coefficient for very long chamber, low Reynolds number for $\varphi = 40^o$ swirler.

It is interesting to see how the vortex core size behaves. Figure (4-1-18) shows the theortical results of the vortex core size for configuration ($\varphi = 30^o, \alpha = 0.131$, $\zeta = 3.00$). At a specific Reynolds number as the diameter ratio (ξ) increases, the core size (χ) decreases. While if the diameter ratio is kept constant, the core size increases as the Reynolds number increases. In case where the diameter ratio (ξ) is increased, this means increasing the axial velocity magnitude. Therefore, the core size will have to contract in size in order to achieve the mass conservation principle which leads to increase the magnitude of the axial velocity.

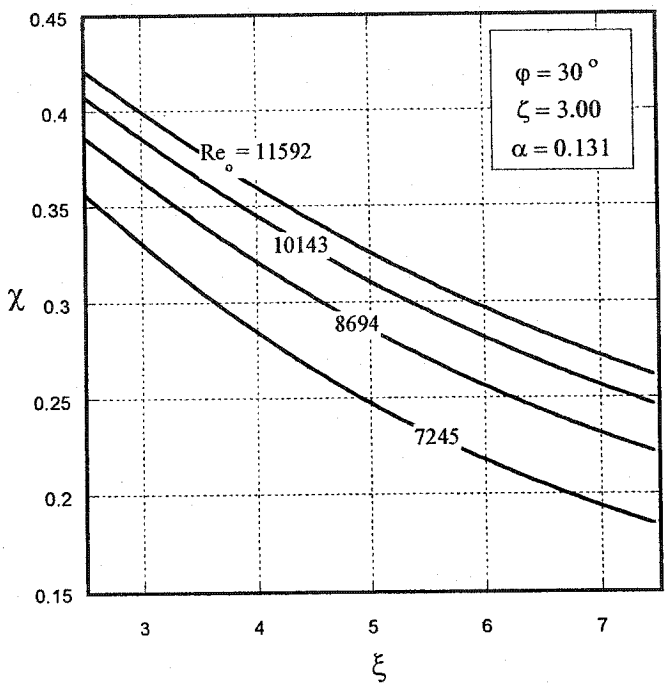

Figure (4-1-18): Core size vs the diameter ratio.

It is also of interest to see how the friction losses ($F_{friction}$) varies with the Reynolds number. Figure (4-1-19) shows the theortical results of the friction losses for configuration ($\varphi = 30^o, \alpha = 0.131, \zeta = 3.00$). At a specific Reynolds number as the diameter ratio (ξ) increases, the friction loss increases. While if the diameter ratio is kept constant, the friction increases as the Reynolds number decreases. This is expected because at low Reynolds number the viscosity effects are higher than the inertia effects.

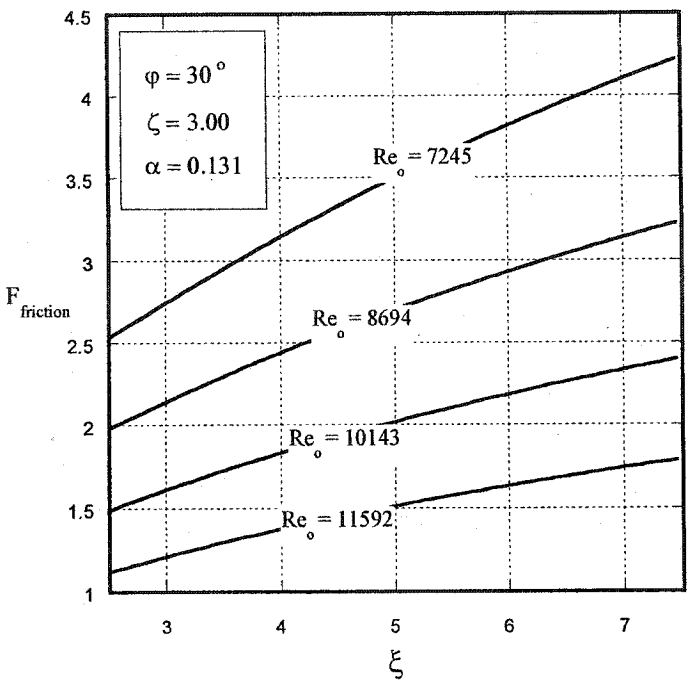

Figure (4-1-19): Friction loss vs the diameter ratio for different Reynolds numbers.

4-2: The n=2 Vortex Model for Non-Reverse Flow

The axial velocity profile at the exit port is assumed approximately a wake-like profile, based on n=2 reverse vortex model as ξ increases while R_{eo} is kept constant. The forced vortex core size (χ or R_c) and the free vortex size ($R_e - R_c$) contract, then the volumetric fractions (δ_1, δ_2) decrease, see figure (4-2-1), and the result is increasing $V_{z\,out}$ and $V_{z\,rev}$. As R_{eo} increases while ξ is kept constant, the core size (χ or R_c) expands and the free vortex size ($R_e - R_c$) contracts, reverse volumetric fractions (δ_1, δ_2) increase, and the result is increasing $V_{z\,out}$ and $V_{z\,rev}$.

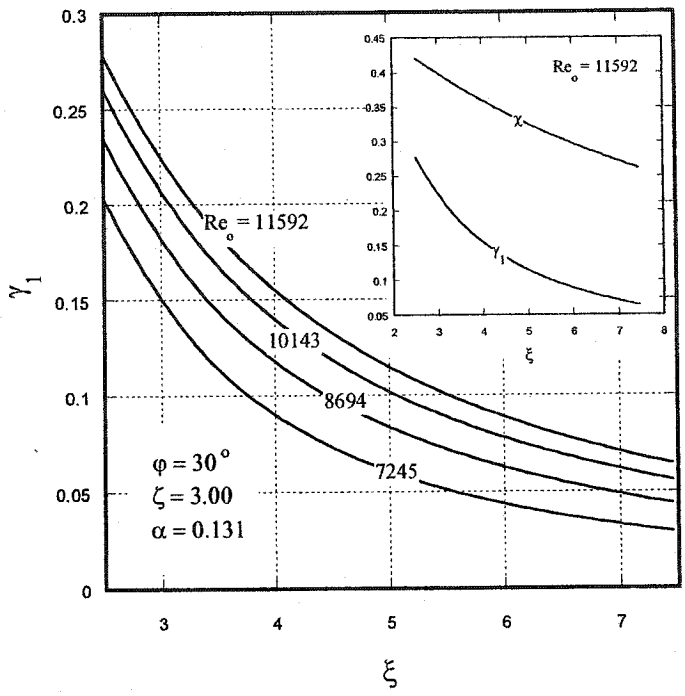

Figure (4-2-1): Volumetric fraction for different Reynolds numbers.

In the case where the flow behaves as a wake-like, approximately without axial reversal flow or $\gamma_2 \approx 1$ .Therefore equation (3-5) can be reduced to:

$$C_p = \delta^2 \cos^2(\varphi)\, \xi^2 \frac{Ln\left[\frac{1}{2}\left\{1+\frac{1}{\chi^4}\right\}\right]}{2(1-\chi^2)} + \alpha^2 \xi^4 \frac{1}{(1-\chi^2)^2}$$

$$+ \cos^2(\varphi)\,(1-\delta^2) \frac{Ln\left[\frac{1}{2}\left\{1+\left(\frac{\xi}{\chi}\right)^4\right\}\right]}{2\left[1-\left(\frac{\chi}{\xi}\right)^2\right]} - 1 \qquad (4\text{-}1)$$

Solving this equation with the minimum principle, the results for all configurations are shown in figures (4-2-2) to (4-2-14). The theory here suggests that the δ values are higher than n=2 reverse vortex model.

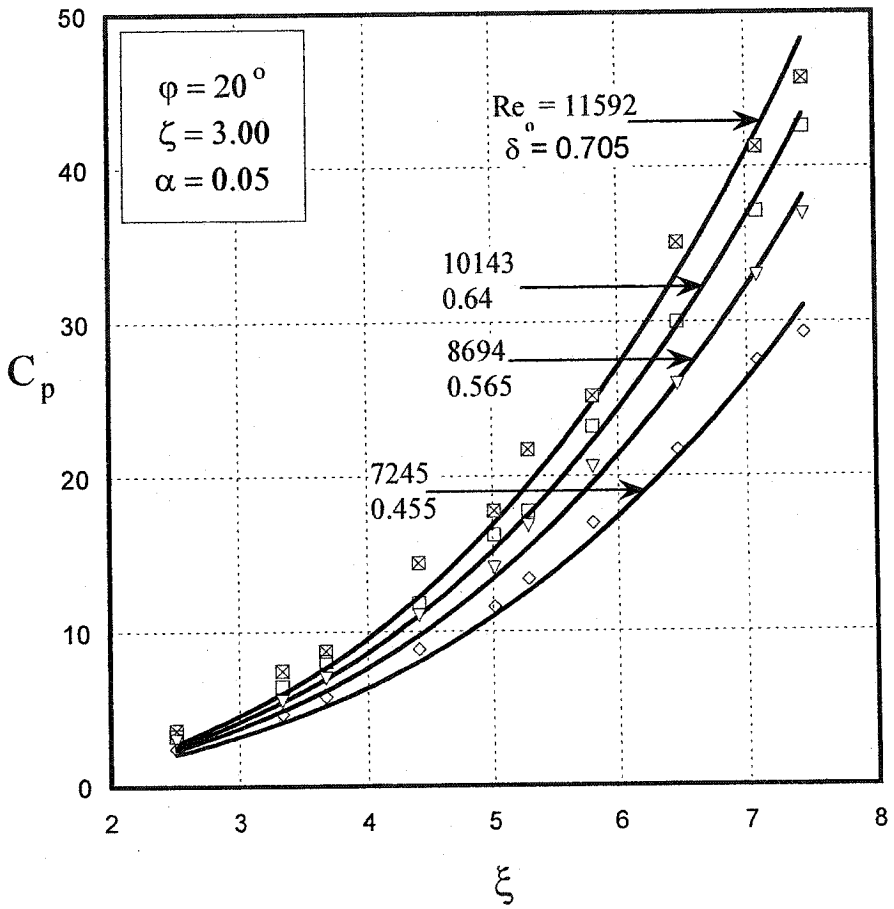

Figure (4-2-2): Pressure drop coefficient based on n=2 non-reverse vortex model in an intermediate aspect ratio chamber for a small inlet ($\varphi = 20°$) angle for different Reynolds numbers. The symbols refer to present experiment while the solid lines refer to present theory.

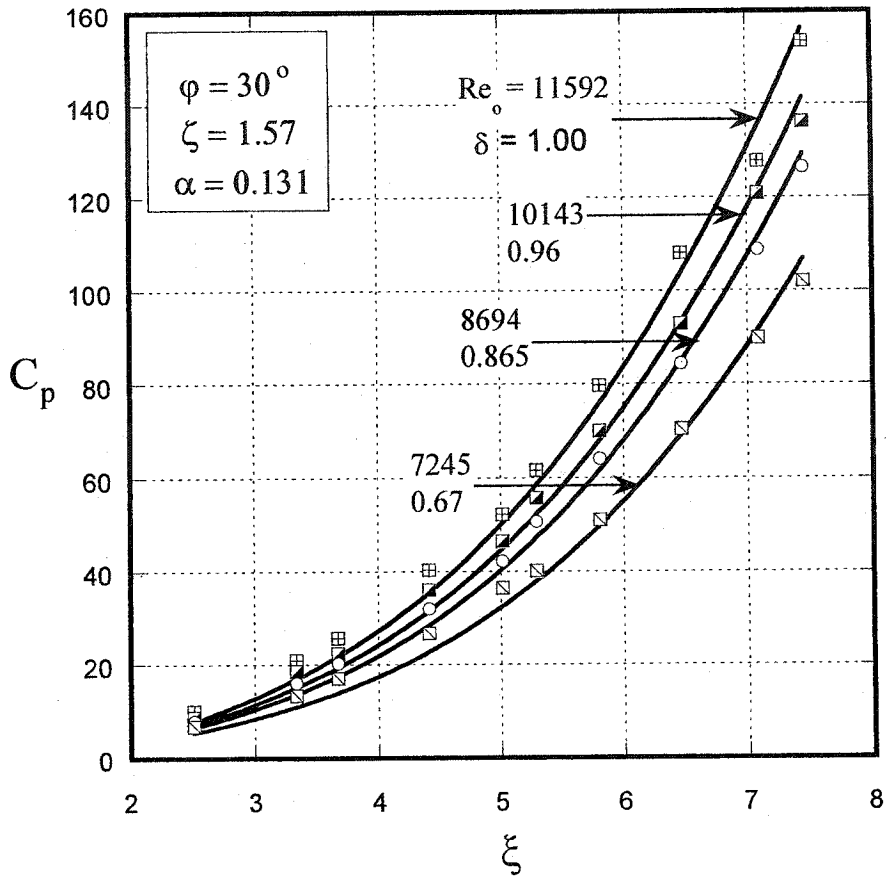

Figure (4-2-3): Pressure drop coefficient based on n=2 non-reverse vortex model in short aspect ratio chamber for an intermediate inlet angle (φ=30°) for different Reynolds numbers. The symbols refer to present experiment while the solid lines refer to present theory.

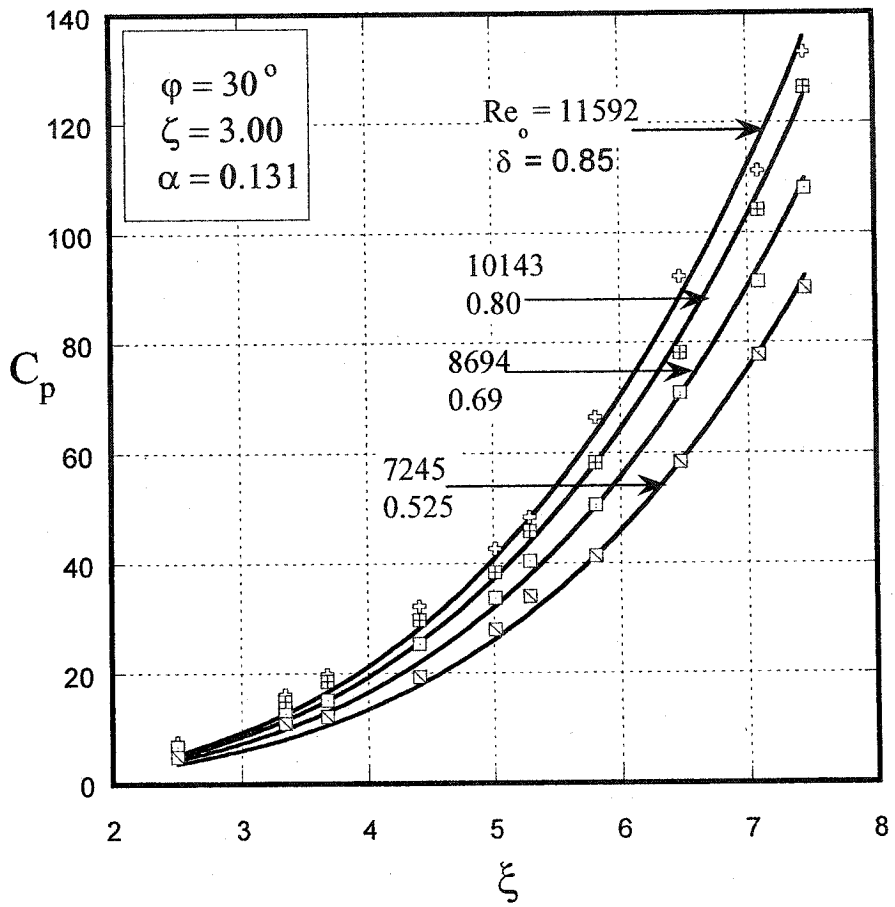

Figure (4-2-4): Pressure drop coefficient based on n=2 non-reverse vortex model in an intermediate aspect ratio chamber and inlet angle (φ=30°) for different Reynolds numbers. The symbols refer to present experiment while the solid lines refer to present theory.

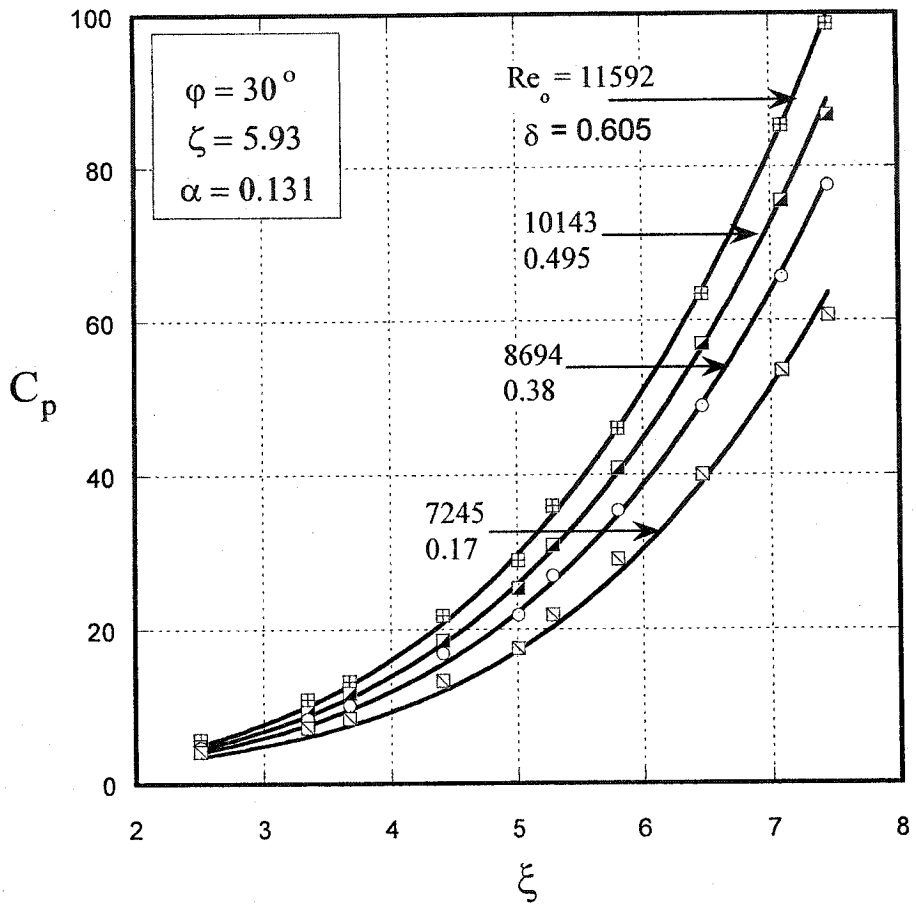

Figure (4-2-5): Pressure drop coefficient based on n=2 non-reverse vortex model in an intermediate aspect ratio and inlet angle ($\varphi = 30^\circ$) chamber for different Reynolds numbers. The symbols refer to present experiment while the solid lines refer to present theory.

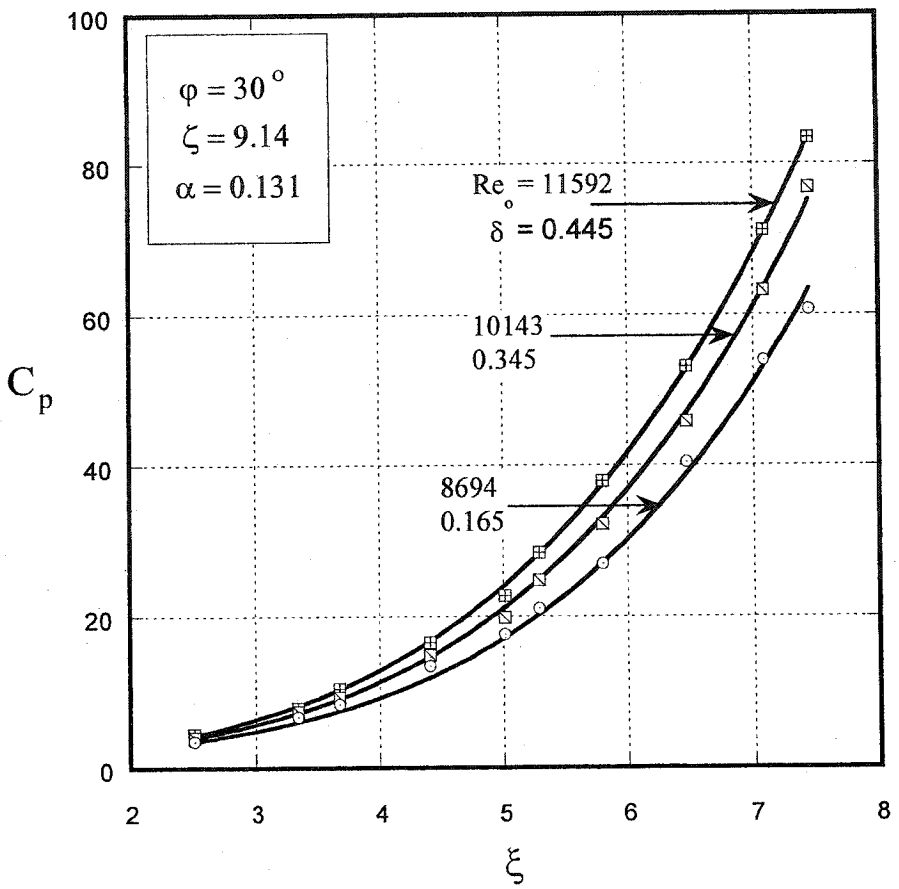

Figure (4-2-6): Pressure drop coefficient based on n=2 non-reverse vortex model for long aspect ratio and an intermediate inlet angle (φ=30°) chamber for different Reynolds numbers. The symbols refer to present experiment while the solid lines refer to present theory.

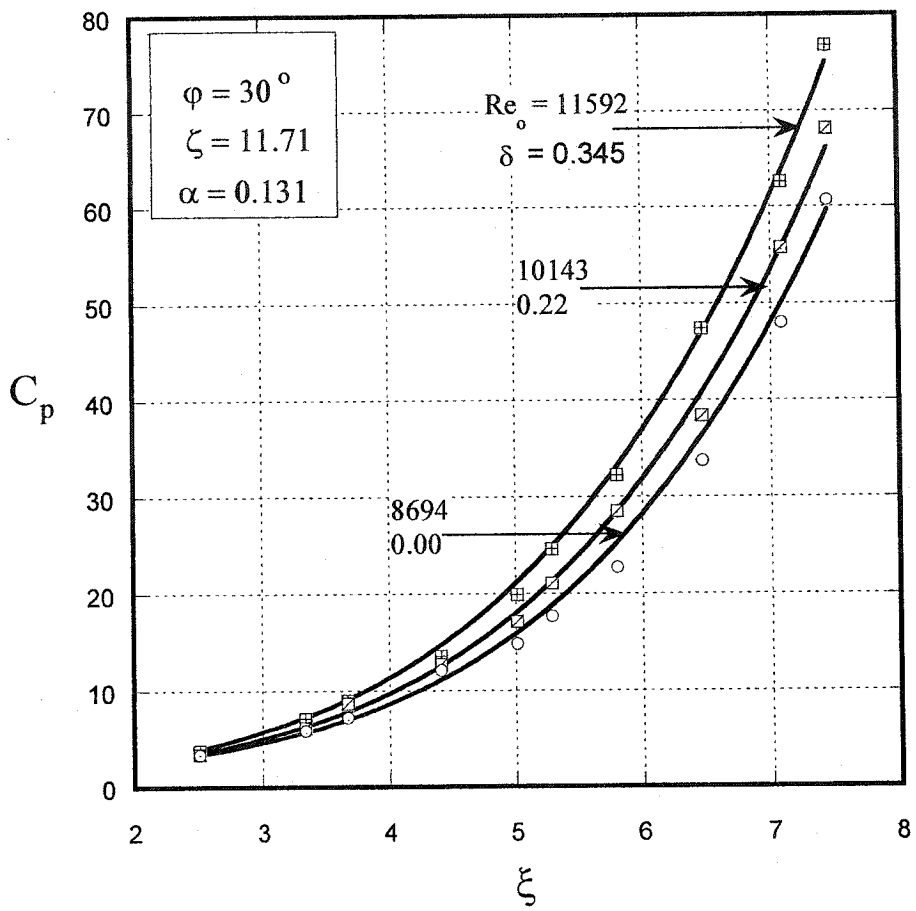

Figure (4-2-7): Pressure drop coefficient based on n=2 non-reverse vortex model for very long aspect ratio and an intermediate inlet angle (φ=30°) chamber for different Reynolds numbers. The symbols refer to present experiment while the solid lines refer to present theory.

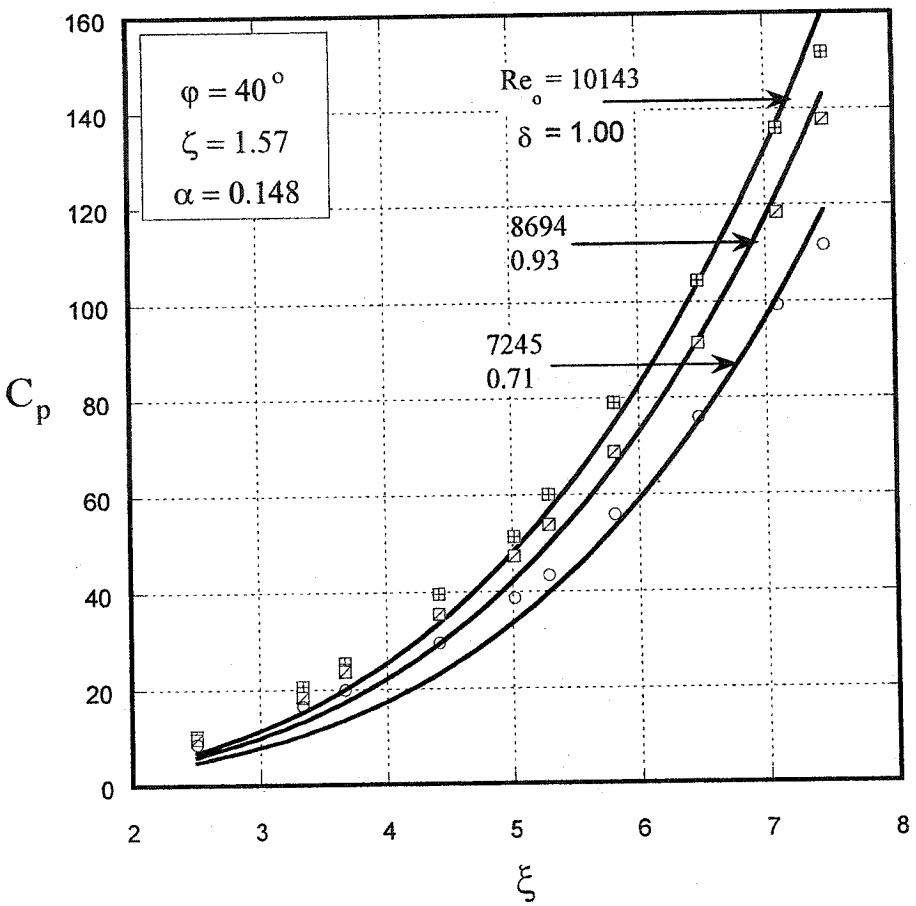

Figure (4-2-8): Pressure drop coefficient based on n=2 non-reverse vortex model in short aspect ratio chamber for an intermediate inlet angle ($\varphi = 40^\circ$) for different Reynolds numbers. The symbols refer to present experiment while the solid lines refer to present theory.

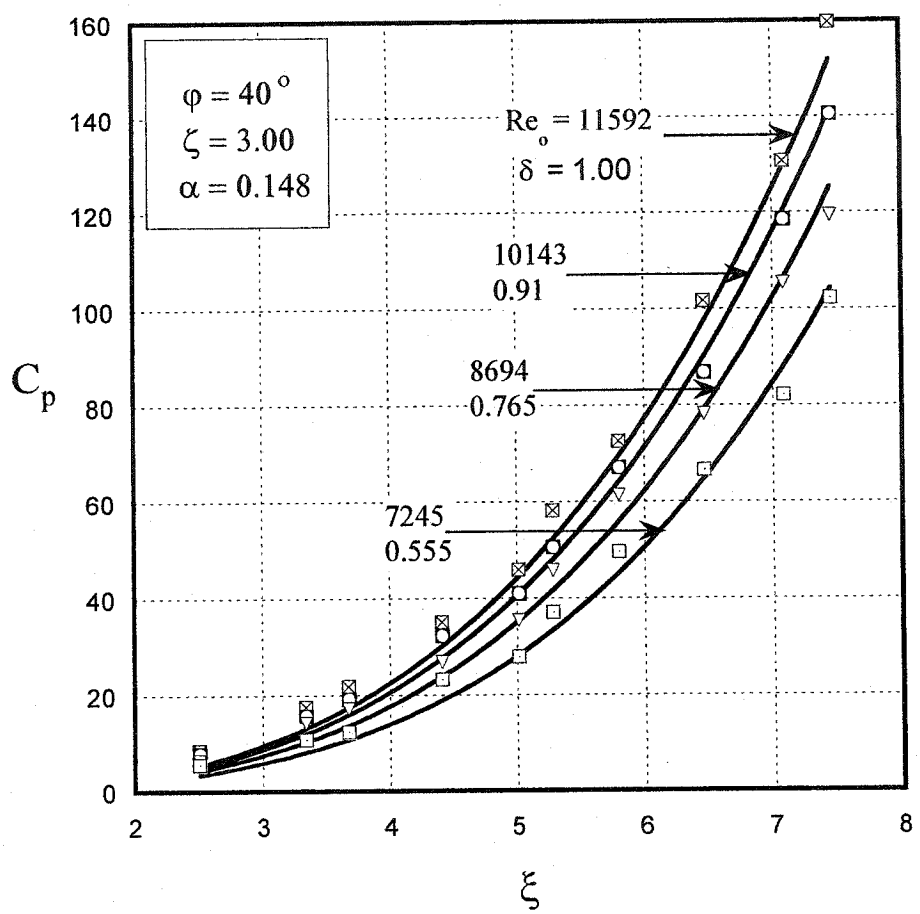

Figure (4-2-9): Pressure drop coefficient based on n=2 non-reverse vortex model in an intermediate aspect ratio chamber and inlet angle ($\varphi = 40°$) for different Reynolds numbers. The symbols refer to present experiment while the solid lines refer to present theory.

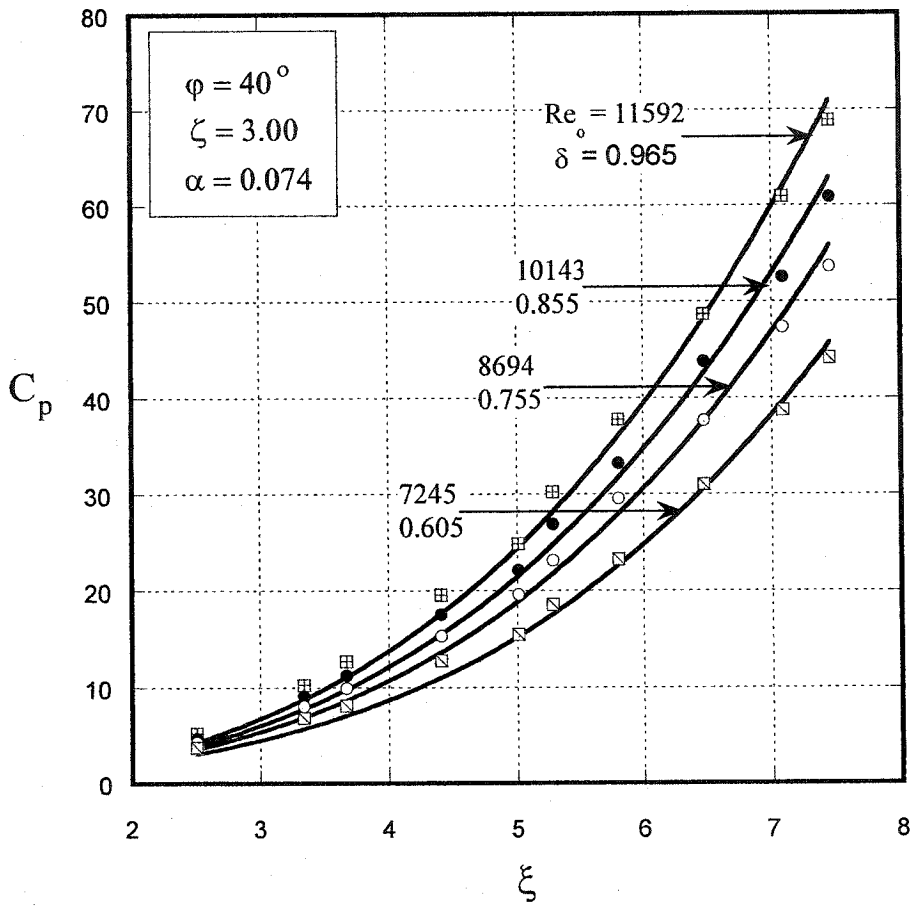

Figure (4-2-10): Pressure drop coefficient based on n=2 non-reverse vortex model in an intermediate aspect ratio chamber and inlet angle ($\varphi = 40°$) for different Reynolds numbers. The symbols refer to present experiment while the solid lines refer to present theory.

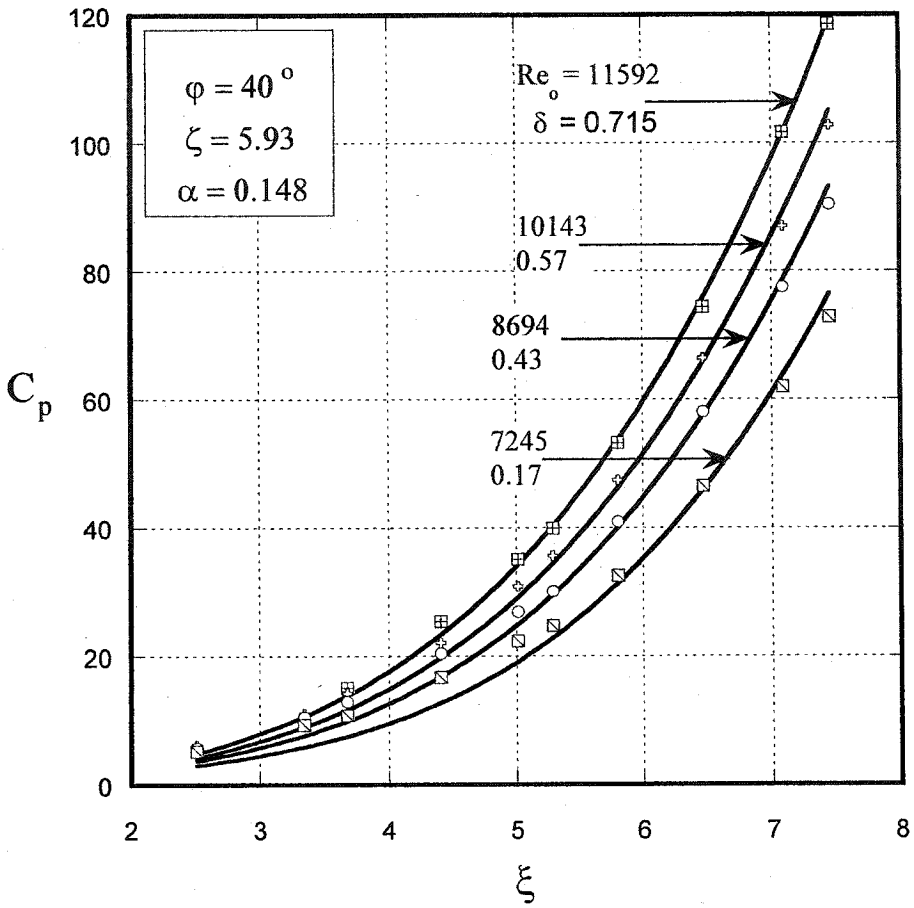

Figure (4-2-11): Pressure drop coefficient based on n=2 non-reverse vortex model in an intermediate aspect ratio chamber and inlet angle ($\varphi = 40°$) for different Reynolds numbers. The symbols refer to present experiment while the solid lines refer to present theory.

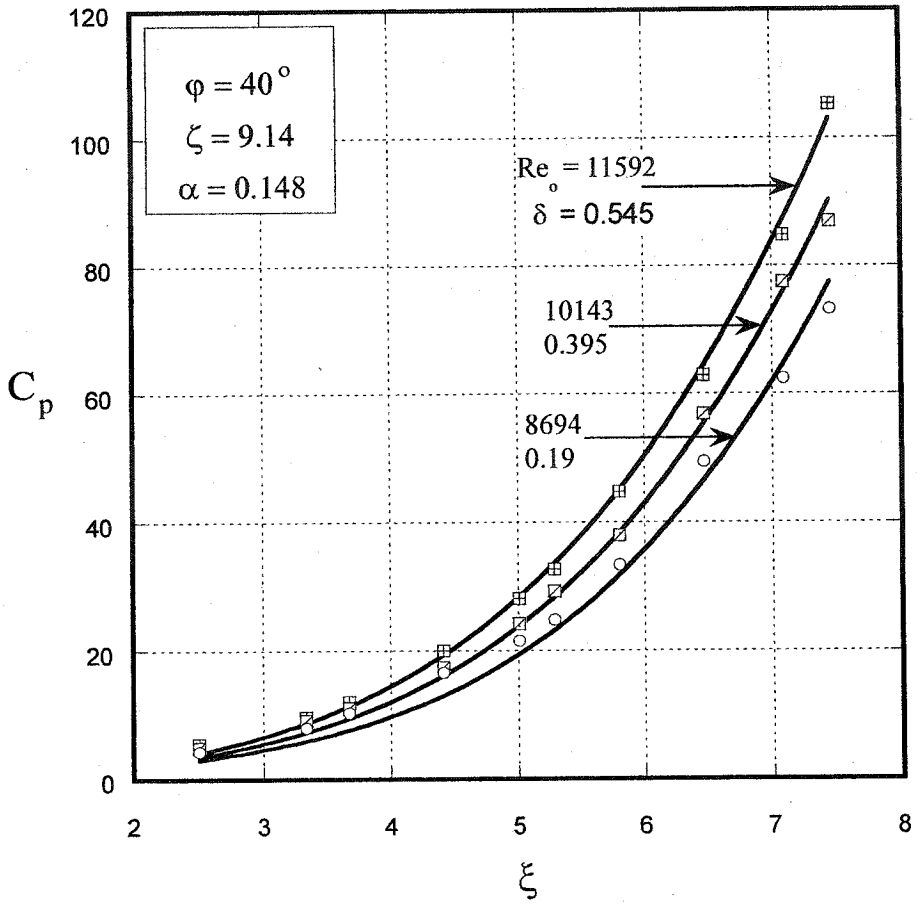

Figure (4-2-12): Pressure drop coefficient based on n=2 non-reverse vortex model for long aspect ratio and an intermediate inlet angle ($\varphi = 40°$) chamber for different Reynolds numbers. The symbols refer to present experiment while the solid lines refer to present theory.

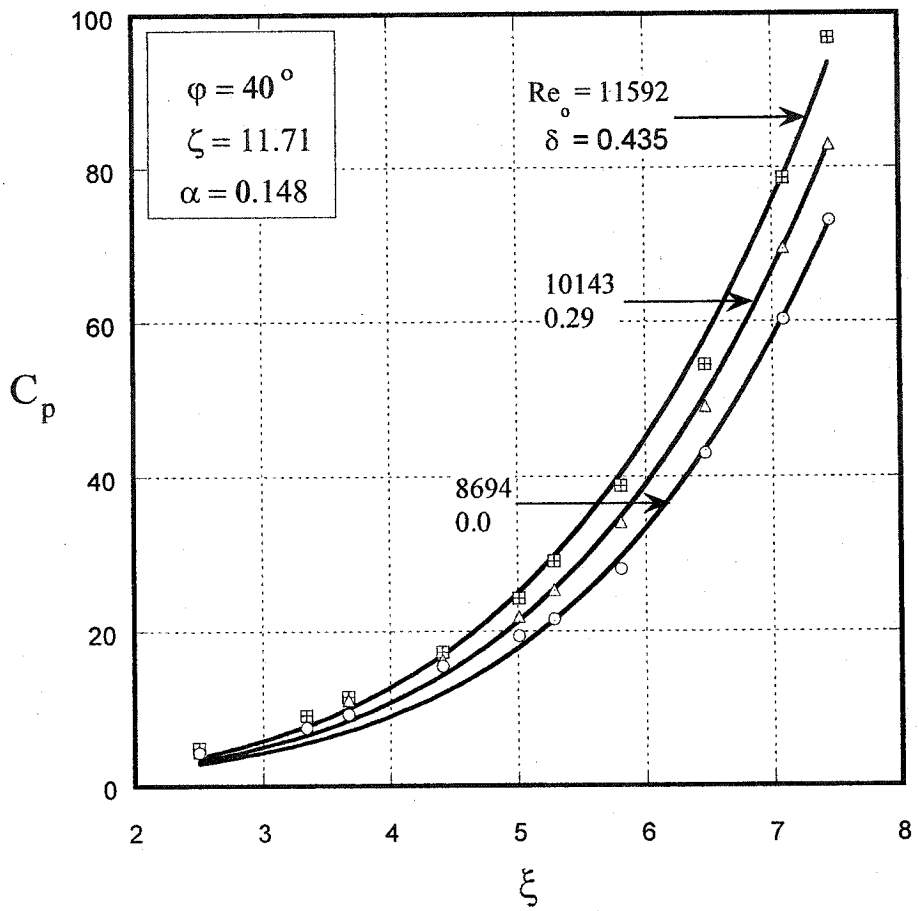

Figure (4-2-13): Pressure drop coefficient based on n=2 non-reverse vortex model for very long aspect ratio and an intermediate inlet angle ($\varphi = 40°$) chamber for different Reynolds numbers. The symbols refer to present experiment while the solid lines refer to present theory.

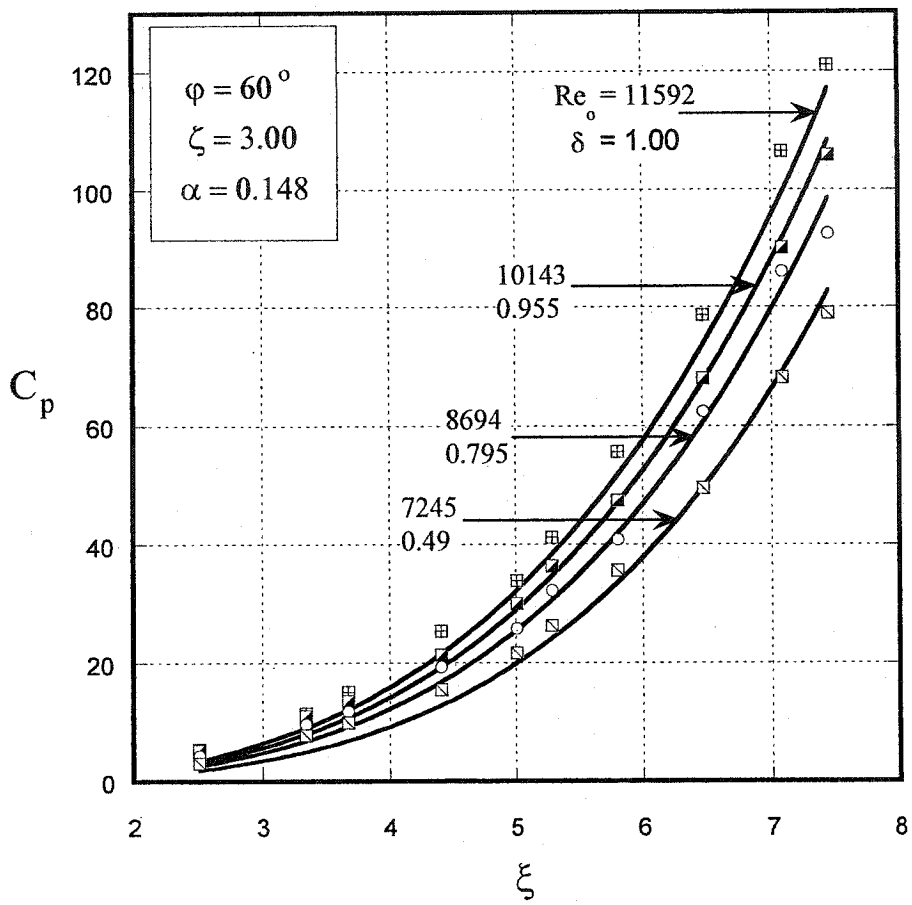

Figure (4-2-14): Pressure drop coefficient based on n=2 non-reverse vortex model in an intermediate aspect ratio chamber for large inlet angle (φ=60°) for different Reynolds numbers. The symbols refer to present experiment while the solid lines refer to present theory.

4-3: Free Vortex Model

First, consider the pressure drop across a chamber with configuration $\varphi=20^o, \alpha=0.05$, $\zeta=3.00$ where the flow field is expected to be under intense swirl conditions. The results for this case are shown in figure (4-3-1). A good correlation between the present theory and experiment is evident as the maximum difference between the theory and the experiment is less than 10%. A similar level of correlation is also the case for configurations ($\varphi=30^o, \alpha=0.131, \zeta=3.00$), and ($\varphi=40^o$, $\alpha=0.148$, $\zeta=3.00$), see figures (4-3-2) and (4-3-3), when ξ is larger than say 5 and 6 respectively. For all the three cases the conformity of the analytical result to the observations is better in the region of high ξ values.

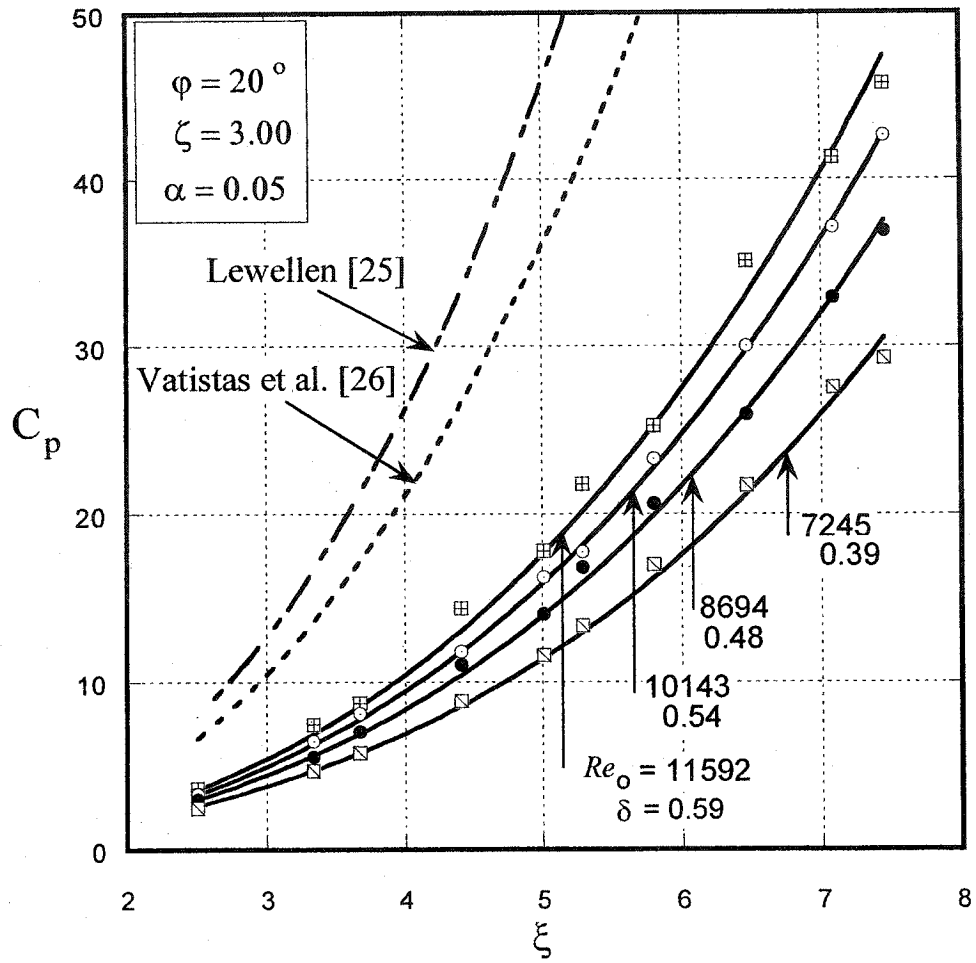

Figure (4-3-1): Pressure drop coefficient based on free vortex model in an intermediate aspect ratio chamber for a small inlet angle ($\varphi = 20°$) for different Reynolds numbers. The symbols refer to present experiment while the solid lines refer to present theory.

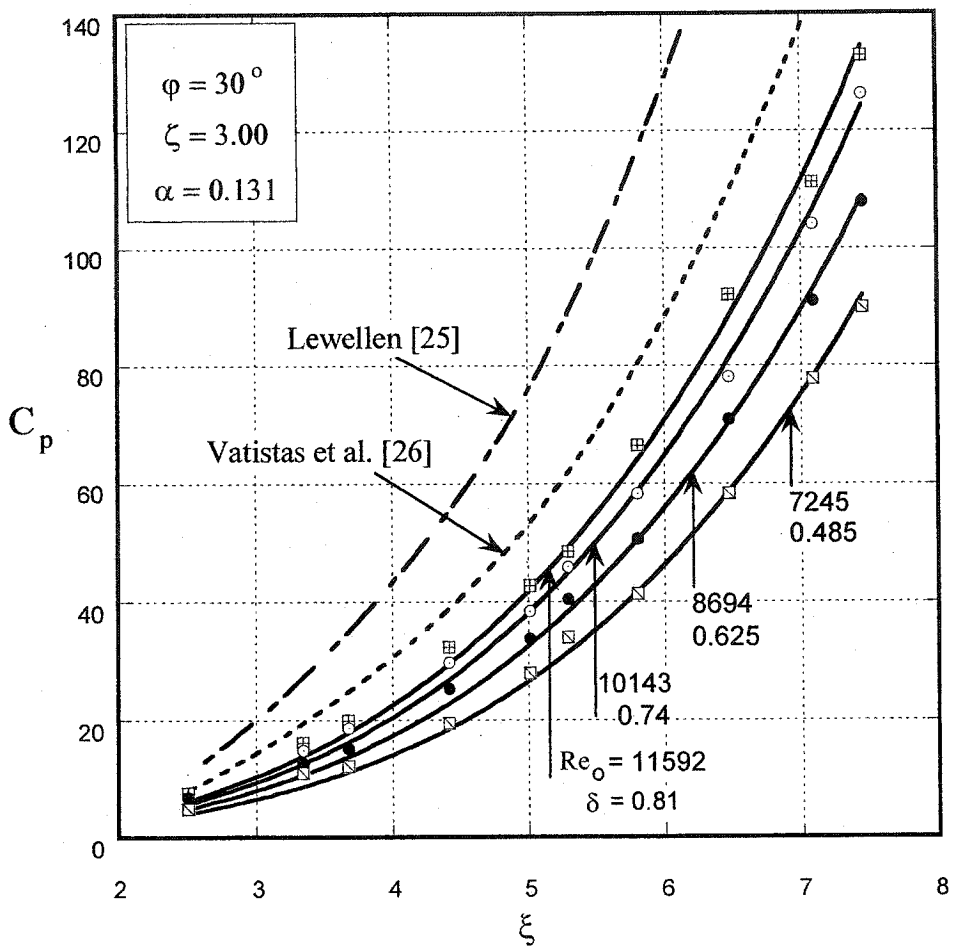

Figure (4-3-2): Pressure drop coefficient based on free vortex model in an intermediate aspect ratio chamber and inlet angle (φ=30°) for different Reynolds numbers. The symbols refer to present experiment while the solid lines refer to present theory.

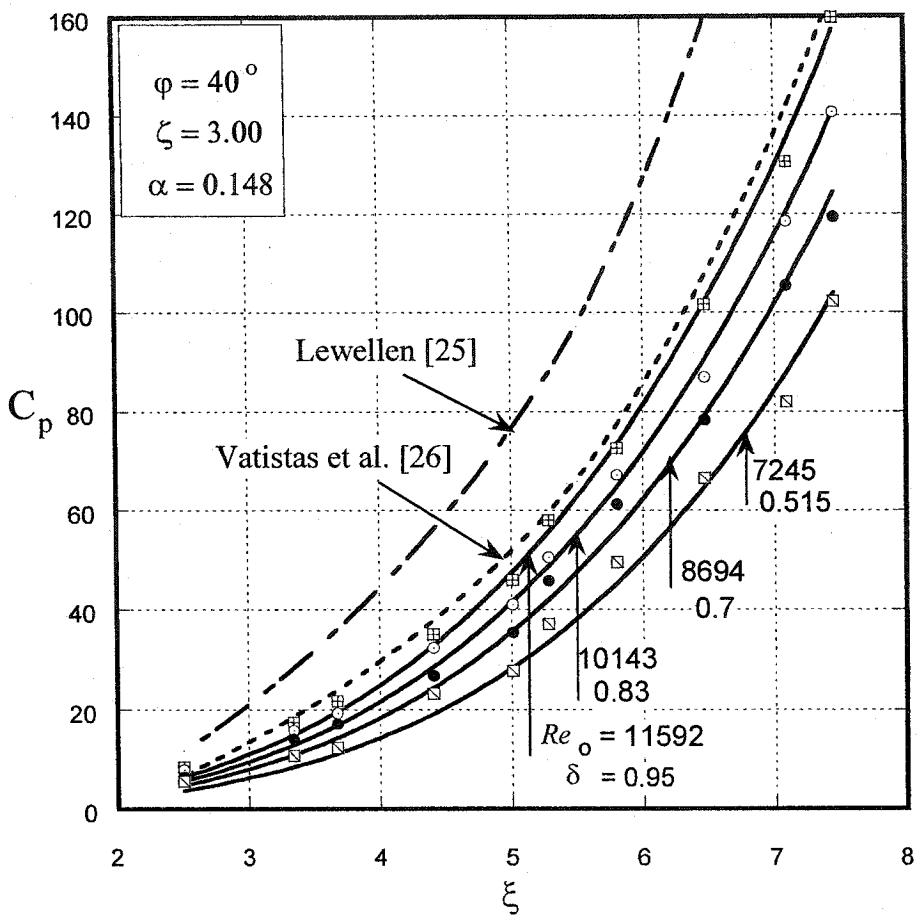

Figure (4-3-3): Pressure drop coefficient based on free vortex model in an intermediate aspect ratio chamber and inlet angle ($\varphi = 40°$) for different Reynolds numbers. The symbols refer to present experiment while the solid lines refer to present theory.

As in n=2 vortex model, Any of the previous graphs figures (4-3-1) to (4-3-3) point out that δ increases with R_{eo} tending towards one for larger R_{eo} values. The last makes the pressure profiles to approach the formulation of Vatistas et al [26] which assumes a δ = 1.00. This propensity is amply evident for configuration ($\varphi = 40^o$, $\alpha = 0.148$, $\zeta = 3.00$), see figure (4-3-2), where the pressure coefficient is seen to come within the reach of Vatistas et al. [26].

Figure (4-3-4) shows the percentage different error at R_{eo}=10143 for different swirlers ($\varphi = 20^o, 30^o, 40^o, 60^o$). At very low contraction ratio (i.e ξ=2.5) the error reach 42% which is the worst case for the 60^o swirler, while at the same contraction ratio the error approach zero for the 20^o swirler. When the contraction ratio $\xi > 4.5$, the percentage error is less than 5% for all swirlers.

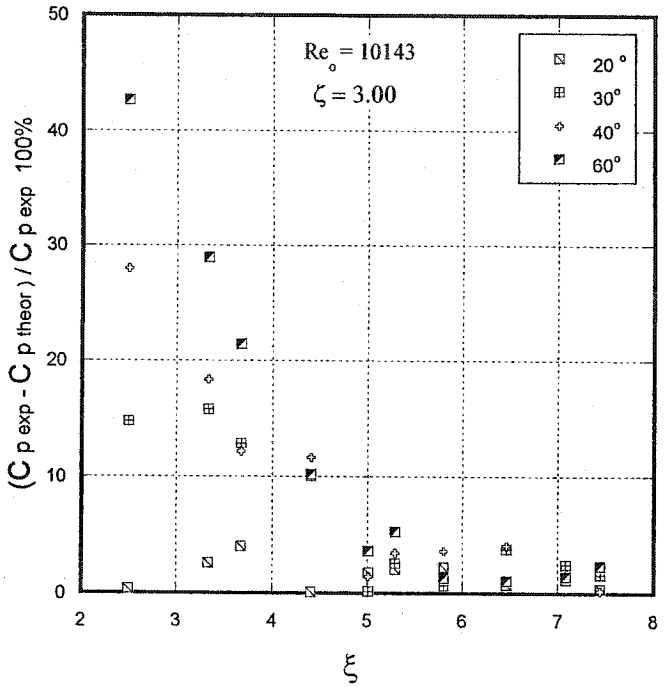

Figure (4-3-4): Percentage error criteria.

Having demonstrated that the present theoretical formulation can reasonably correlate the pressure drop in a vortex chamber, the following examines analytically a number of flow features. The pressure drop, see equation (3-11), is made up from the axial inertial term,

$$A_{axial} = \frac{\alpha^2 \xi^4}{(1-\chi^2)^2}$$

the swirl term,

$$S_{swirl} = -2 \frac{\delta^2 \xi^2 \cos^2(\varphi) \ln(\chi)}{(1-\chi^2)}$$

and the friction term,

$$F_{friction} = -2 \frac{(1-\delta^2)\ \cos^2(\varphi)\ \ln\left(\frac{\chi}{\xi}\right)}{1-\left(\frac{\chi}{\xi}\right)^2}$$

From figure (4-3-5), as ξ increases and in order to minimize the pressure drop across the chamber, the vortex core χ reduces, but the effective outlet area σ,

$$\sigma = \frac{A_e}{A_o} = \frac{1-\chi^2}{\xi^2}$$

contracts, giving rise to the increase of the inertia term. Since the core always occurs between $0 < \chi_c < 1.0$, as ξ becomes larger the vortex is focused, the swirl term increases and the frictional effects rise also. For $\xi < 1.5$ (large exit port diameter) the $F_{friction}$ term is significant while the A_{axial} is negligibly small in comparison to the other two terms. For $\xi > 1.5$ the A_{axial} term begins to overtake friction, while for $\xi > \sim 6.8$ surpasses even S_{swirl}.

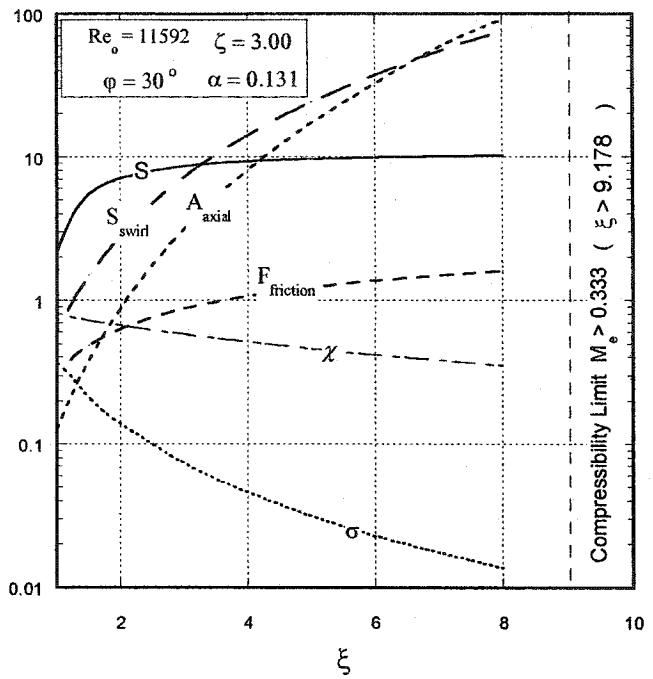

Figure (4-3-5): Variation of various flow components in a typical chamber.

Traditionally the degree of swirl in a given flow field is expressed by the swirl number S which is defined in Gupta et al [1] and is given by:

$$S = \frac{2\delta\cos(\varphi)}{\alpha}\left(1 - \frac{\chi_c}{\xi}\right)$$

For the first configuration where the swirl is the strongest the current analytical development is applicable for the full set of data. The previously mentioned good correlation between the theory and the experiment is achieved for larger values of S (say 10).

The pressure drop coefficients for different configurations for the free vortex model are given in figures (4-3-6) to (4-3-15).

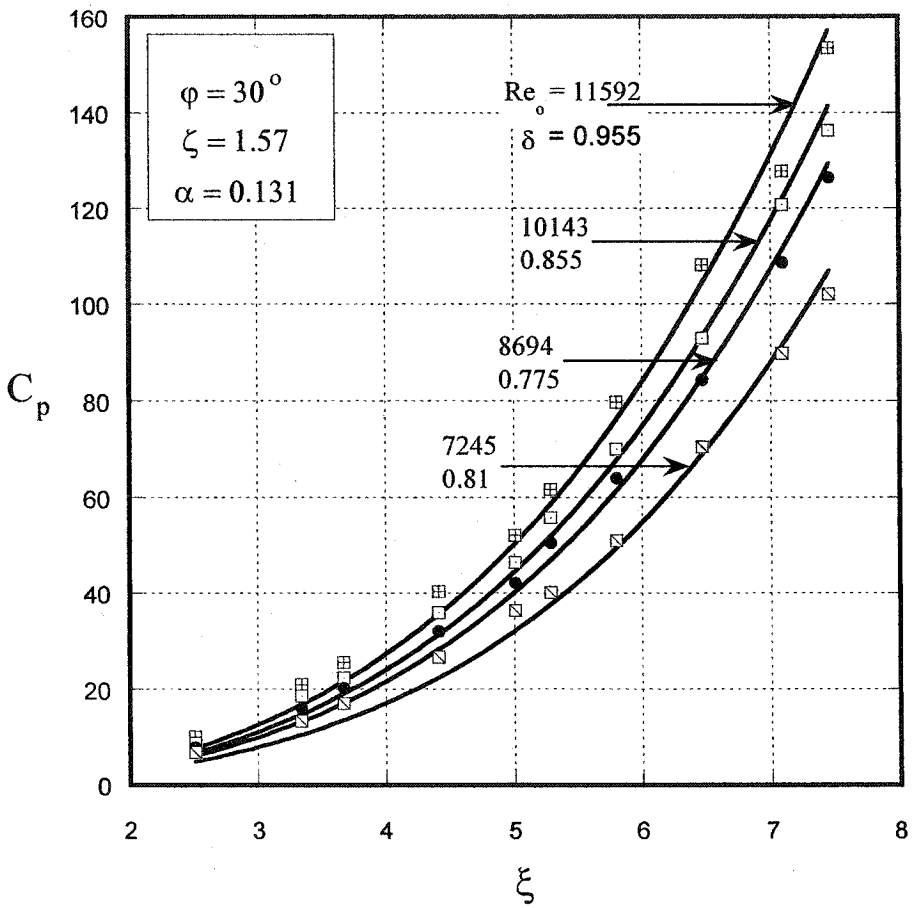

Figure (4-3-6): Pressure drop coefficient based on free vortex model in short aspect ratio chamber for an intermediate inlet angle ($\varphi = 30°$) for different Reynolds numbers. The symbols refer to present experiment while the solid lines refer to present theory.

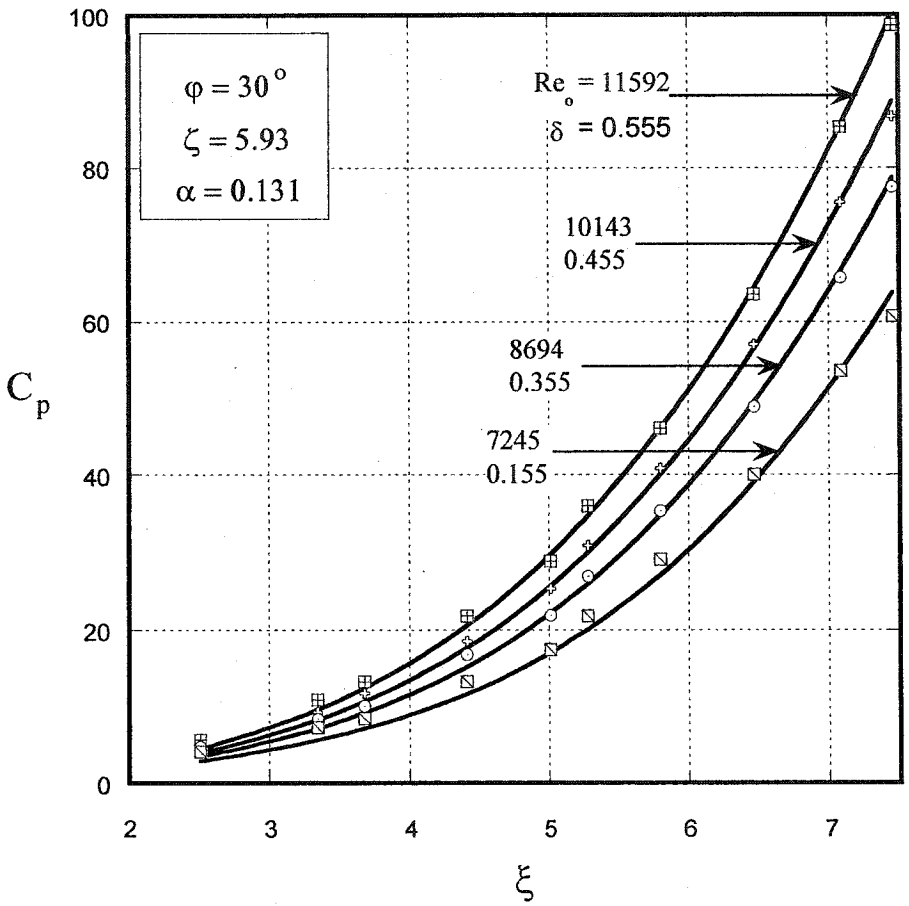

Figure (4-3-7): Pressure drop coefficient based on free vortex model in an intermediate aspect ratio and inlet angle (φ=30°) chamber for different Reynolds numbers. The symbols refer to present experiment while the solid lines refer to present theory.

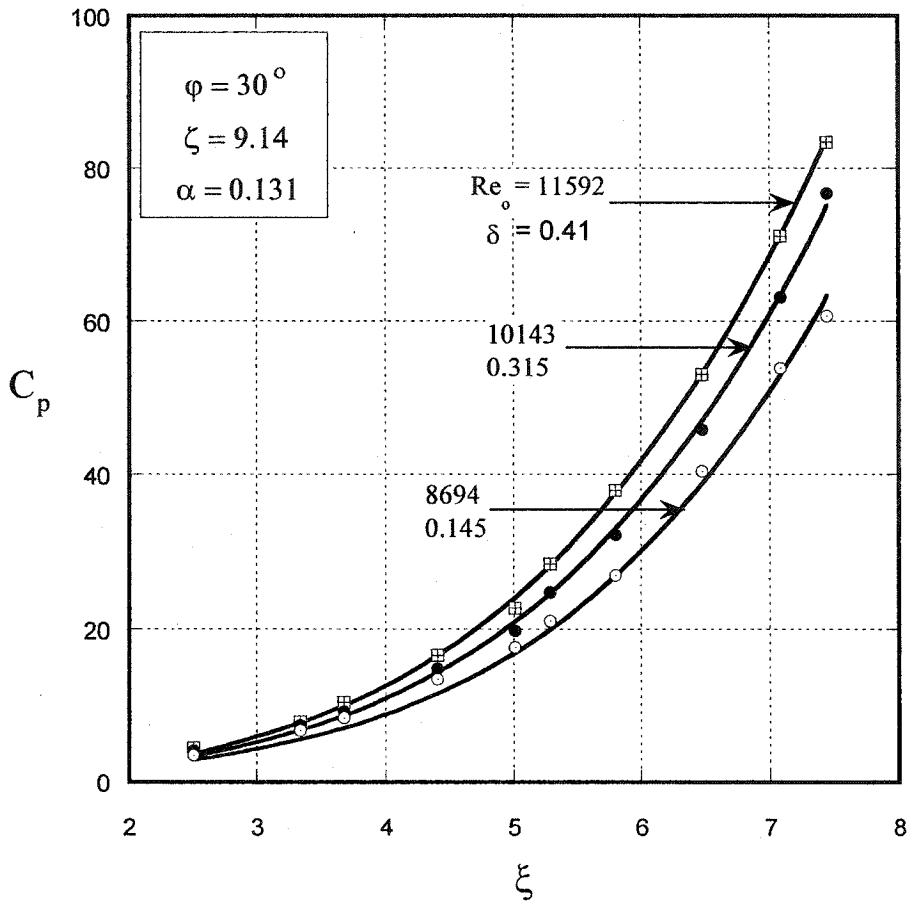

Figure (4-3-8): Pressure drop coefficient based on free vortex model for long aspect ratio and an intermediate inlet angle ($\varphi = 30^\circ$) chamber for different Reynolds numbers. The symbols refer to present experiment while the solid lines refer to present theory.

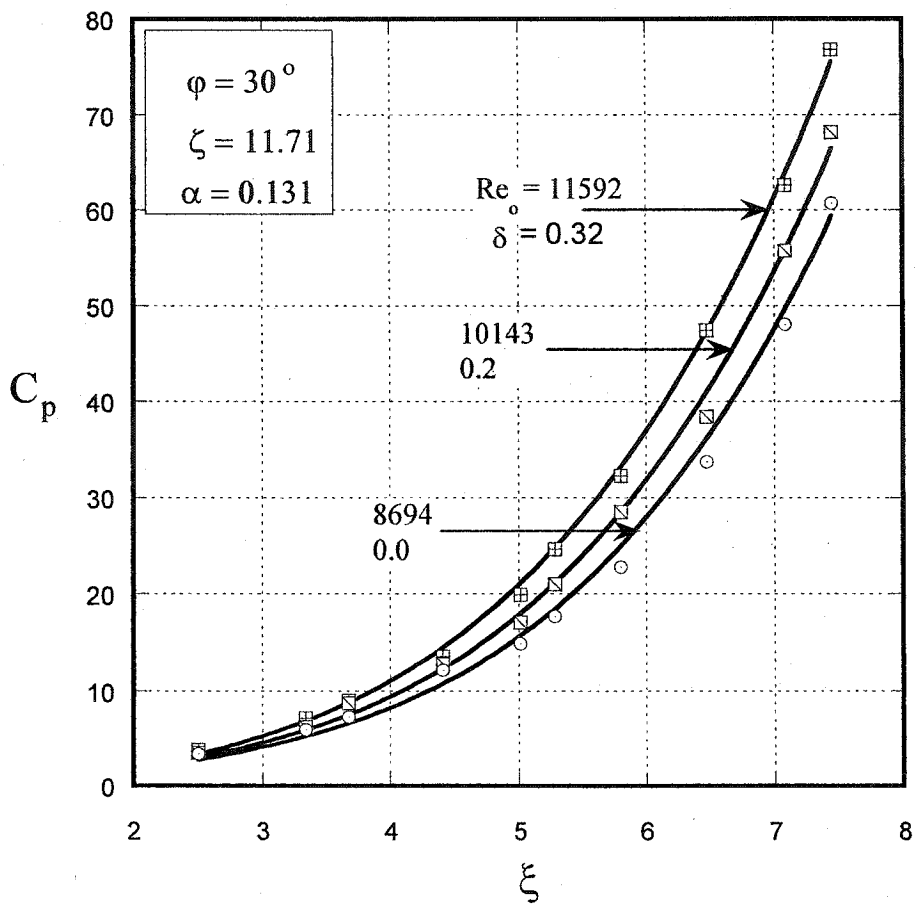

Figure (4-3-9): Pressure drop coefficient based on free vortex model for very long aspect ratio and an intermediate inlet angle ($\varphi = 30°$) chamber for different Reynolds numbers. The symbols refer to present experiment while the solid lines refer to present theory.

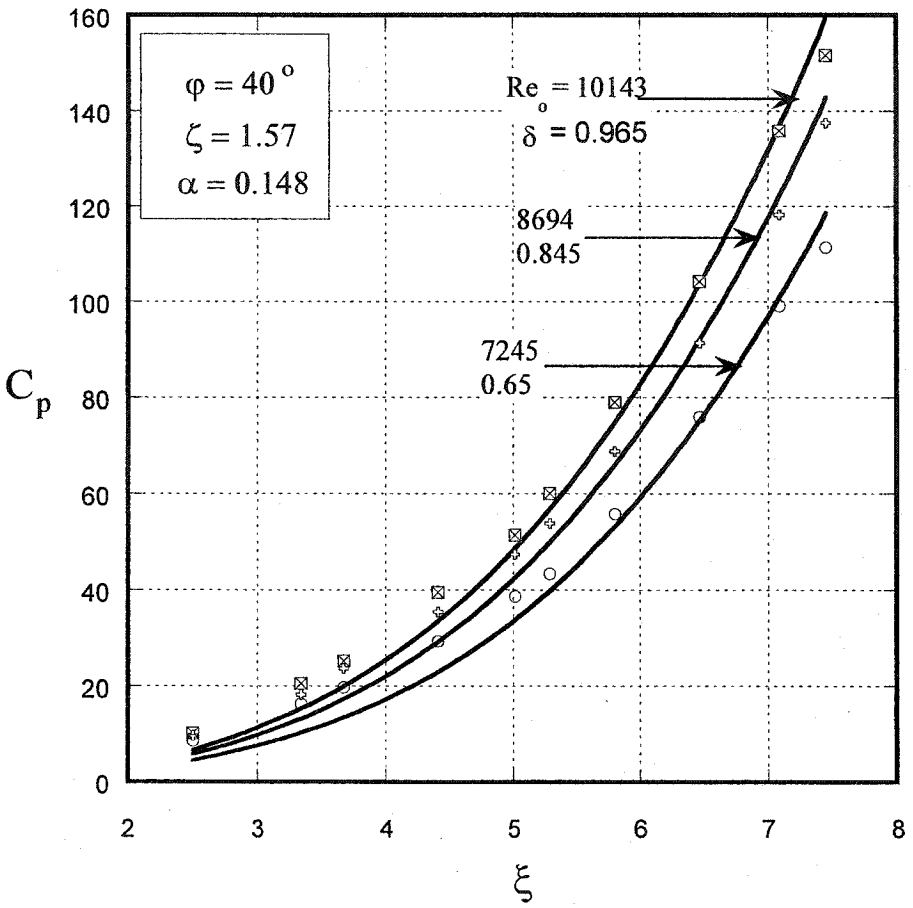

Figure (4-3-10): Pressure drop coefficient based on free vortex model in short aspect ratio chamber for an intermediate inlet angle ($\varphi = 40°$) for different Reynolds numbers. The symbols refer to present experiment while the solid lines refer to present theory.

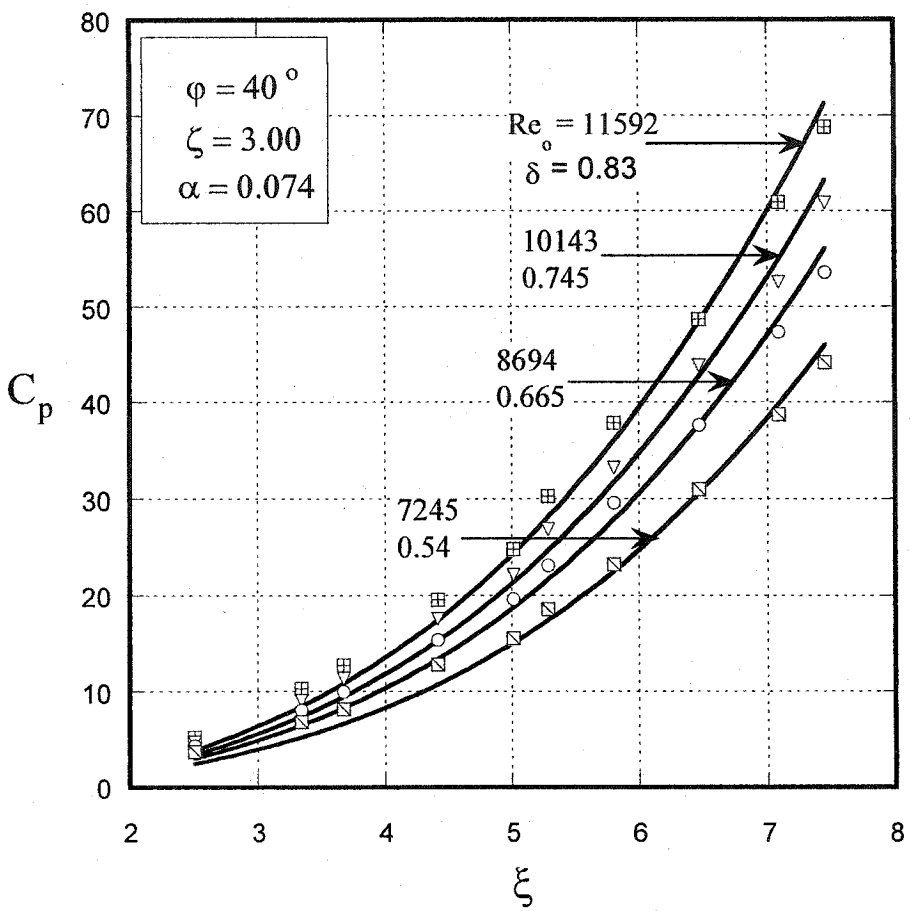

Figure (4-3-11): Pressure drop coefficient based on free vortex model in an intermediate aspect ratio chamber for an intermediate inlet angle ($\varphi = 40°$) for different Reynolds numbers. The symbols refer to present experiment while the solid lines refer to present theory.

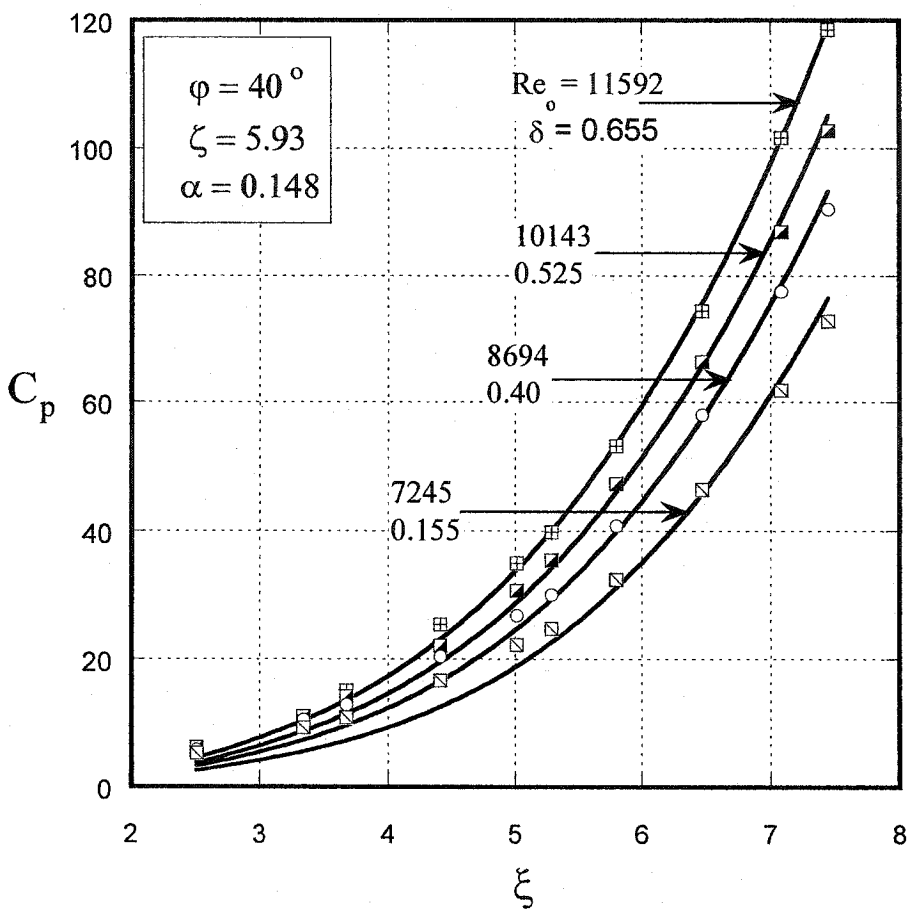

Figure (4-3-12): Pressure drop coefficient based on free vortex model in an intermediate aspect ratio and inlet angle ($\varphi = 40°$) chamber for different Reynolds numbers. The symbols refer to present experiment while the solid lines refer to present theory.

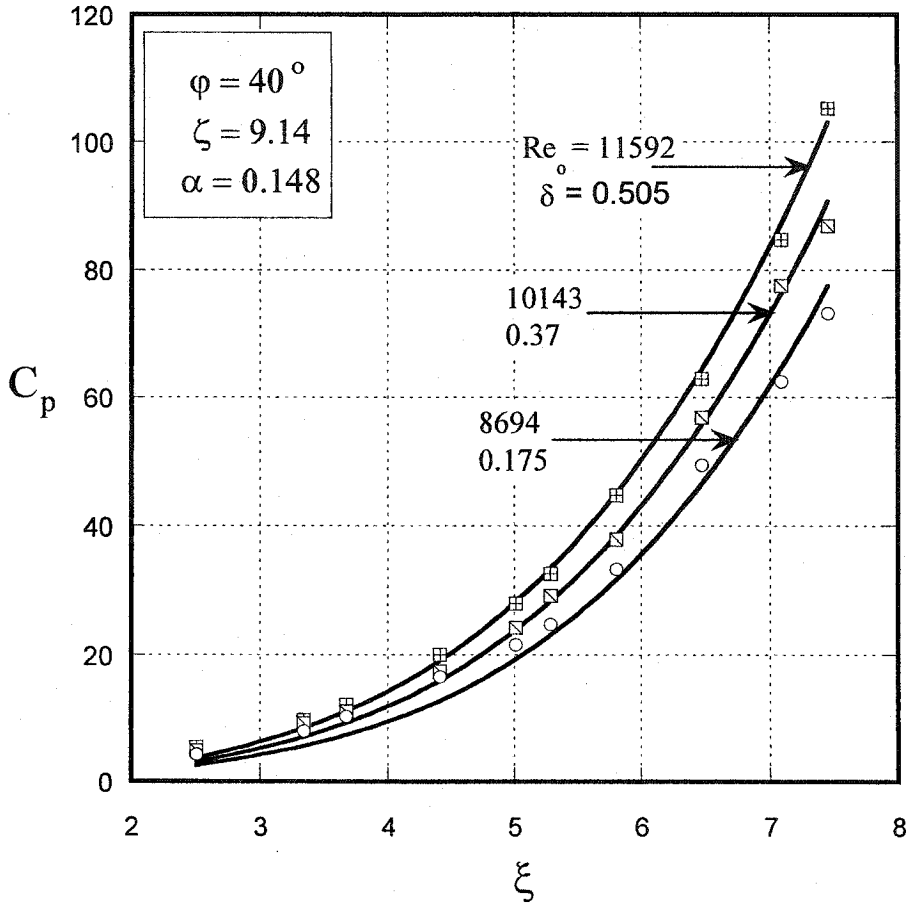

Figure (4-3-13): Pressure drop coefficient based on free vortex model for long aspect ratio and an intermediate inlet angle (φ=40°) chamber for different Reynolds numbers. The symbols refer to present experiment while the solid lines refer to present theory.

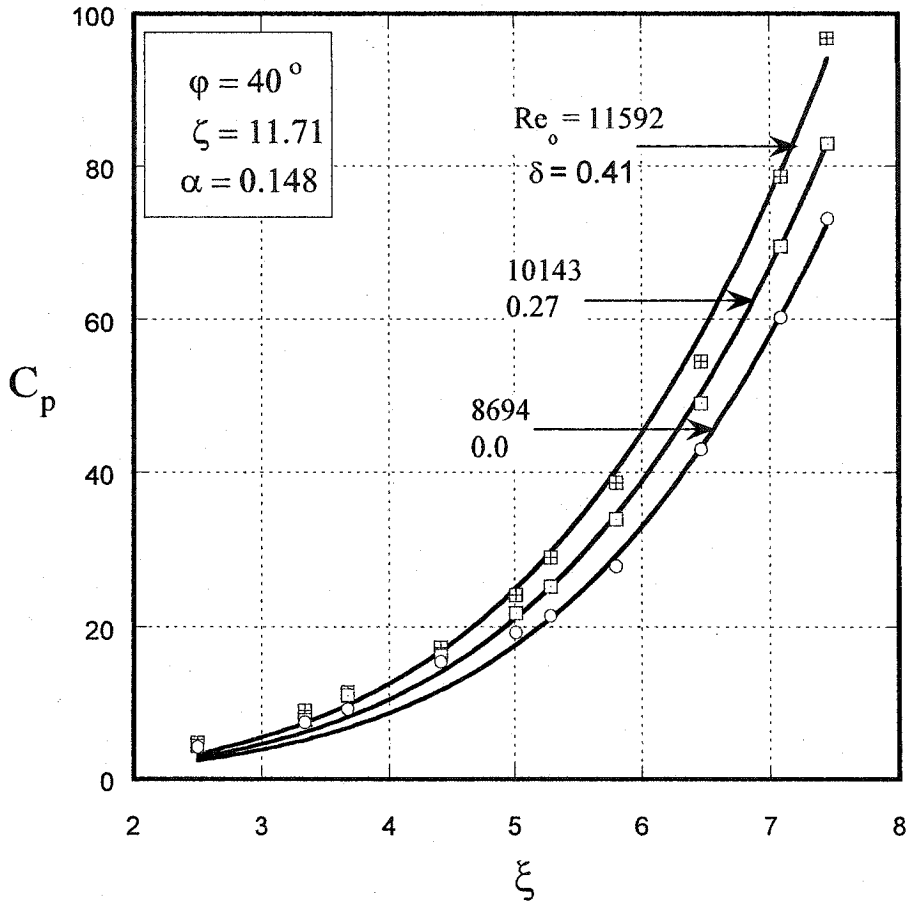

Figure (4-3-14): Pressure drop coefficient based on free vortex model for very long aspect ratio and an intermediate inlet angle ($\varphi = 40^\circ$) chamber for different Reynolds numbers. The symbols refer to present experiment while the solid lines refer to present theory.

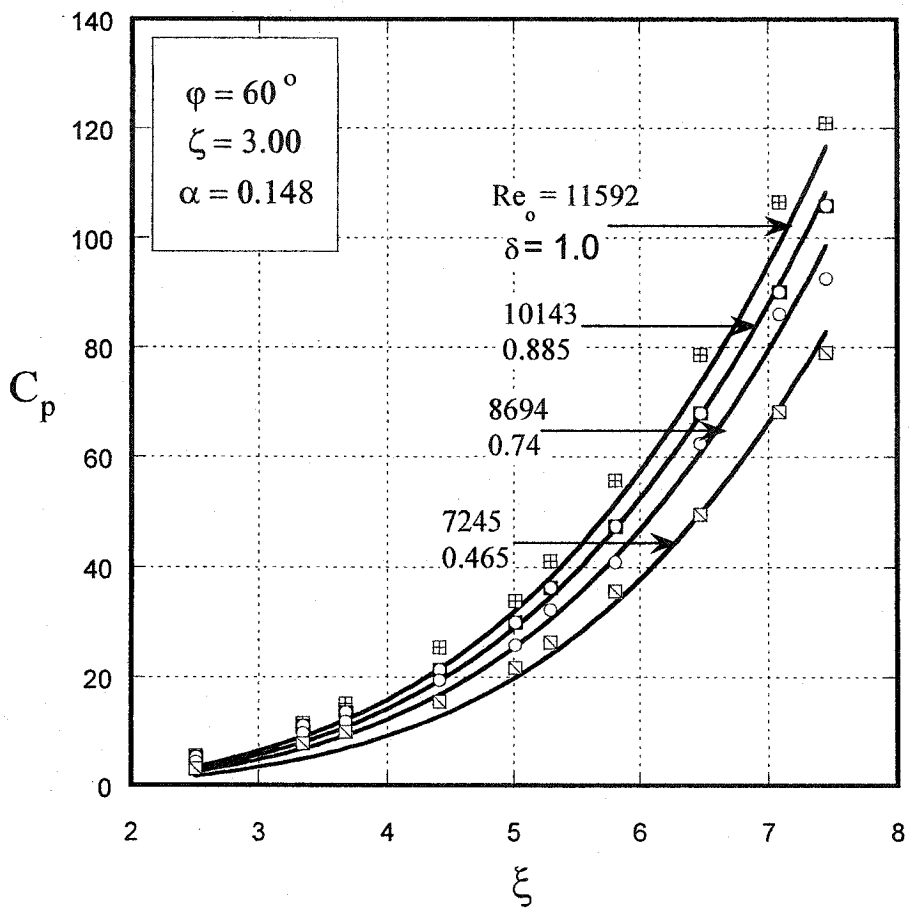

Figure (4-3-15): Pressure drop coefficient based on free vortex model in an intermediate aspect ratio chamber for large inlet angle (φ=60°) for different Reynolds numbers. The symbols refer to present experiment while the solid lines refer to present theory.

Chapter 5: Parametric Study

The parametric study will be used to explore the effects of aspect ratio, area ratio, and inlet angle on the pressure drop, core size, and friction losses. In addition to the Reynolds number and the swirl number, the conditions at the inlet and exit of a chamber play an essential role. The n=2 reverse vortex model will be used in to examine these effects.

5-1: Effect of Aspect Ratio on the Pressure Drop

The pressure coefficient for various aspect ratios (ζ) for a chamber with configuration $\varphi=30^o, \alpha=0.131$, is given in figure (5-1-1). The analysis suggests that δ becomes smaller as ζ increases producing a weaker vortex, lowering the tangential velocity, and therefore a smaller pressure drop. If P_a remains constant it means that P_{in} must be decreasing. At first the last appears to be counterintuitive since one expects the pressure drop to increase as the length is increased. However, here in addition to the r-z flow must also account for the centrifugal force, which influences the flow considerably. In addition, the contributions of axial inertial term (A_{axial}), swirl term (S_{swirl}), and the friction term ($F_{friction}$) on the pressure drop are given in figure (5-1-2) for two configurations $\zeta=3.0, \varphi=30^o, \alpha=0.131$ and $\zeta=11.71, \varphi=30^o, \alpha=0.131$. It is clear that A_{axial} and S_{swirl} for aspect ratio 3.00 are higher than aspect ratio 11.71 while $F_{friction}$ is less, the result is more pressure drop for shorter chamber. If one compares the

vortex chamber pressure drop with the pipe flow where most of pressure drop occurs mainly due to friction term, the axial inertial and swirl terms must be neglected and the result is increasing the pressure drop as the aspect ratio increases.

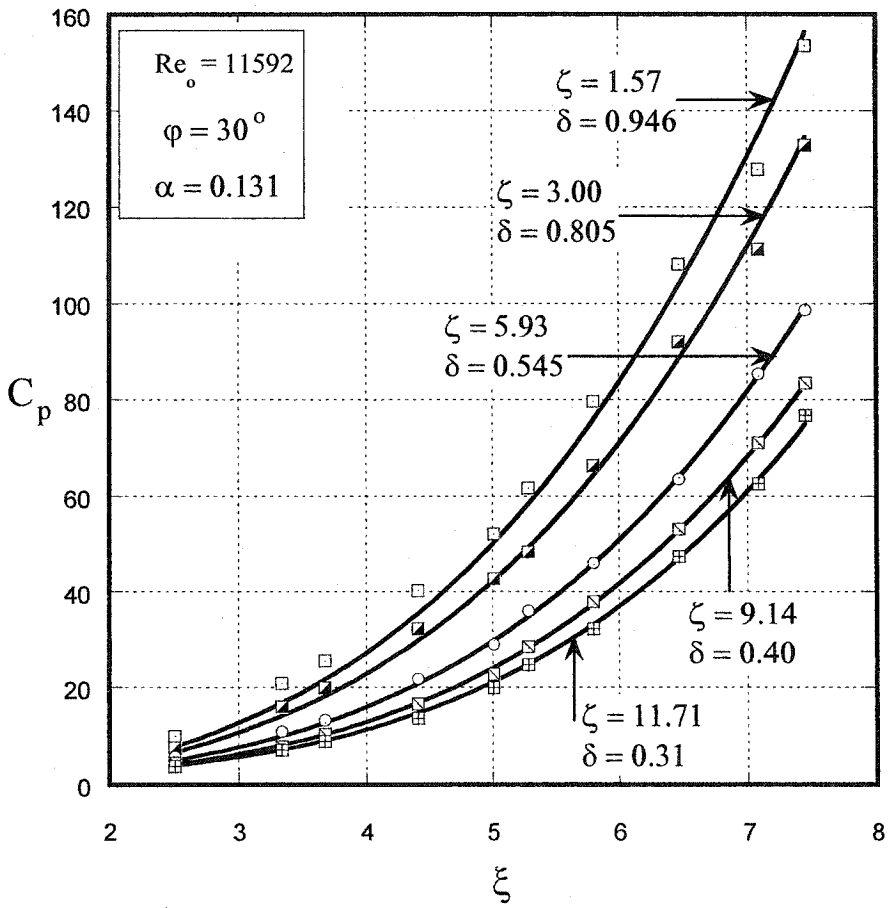

Figure (5-1-1): Pressure coefficient in an intermediate inlet angle for different aspect ratios. The symbols refer to present experiment while the solid lines refer to present theory.

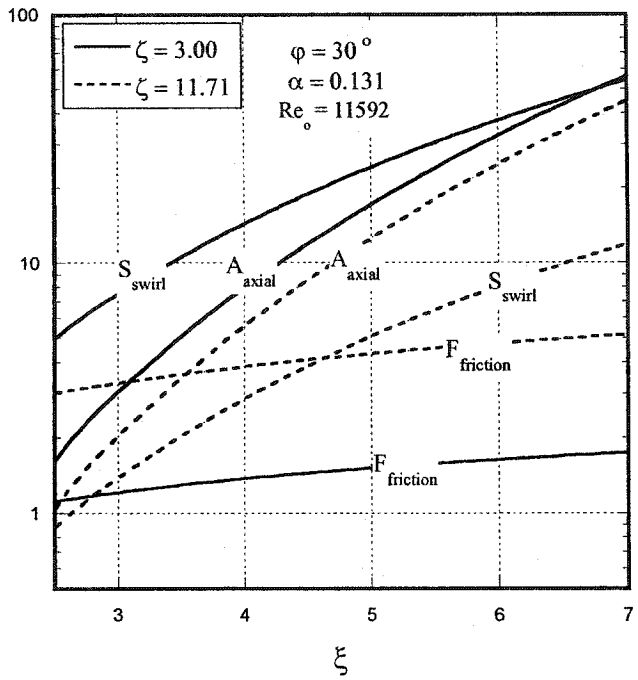

Figure (5-1-2): Variation of various flow terms for different aspect ratios

Figure (5-1-3) shows the core size variations for two aspect ratios (ζ =3.00, and 9.14) for configuration ($\varphi = 30^o, \alpha = 0.131$). Theory here suggests that at a given diameter ratio, inlet angle, area ratio and Reynolds number, the core size contracts as the aspect ratio increases.

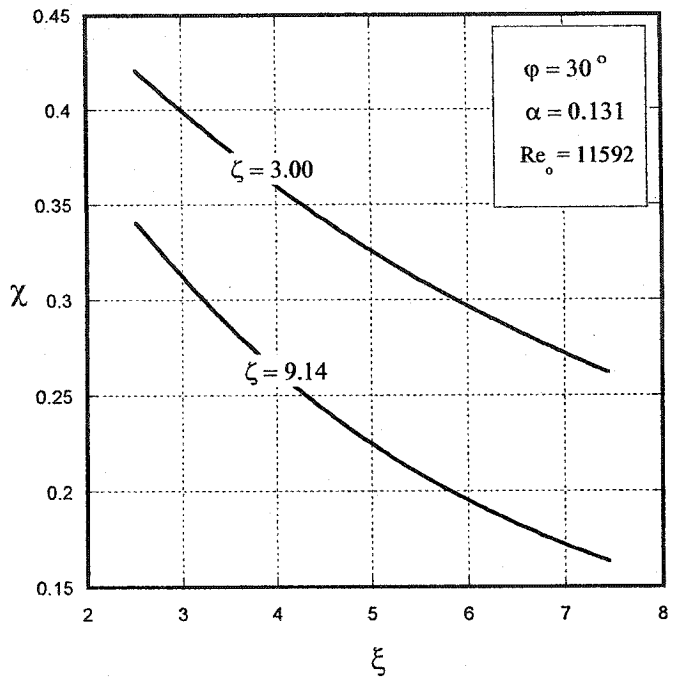

Figure (5-1-3): Core size vs the diameter ratio at two aspect ratios.

It is also interesting to see how the friction losses ($F_{friction}$) varies with aspect ratio. Figure (5-1-4) shows the theortical results of the friction losses for configuration ($\varphi = 30^o, \alpha = 0.131, R_{eo} = 11592$). The friction increases as the aspect ratio increases, and this is expected because the wall friction leads to a damping of the tangential velocity.

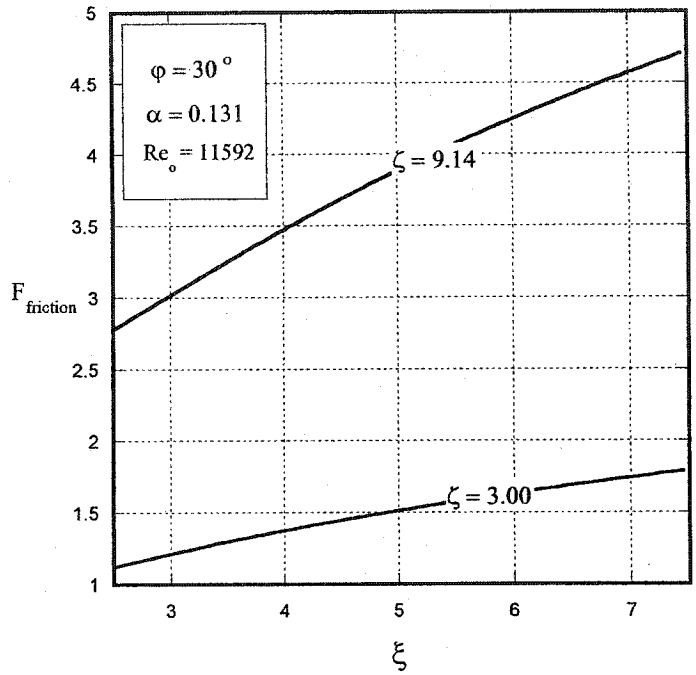

Figure (5-1-4): Friction loss vs the diameter ratio for different aspect Ratios.

5-2: Effect of Area Ratio on the Pressure Drop

The pressure coefficient (C_p) is also a function of the area ratio (α), therefore,the design of inlet ports are very crucial. In order to examine α, half of the inlets ports were blocked for configuration ($\varphi = 40^o, \alpha = 0.148, \zeta = 3.0$) and ΔP was measured. The results are shown in figure (5-2-1). For the smaller α the pressure coefficient (C_p) is seen to drop, but the actual pressure difference (ΔP) increases for increasing diameter ratio.

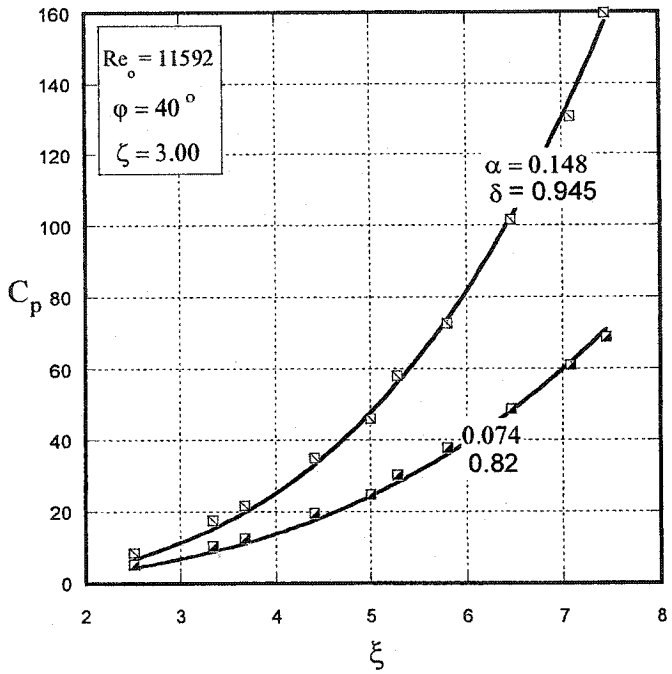

Figure (5-2-1): Pressure coefficient for different inlet area ratios. The symbols refer to present experiment while the solid lines refer to present theory.

For the case where the area ratio (α) is increased, the total inlet velocity (q_{in}) will be slowed down and hence the vortex strength will be weakened. That means the mass and energy transfer process will also be slowed down. By the principle of mass conservation, the same amount of mass has to be transferred in the same unit of time. Therefore, the core size will have to contract in size in order to maintain the same mass transfer to the atmosphere.

Figure (5-2-2) shows the core size variations for two area ratios (α=0.148, and 0.074) for configuration ($\varphi = 40^o, \zeta = 3.00$). Theory here suggests that at a given diameter

ratio, inlet angle, aspect ratio and Reynolds number, the core size contracts as the area ratio increases.

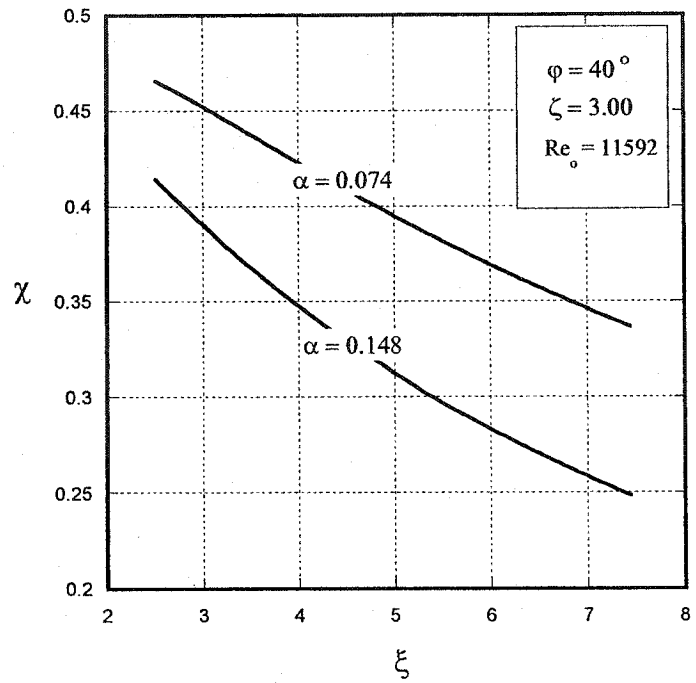

Figure (5-2-2): Core size vs the diameter ratio at two area ratios.

Figure (5-2-3) shows how the friction losses ($F_{friction}$) varies with the area ratio. The theortical results of the friction losses for configuration ($\varphi = 40^o, \zeta = 3.00, R_{eo} = 11592$) for two area ratios ($\alpha = 0.148$ and $\alpha = 0.074$) suggest that the friction increases as the area ratio decreases.

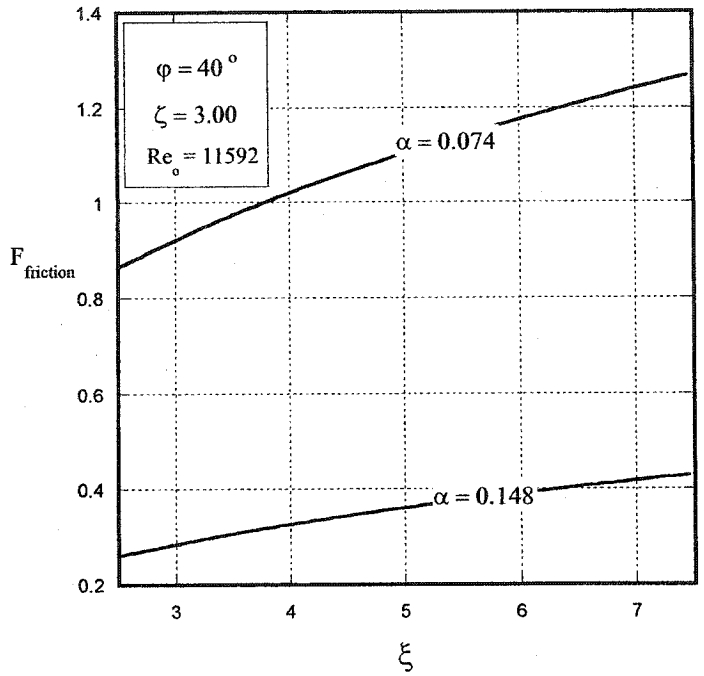

Figure (5-2-3): Friction loss vs the diameter ratio for different area ratios.

5-3: Effect of Inlet Angle on the Pressure Drop

All the vortex chamber configurations used up to this point have different α's and therefore it is unsuitable to discuss the influence of the inlet angle on the flow development because two variables will be changing at the same time. However, the swirler with $\varphi = 60^o$ has exactly the same α value with that of 40^o. The results of the study are shown in figure (5-3-1). It is expected that a stronger vortex is produced for smaller inlet angle and thus the pressure drop for small φ's must be large. The latter is amply evident from the same figure.

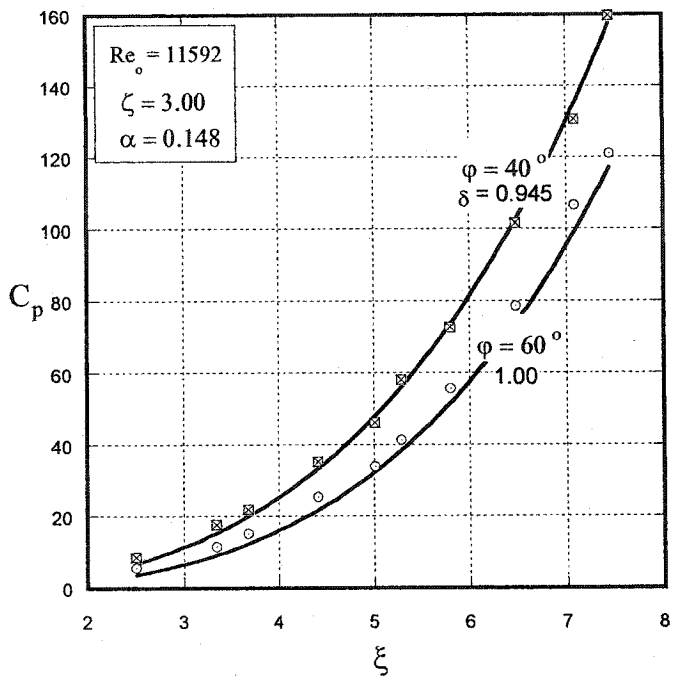

Figure (5-3-1): Pressure coefficient in an intermediate aspect ratio chamber for different inlet angles. The symbols refer to present experiment while the solid lines refer to present theory.

If the inlet angle (φ) is increased, this means to decrease the inlet swirling strength (Γ) of the vortex. Where the Γ is decreased, the tangential velocity component will be decreases inside the chamber. That means there is a shift of momentum to the axial or radial direction since the total inlet velocity (q_{in}) remains the same. However, the shift of momentum has mainly happened in the radial direction because the total inlet velocity (q_{in}) consists of the tangential and radial components only. This leads to a decrease of the core size.

Figure (5-3-2) shows the core size variations for two inlet angles ($\varphi = 40^o$ and 60^o), for configuration ($\alpha = 0.148, \zeta = 3.00$). Theory here suggests that at a given diameter ratio, area ratio, aspect ratio and Reynolds number, the core size expands as the inlet angle decreases.

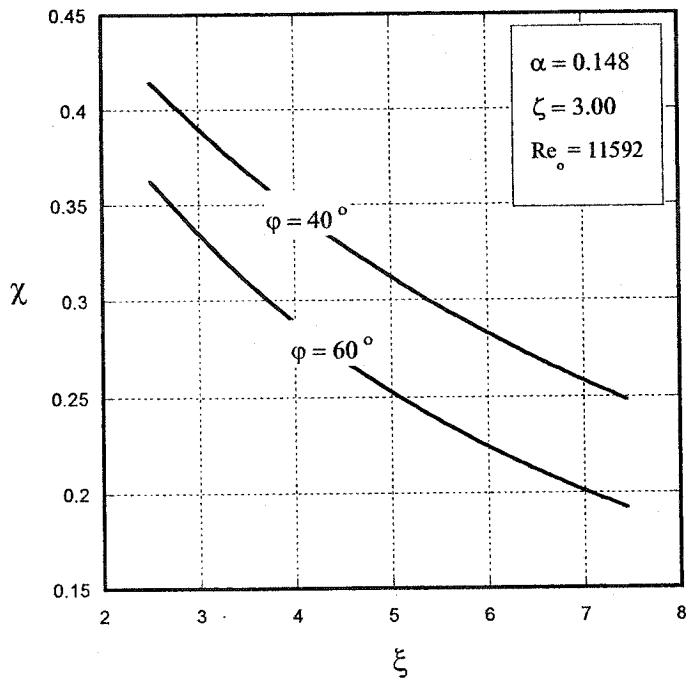

Figure (5-3-2): Core size vs the diameter ratio at two inlet angles.

Figure (5-3-3) shows how the friction losses ($F_{friction}$) varies with the inlet angle. The theortical results of the friction losses for configuration ($\alpha = 0.148, \zeta = 3.00, R_{eo} = 8694$) for two inlet angles ($\varphi = 40^o$ and $\varphi = 60^o$) suggest that the friction increases as the inlet angle decreases.

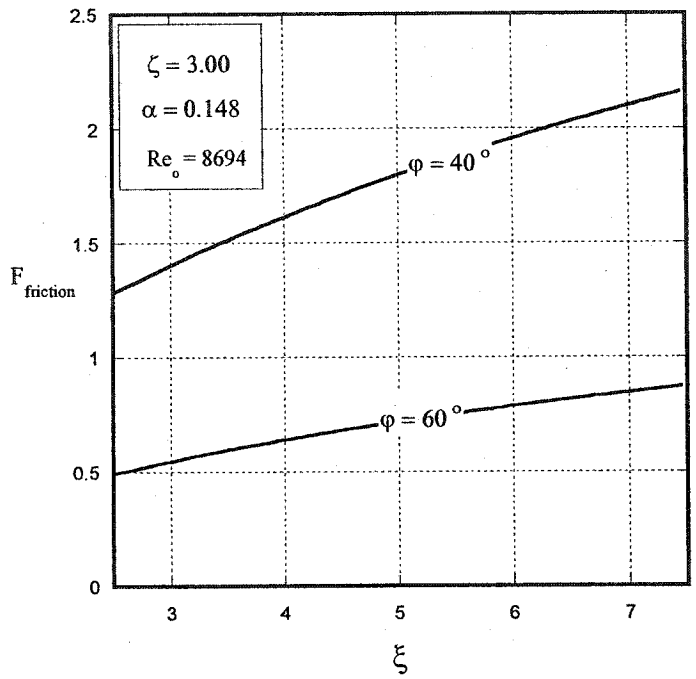

Figure (5-3-3): Friction loss vs the diameter ratio for different inlet angles.

Chapter 6: Comparison of Vortex Models

6-1: Swirl, Axial Inertial and Friction Terms

Comparison of three models: n=2 reverse flow, n=2 non-reverse flow and free vortex models are shown in figures (6-1-1) to (6-1-3) for two configurations ($\varphi=20^{o},\zeta=3.0,\alpha=0.05,R_{eo}=11592$) and ($\varphi=30^{o},\zeta=3.0,\alpha=0.131,R_{eo}=11592$). From the last two figures at constant Reynolds number, the axial inertial term for n=2 non-reverse is the highest, while for n=2 reverse is the lowest. The swirl term for n=2 reverse is the highest, while for n=2 non-reverse is the lowest. The friction term for n=2 reverse is the highest, then free vortex, then n=2 non-reverse model. From figure (6-1-2) for configuration ($\varphi=30^{o},\zeta=3.0,\alpha=0.131$), the swirl and axial terms are approximately equal for n=2 reverse and free vortex models.

By taking the n=2 reverse model as an example and fixing the geometry, the effects of Reynolds number on the pressure drop terms can be observed. Figure (6-1-3) for configuration ($\varphi=30^{o},\zeta=3.0,\alpha=0.13130$) at two Reynolds numbers (11592 and 7245) shows that the axial and the swirl terms for $R_{eo}=11592$ are higher than at $R_{eo}=7245$, but more energy loss is as expected at lower Reynolds number.

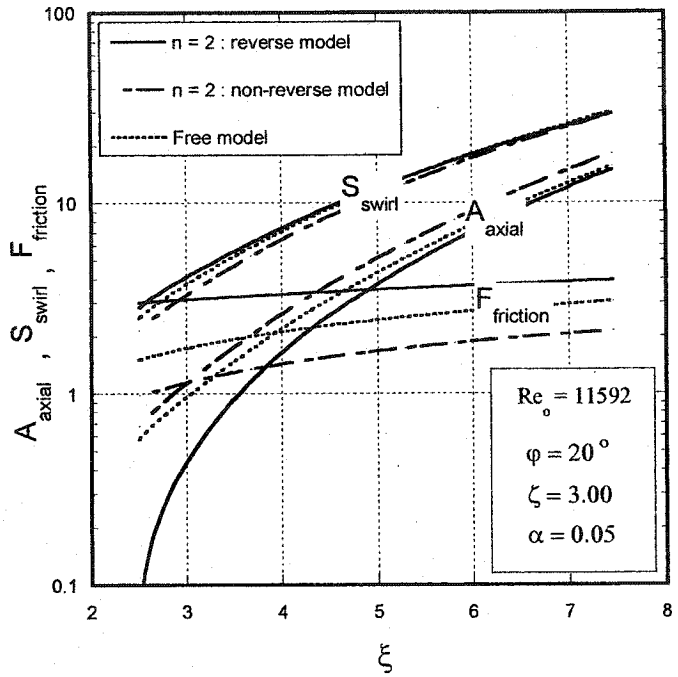

Figure (6-1-1): Axial, swirl, and friction terms for an intermediate aspect ratio and a small inlet angle.

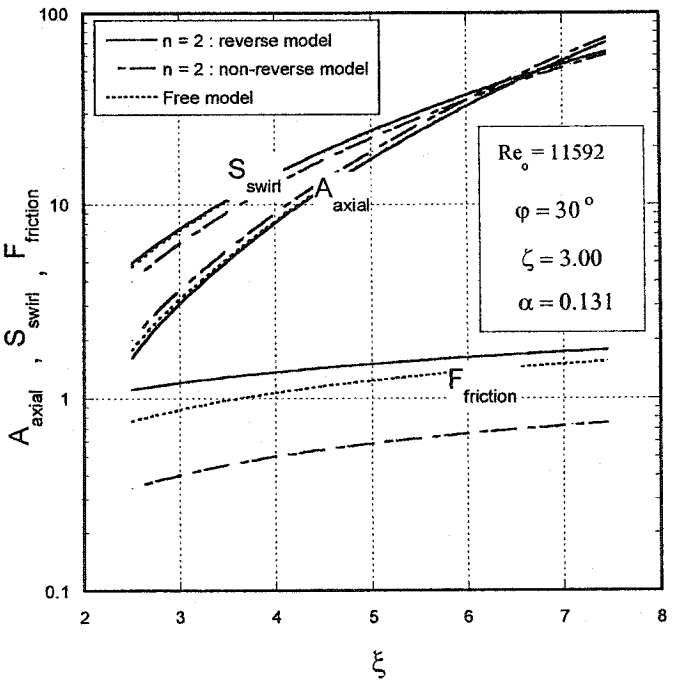

Figure (6-1-2): Axial, Swirl, and Friction terms for an intermediate aspect ratio and inlet angle.

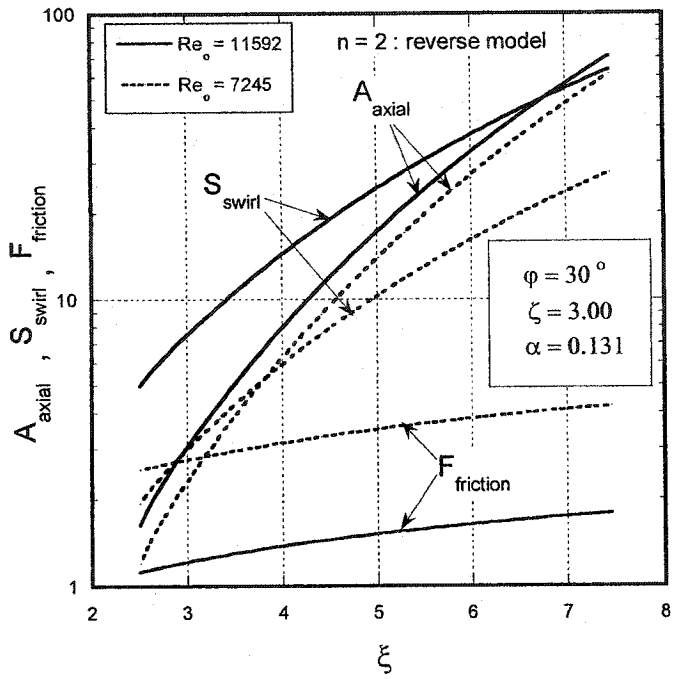

Figure (6-1-3): Axial, Swirl, and Friction terms for an intermediate aspect ratio and inlet angle for two Reynolds number.

6-2: Core Size Comparison

The LDA experiments of Yan et al [60] have shown that the core-size inside the chamber stays nearly constant along the height. Assuming that the core at the exit plane is the same as that inside the chamber, the present theories are employed to predict the core-size and compare it with the observed values. The results are shown in figure (6-2-1) where an acceptable correlation between the experiment and present theories is apparent. In this case the experimental χ_{co} ($\chi_c R_e / R_o$) values have been ascertained by fitting the n = 2 vortex model to the LDA velocity data using the least squares method with one of the unknown variables being the core-size while the other is the vortex strength.

It is clear from figure (6-2-1) that the free and n=2 non-reverse models have the same core size values and agree with the Yan et al [60] experiments till diameter ratio (ξ) equal to 3 , while the n=2 reverse model has lowest core size and agree with experiment (Ref. 60) for ξ more than 3. In addition, the χ_o values for the free and n=2 non-reverse models are approximately equal and higher than the n=2 reverse model.

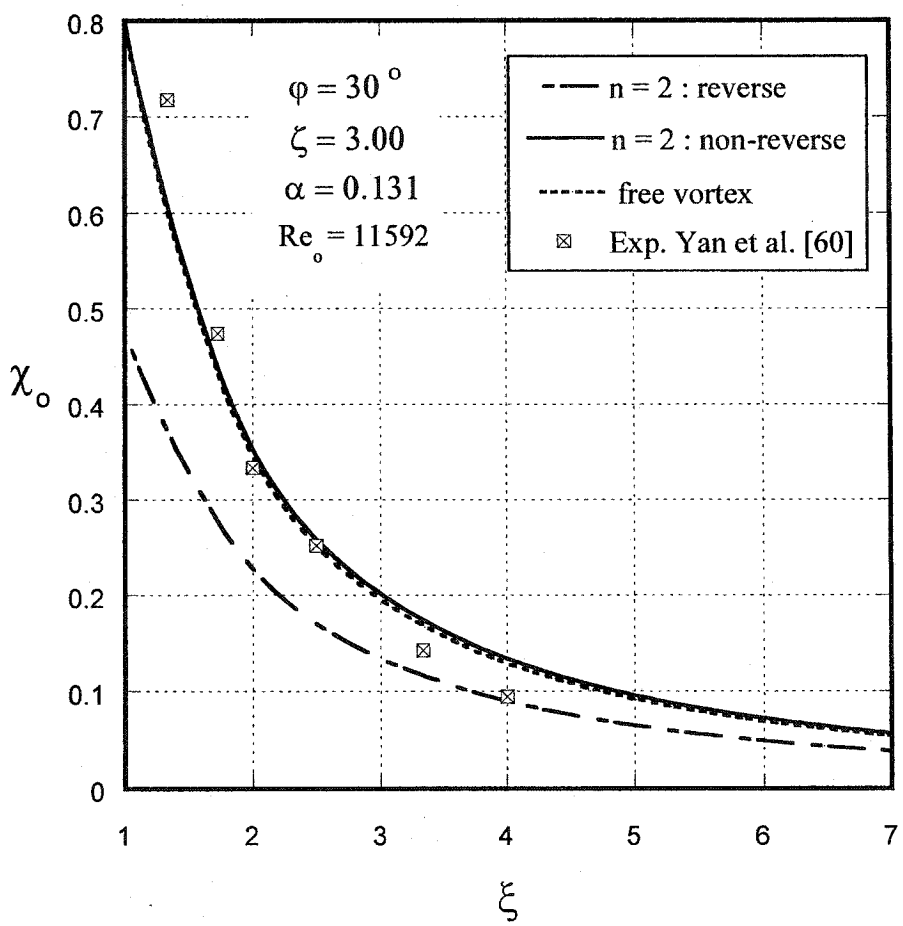

Figure (6-2-1): Core size variations.

6-3: Swirl Velocities Profiles

In addition to the capability of the previous three models to predict the pressure drop coefficient (C_p), vortex core (χ), and the vortex circulation (Γ), swirl velocities profiles can be obtained. In the case where the tangential velocity is based on n=2 vortex model then,

$$V_{\varphi out} = \frac{\delta Q_{in} \cos(\varphi)}{A_{in}} \frac{\bar{r}}{\left[\left\{\frac{\chi}{\xi}\right\}^4 + \bar{r}^4\right]^{1/2}} \tag{6-1}$$

where

$$\bar{r} = \frac{r}{R_o}$$

The last equation is valid for reverse and non-reverse axial flow with different values of χ and δ .

In the case of free vortex swirl velocity:

$$V_{\varphi out} = \frac{\delta Q_{in} \cos(\varphi)}{A_{in}} \frac{1}{\bar{r}} \tag{6-2}$$

Figures (6-3-1) a, b, c, and d show the swirl velocities profiles for the configuration ($\varphi=30^{\circ}, \zeta=3.0, \alpha=0.131$) at Reynolds number ($R_{eo}=11592$) and the results are compared with available experiments data (LDA) from Yan et al [60] at different diameter ratios (ξ). The free vortex model shows a good agreement with the experiments in the free vortex region. It is obvious from figure 6-3-1a that n=2 model for reverse flow can capture the experimental points at $\xi = 4.00$, while n = 2 model for non-reverse flow can capture the points at $\xi =$ 3.33, 2.5, and 2, see figures (6-3-1) b to d . This is may be due to how the vortex core size

$$\chi_o = \frac{\chi}{\xi}$$

behaves, see figure (6-2-1). . In the last figure, the peak tangential velocity decreases with the diameter ratio, where the location where the tangential velocity is maximum moves towards the vortex chamber center. Free vortex and n=2 non-reverse flow models agree with the core size (χ_o) experiment of Yan et al [60] for $\xi<4$, while n=2 reverse flow model agree for $\xi \geq 4$. Generally the reverse model is applicable for large values of ξ where strong vortex exists.

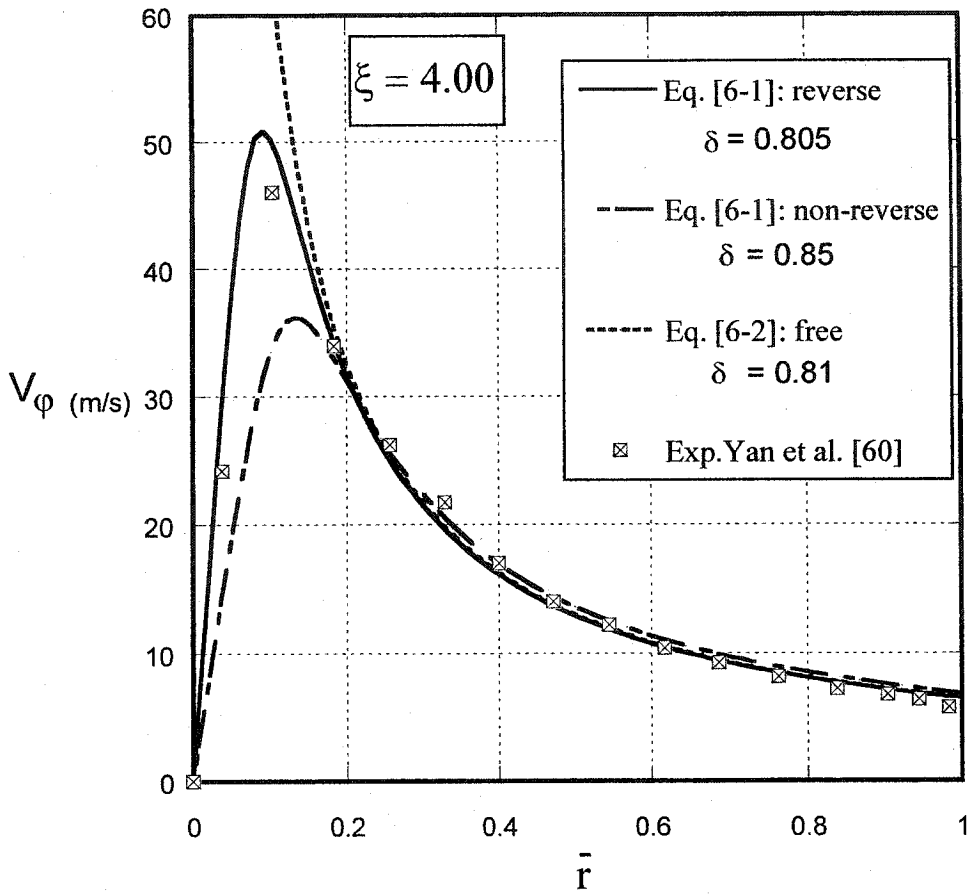
60
50
40
30
20
10
0
V_φ (m/s)
$\xi = 4.00$
Eq. [6-1]: reverse
$\delta = 0.805$
Eq. [6-1]: non-reverse
$\delta = 0.85$
Eq. [6-2]: free
$\delta = 0.81$
Exp.Yan et al. [60]
0
0.2
0.4
0.6
0.8
1
$\bar{r}$

Figure (6-3-1a)

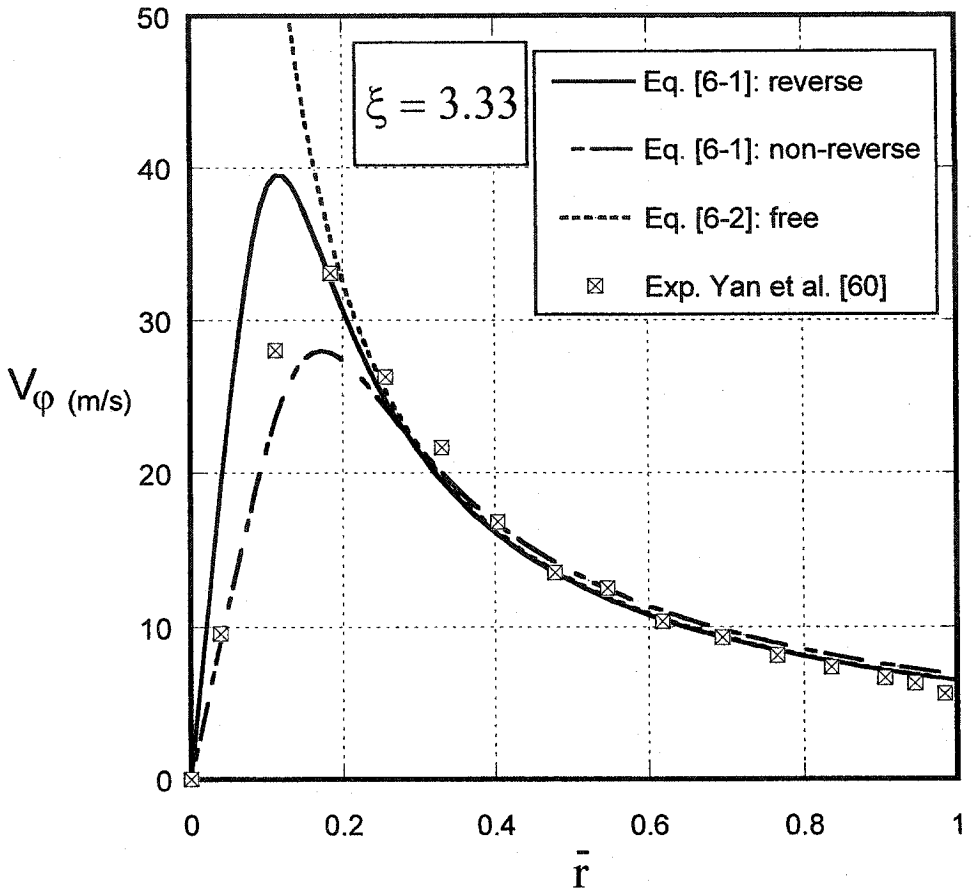
50
40
30
20
10
0
0
0.2
0.4
0.6
0.8
1
V_φ (m/s)
$\bar{r}$
$\xi = 3.33$
Eq. [6-1]: reverse
Eq. [6-1]: non-reverse
Eq. [6-2]: free
Exp. Yan et al. [60]

Figure (6-3-1b)

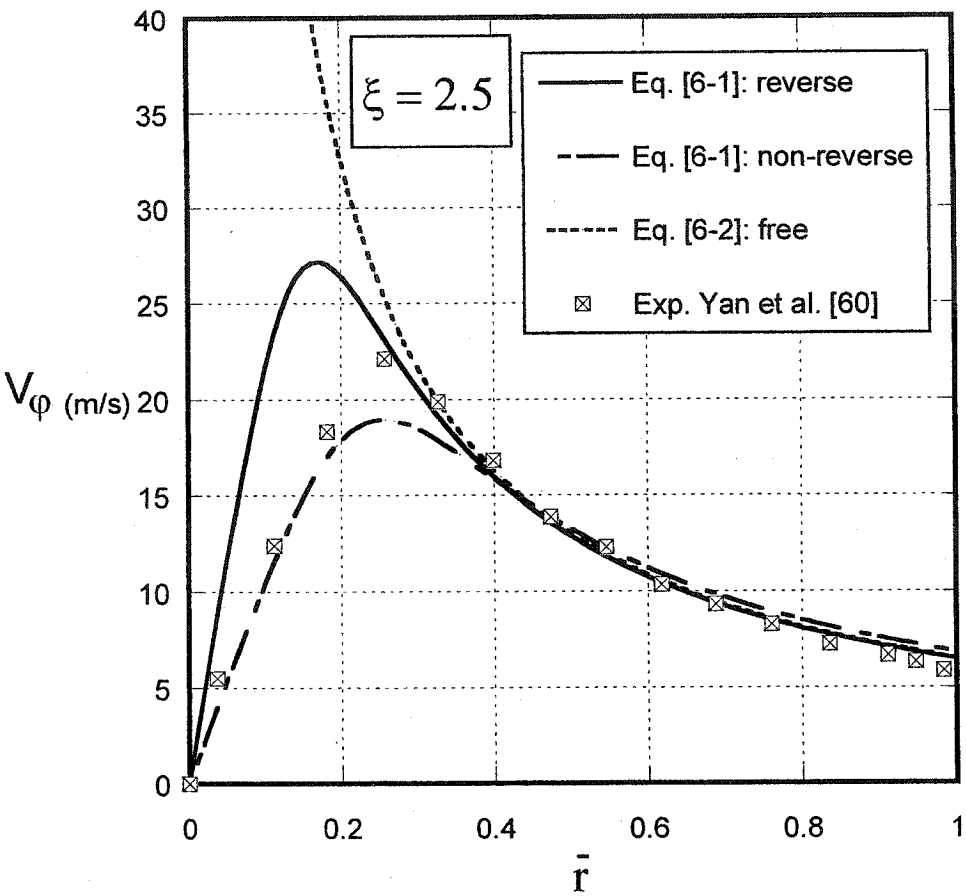
ξ = 2.5
Eq. [6-1]: reverse
Eq. [6-1]: non-reverse
Eq. [6-2]: free
Exp. Yan et al. [60]
Vφ (m/s)
r̄
0
5
10
15
20
25
30
35
40
0
0.2
0.4
0.6
0.8
1

Figure (6-3-1c)

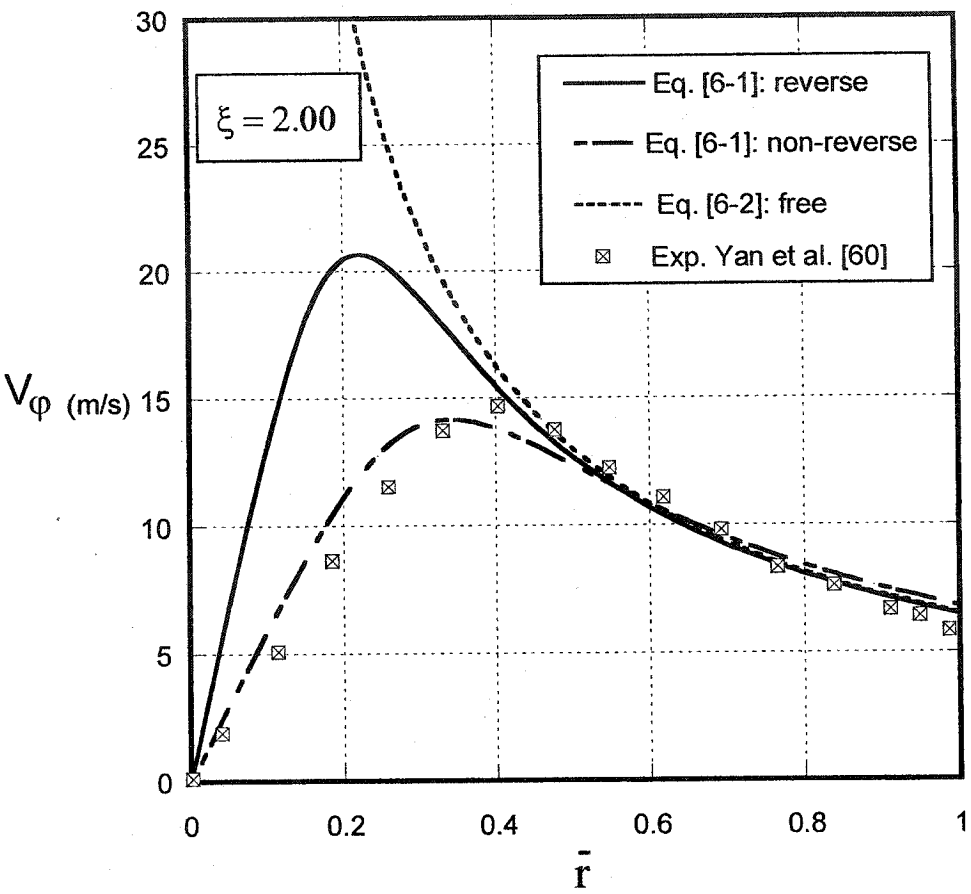

Figure (6-3-1d)

Figure (6-3-1): Tangential velocities profiles at different diameter ratios.

6-4: Radial Pressure Profiles

The following analysis illustrates that an approximate solution of the pressure distribution profile Π can be obtained if the tangential velocity profile is a known function. Two tangential velocity profiles: n=2 model in case of reverse and non-reverse flow, and free vortex velocity profile will be used to formulate the analysis and the derived radial pressure (Π) will be compared with available experimental data from Lam [41] and Alekseenko [42]. In the case of strong vortex, the tangential velocity is dominant within the flow field, the r-momentum equation gives

$$\frac{\partial p}{\partial r}=\rho\frac{V_{\varphi 2}^{2}}{r} \tag{6-3}$$

Substitution of equation (3-4) into equation (6-3), the radial pressure profile inside a vortex chamber based on n=2 vortex model is given by

$$\Pi(\bar{r})=\delta^{2}\cos^{2}(\varphi)\left(\frac{\xi}{\chi}\right)^{2}\left[\arctan\left(\left\{\frac{\xi}{\chi}\right\}^{2}\bar{r}^{2}\right)-\arctan\left(\left\{\frac{\xi}{\chi}\right\}^{2}\right)\right] \tag{6-4}$$

The above equation is valid for reverse and non-reverse flow, where the differences are in the values of the core size and the vortex decay factor.

Substituting equation (3-10) into equation (6-3), the radial pressure profile inside a vortex chamber based on free vortex model is given by

$$\Pi(\bar{r}) = \delta^2 \cos^2(\varphi)\left[1 - \frac{1}{\bar{r}^2}\right] \tag{6-5}$$

where

$$\Pi(\bar{r}) = \frac{2\left(p(\bar{r}) - p(\bar{r}=1)\right)}{\rho q_{in}^2}$$

Figure (6-4-1) shows the radial pressure coefficient (Π) with the experimental results (Ref.41) for the configuration ($\varphi = 40^o, \zeta = 3.00, \alpha = 0.148$) and Reynolds number $R_{eo} = 20288$. A good agreement for n=2 reverse model with the experiment is observed, while the others are not. This is expected because the vortex field is under strong swirling conditions especially at high Reynolds number.

In figure (6-4-2) the radial pressure for the configuration ($\varphi = 40^o, \zeta = 2.28, \alpha = 0.109$) is compared with experimental data obtained from Alekseenko [42]. The n=2 reverse model agrees well with the experiment. This is expected because the aspect and area ratios are small which leads to a strong vortex.

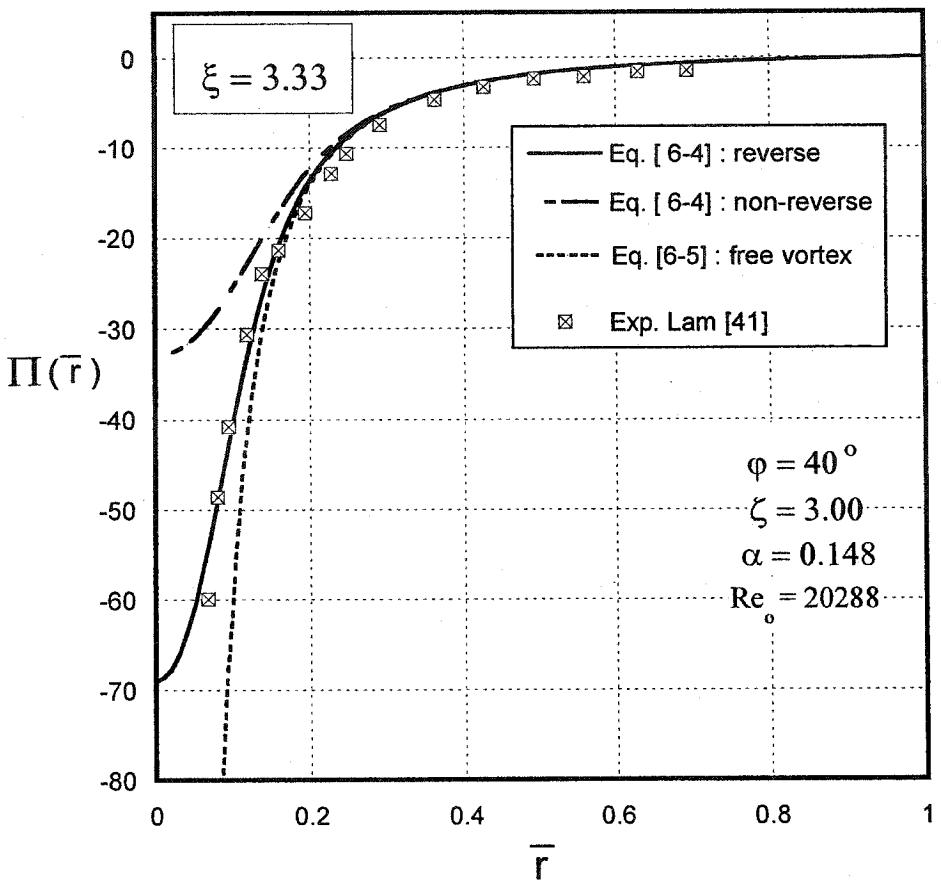

Figure (6-4-1): Radial pressure profile at a diameter ratio (ξ) equal to 3.33.

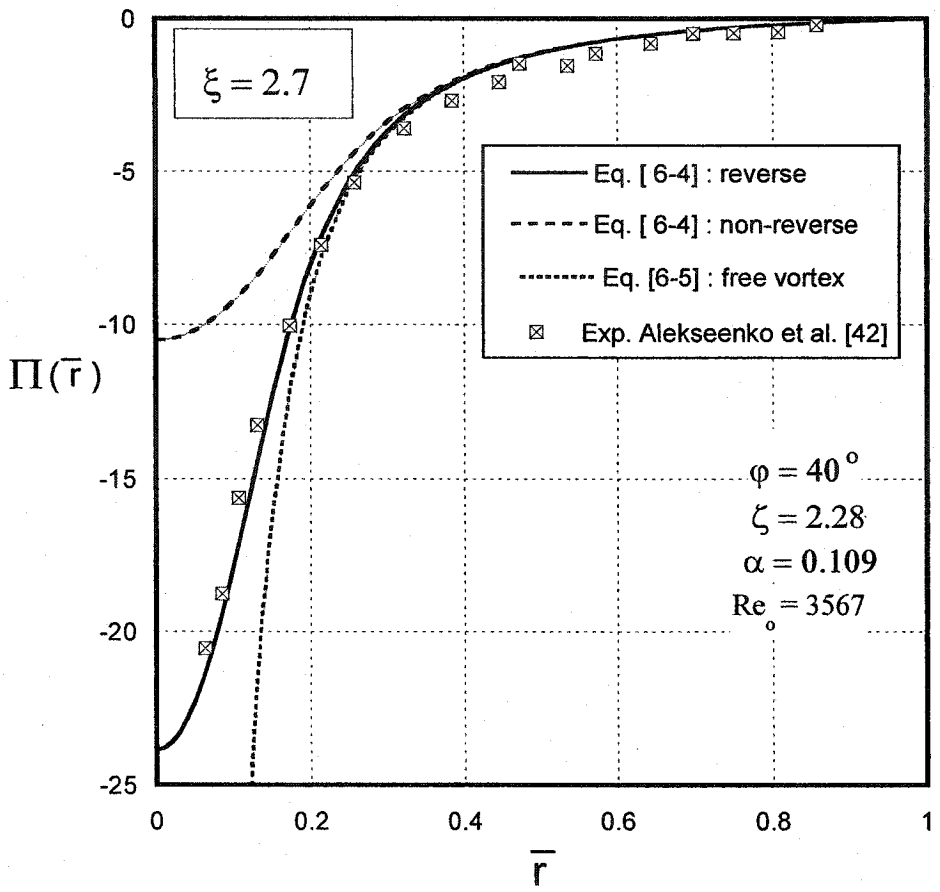

Figure (6-4-2): Radial pressure profile at a diameter ratio (ξ) equal to 2.7.

In the following analysis the pressure profile ($\Delta\overline{P}$) will be given as a difference between the radial pressure and ambient, the reason is to see when the reverse flow will occur. The present experiments reveal that the wall static pressure (p_{wall}) does not change sufficiently with chamber height, and the same conclusion was reached by Alekseenko [42], Vyas [32] and Lam [41]. The pressure distribution in the axial direction is almost negligible compared to the rapid radial variations. Therefore, the wall static pressure and inlet static pressure approximately equal

$$P_{wall} \cong P_{in}$$

From equations (3-5) and (6-4), the pressure profile ($\Delta\overline{P}$) inside the vortex chamber based on n=2 reverse model is given by

$$\begin{aligned}
\Delta\overline{P} \;=\; & \gamma_2 \delta^2 \cos^2(\varphi)\, \xi^2 \frac{Ln\left[\frac{1}{2}\left\{1+\frac{1}{\chi^4}\right\}\right]}{2(1-\chi^2)} + \gamma_2^3 \alpha^2 \xi^4 \frac{1}{(1-\chi^2)^2} \\
& - \left[\gamma_2 - 1\right]\delta^2 \cos^2(\varphi)\, \xi^2 \frac{Ln(2)}{2\chi^2} - \left[\gamma_2 - 1\right]^3 \alpha^2 \xi^4 \frac{1}{\chi^4} \\
& + \gamma_2 \cos^2(\varphi)\left[1-\delta^2\right] \frac{Ln\left[\frac{1}{2}\left\{1+\left(\frac{\xi}{\chi}\right)^4\right\}\right]}{2\left[1-\left(\frac{\chi}{\xi}\right)^2\right]} - 1 \\
& + \delta^2 \cos^2(\varphi)\left(\frac{\xi}{\chi}\right)^2 \left[\arctan\left(\left\{\frac{\xi}{\chi}\right\}^2 \bar{r}^2\right) - \arctan\left(\left\{\frac{\xi}{\chi}\right\}^2\right)\right]
\end{aligned} \tag{6-6}$$

From equations (4-1) and (6-4), the pressure profile ($\Delta\overline{P}$) inside the vortex chamber based on n=2 non-reverse model is given by

$$\Delta\overline{P} = \delta^2\cos^2(\varphi)\,\xi^2\frac{Ln\left[\frac{1}{2}\left\{1+\frac{1}{\chi^4}\right\}\right]}{2(1-\chi^2)} + \alpha^2\xi^4\frac{1}{(1-\chi^2)^2}$$

$$+\cos^2(\varphi)\,(1-\delta^2)\frac{Ln\left[\frac{1}{2}\left\{1+\left(\frac{\xi}{\chi}\right)^4\right\}\right]}{2\left[1-\left(\frac{\chi}{\xi}\right)^2\right]} - 1 \qquad (6\text{-}7)$$

$$+\delta^2\cos^2(\varphi)\left(\frac{\xi}{\chi}\right)^2\left[\arctan\left(\left\{\frac{\xi}{\chi}\right\}^2\bar{r}^2\right) - \arctan\left(\left\{\frac{\xi}{\chi}\right\}^2\right)\right]$$

where

$$\Delta\overline{P} = \frac{2\left(P(\bar{r}) - P_a\right)}{\rho q_{in}^2}$$

Figure (6-4-3) and (6-4-4) show the profiles of radial pressure ($\Delta\overline{P}$) distributions inside the vortex chamber based on the above theory for configuration ($\varphi=30^o$, $\alpha=0.131$, $\zeta=3.00$) and Reynolds number equal to 11592. Reverse flow appears in the central region and the magnitude of the reverse flow increases as the diameter ratio increases. It is clear that the pressure drops to a negative value as it approaches the core region, more drops occur for large contraction ratios due to strong vortex. As shown in figure (6-4-5),

the pressure drop is deeper for the n=2 reverse model, when compared to the n=2 non-reverse model.

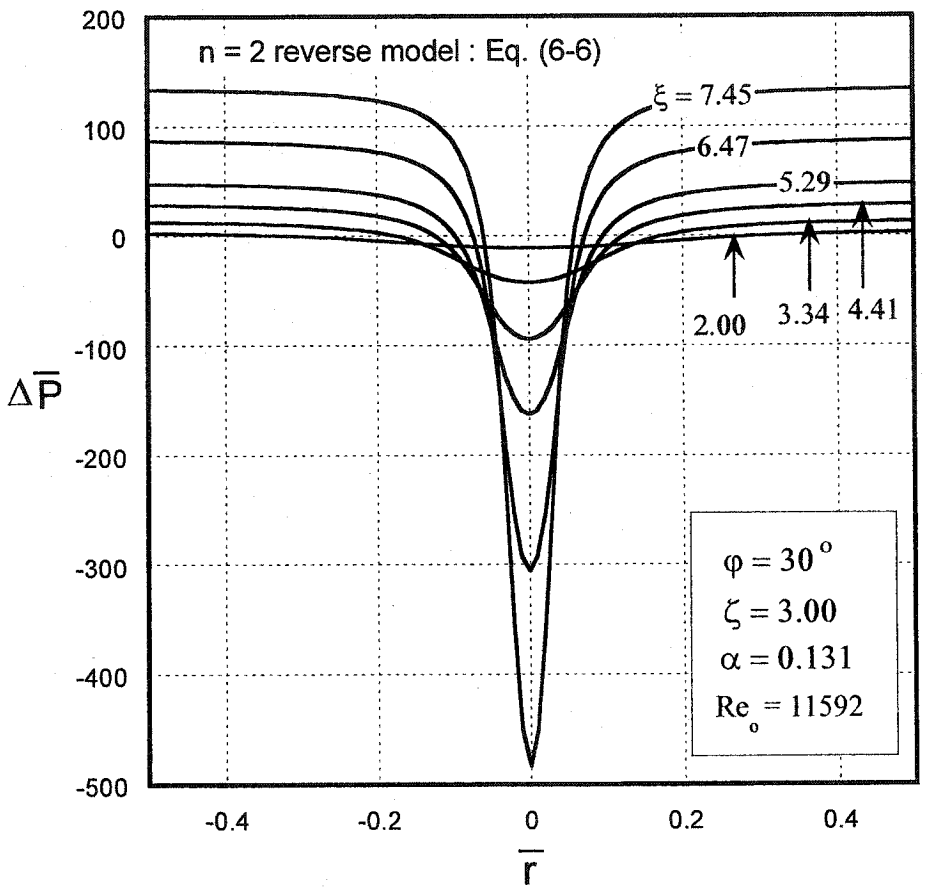

Figure (6-4-3): Radial pressure profile based on n=2 reverse vortex model.

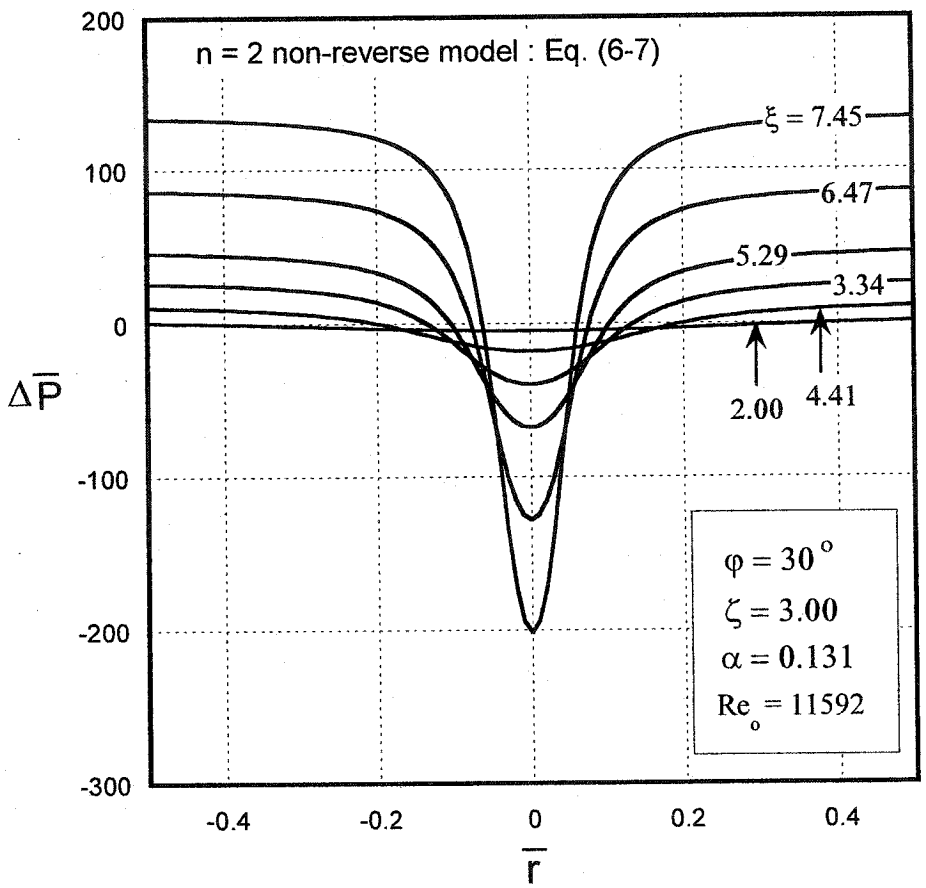

Figure (6-4-4): Radial pressure profile based on n=2 non-reverse vortex model.

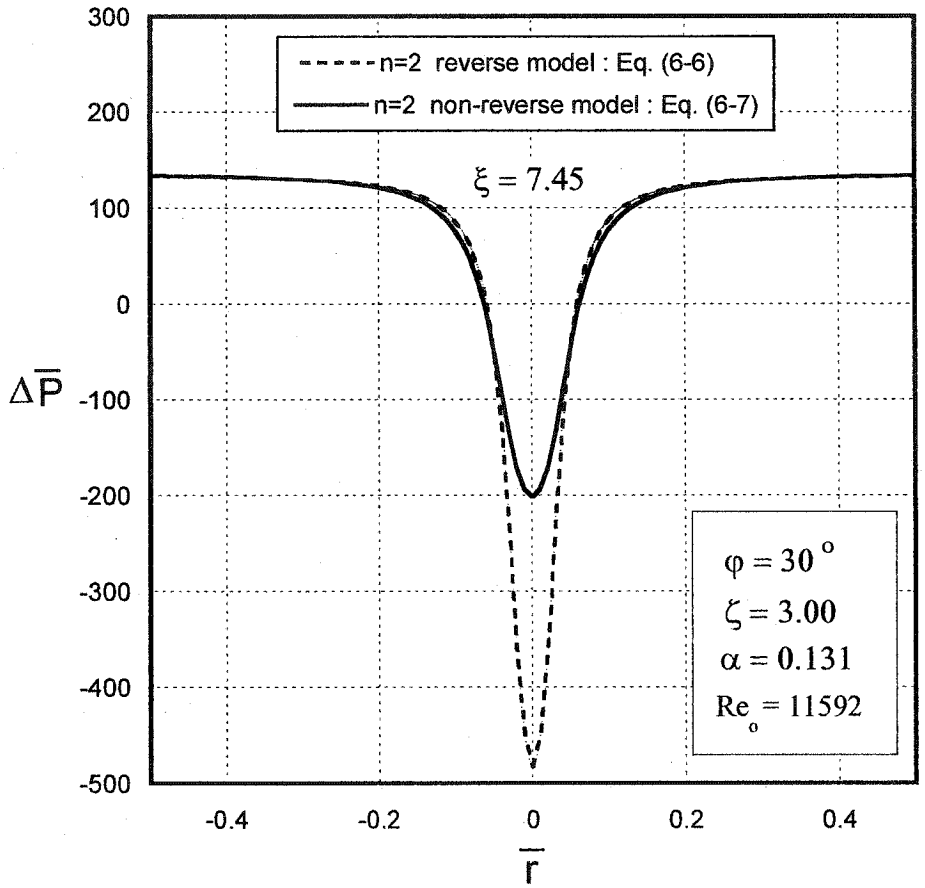

Figure (6-4-5): Comparison of radial pressure profiles for n=2 reverse and non-reverse vortex models .

6-5: Compressibility Effect

It is evident that for large ξ ratios the agreement of the theoretical pressure with the experiment becomes better. However given the chamber geometry and flow conditions the compressibility effect for free and n=2 non-reverse vortex models when

$$M_e = \frac{V_{z\,out}}{\sqrt{kRT}} = \frac{Q_{in}\,\xi^2}{A_o\sqrt{kRT}\,(1-\chi_c^2)} < 0.333$$

and for n=2 vortex model when

$$M_e = \frac{V_{z\,out}}{\sqrt{kRT}} = \frac{\gamma_2\,Q_{in}\,\xi^2}{A_o\sqrt{kRT}\,(1-\chi_c^2)} < 0.333$$

provides an upper limit for ξ beyond which the present theory is not applicable since density variations have not been taken into account. The variation of exit Mach number for the two configurations ($\varphi=20^o, \alpha=0.05$, $\zeta=3.00$) and ($\varphi=30^o$, $\alpha=0.131$, $\zeta=3.00$) as a function of ξ for three vortex models is given in figures (6-5-1) to (6-5-3). As it is anticipated the compressibility limit for $\varphi=20^o$, since the swirl effects are stronger forcing the exit area to contract, ξ_{cr} moves towards the lower values. In addition, free and n=2 reverse models posses approximately the same compressibility

limit (i.e for $\varphi=20^o$) at the critical value (ξ_{cr}) 8.4, while ξ_{cr} is 8.0 for n=2 non-reverse model which is lower than the other two models.

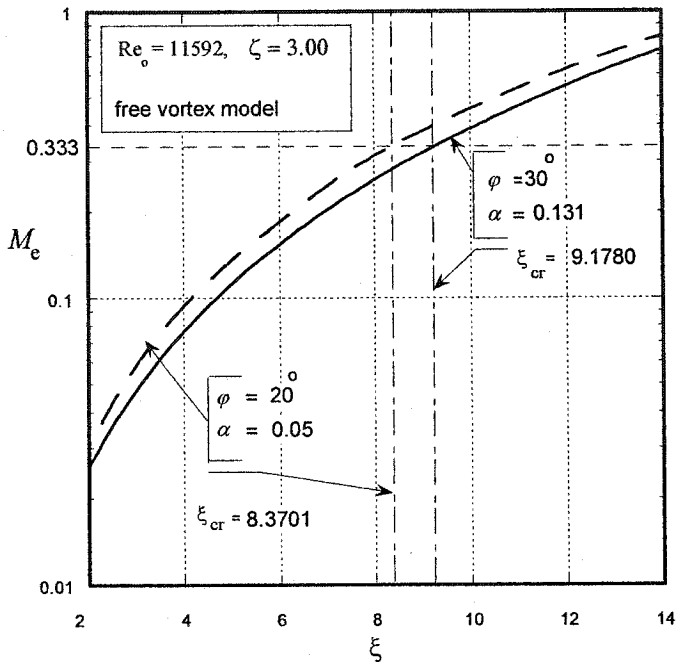

Figure (6-5-1): Compressibility effect for free vortex model.

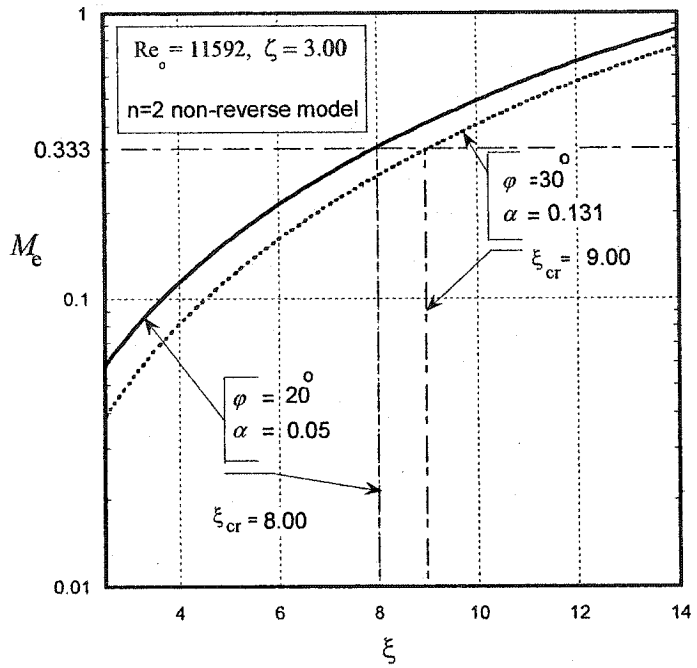

Figure (6-5-2): Compressibility effect for n=2 non-reverse vortex model.

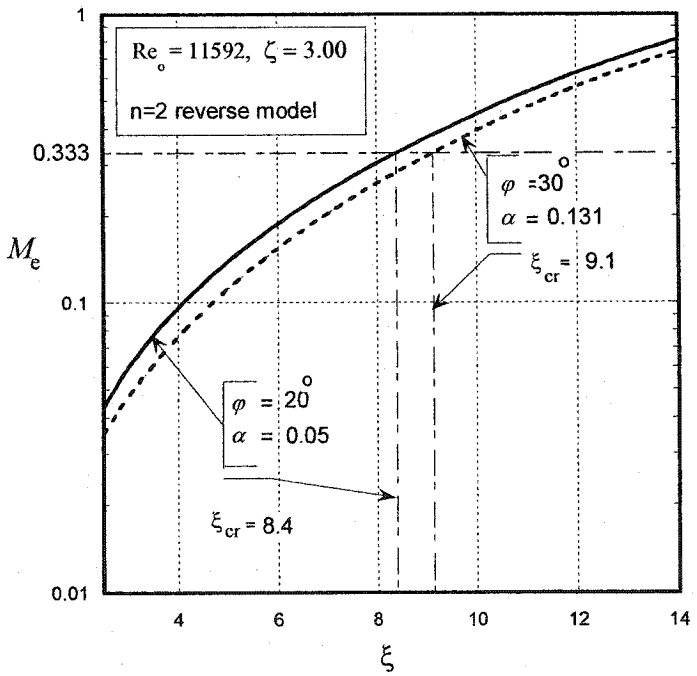

Figure (6-5-3): Compressibility effect for n=2 reverse vortex model.

Chapter 7: Conclusions and Recommendations

7-1: Conclusions

The flow in jet-driven vortex chambers over a wide range of Reynolds numbers, contraction ratios, inlet angles, area and aspect ratios was examined. The theoretical tool to investigate analytically the flow was based on the integral equations of continuity and energy, along with the minimum-pressure-drop postulate. When swirl is strong, the formulation has been found to successfully capture the main characteristics of vortex chamber flow. A parametric study gave the details of how the core size and the pressure coefficient change with each of the dimensionless groups. For longer chambers the present analysis suggests that the pressure drop coefficient is smaller than for shorter chambers. This behavior has been attributed to the controlling character of the centrifugal force. The current theoretical development has also shown the previous models, Lewellen [25] and Vatistas [26] to be only applicable for high Reynolds numbers where the inertia dominates the viscous forces.

It has been seen that increasing the Reynolds number increased the pressure drop coefficient and expanded the core size. Increasing the diameter ratio increased the pressure drop coefficient and contracted the core size. Stronger vortex will be produced by increasing the diameter ratio and/or Reynolds number, resulting in a higher tangential velocity and hence a higher pressure drop. Decreasing the aspect ratio increased the pressure drop coefficient and the core size dilated. As the aspect ratio becomes larger, the vortex decay factor decreases which leads to the damping of the tangential velocity,

leading to a weaker vortex, and therefore a smaller pressure drop. Decreasing the area ratio increased ΔP and caused a dilation of the core size. In case where the area ratio is decreased, the total inlet velocity (q_{in}) will be increased and hence the vortex strength will be stronger, and the result is more pressure drop (ΔP). Decreasing the inlet angle increased the pressure drop coefficient and expanded the core size. As the inlet angle is decreased, this means increasing the inlet tangential velocity ($V_{\varphi in}$), and thus increasing the circulation (Γ). Therefore, higher tangential velocity and hence a higher pressure drop results.

The vortex decay factor increases as the Reynolds number, area ratio, an inlet angle increases while it decreases as the aspect ratio increases. Decreasing the vortex decay factor lowers the tangential velocity, reduces the vortex strength, increases the energy dissipation and consequently reduces the pressure drop.

The n=2 vortex model for reverse flow possess the lowest axial inertial term and the highest swirl and friction terms. The n=2 for non-reverse possess the highest axial inertial term and the lowest swirl and friction terms. The free vortex model terms lie between the other two models.

Based on the present theories where the core size, circulation and vortex decay factor are given, a new approach is developed to determine the tangential velocity and radial pressure profiles inside the vortex chamber. The free vortex model gives a good result in

the free vortex zone. The n=2 vortex model for reverse flow gives better results for strong swirling flow where the reverse flow appears in the central region.

7-2: Contributions

The present experimental data and the developed mathematical models can be used in industrial applications in order to design or improve the performances of vortex devices.

The contributions of this thesis are: this work introduces experimental and theortical study of the flow in a vortex chamber over a wide range of Reynolds numbers, contraction ratios, aspect ratios, inlet angles, and area ratios.

The integral approach of continuity and energy equations, along with the minimum-pressure-drop or maximum flow rate, are used in this study to provide an analytical means to relate the non-dimensional parameters such as the chamber geometry, core size, pressure drop, Reynolds number, and viscous losses.

Both the free vortex model and the n=2 vortex model, with reverse and non-reverse flow have been used at the chamber exit plane. The effect of vortex chamber geometry, such as contraction ratio, inlet angle, area ratio, aspect ratio, and Reynolds number, on the flow field has been analyzed and compared with the present experimental data.

The observations show the pressure drop to decrease with the length. At first this appears to be counterintuitive since one habitually expects the pressure drop to be larger for longer pipes. A closer examination however, reveals that in addition to the radial-axial plane flow there is also a substantial centrifugal force, which decays with the length, thus shaping the development of the overall flow-field. The pressure drop across the vortex chamber differs from that in pipe flow, due to the mechanism of swirl flow. It depends mainly on the intensity of the tangential velocity. If the chamber length is increased, the vortex decay factor decreases, lowering the tangential velocity, which leads to less pressure drop.

A new approach to determine the tangential velocity and radial pressure profiles inside the vortex chamber is developed and compared with the available experimental data. The n=2 vortex model with reverse flow gives better results for strongly swirling flow.

References

[1] Gupta, A. K., Lilly, D. G., and Syred, N., N., Swirl Flows, Abacus, Tunbridge Wells, England, UK., 1984.

[2] Hilsch, R., "The Use of the Expansion of the Gases in a Centrifugal Field" Zeitshrift fuer Naturforschung, Vol. 1, 1946, pp. 208-214, Review of Scientific Instruments, Vol. 18, No. 2, 1947, pp. 108-113 (translation).

[3] Tanasana. Y. and K. Nakamira. "On the Vortex Combustor as Applied to the Gas Turbine". JSME-15 paper presented at the Tokyo Joint JSME-ASME International Gas Turbine Conference and Product Show, Tokyo, Japan, Cot. 4-7, 1971.

[4] Martemianov, S., and Okulov. V. L., "On Heat Transfer Enhancement in Swirl Pipe Flows", Int. J. Heat and Mass Transfer, 47, 2004, pp. 2379-2393.

[5] Martemianov, S., and Okulov. V. L., "Mass Transfer Ambiguities in Swirling Pipe Flows", J. of Applied Electrochemistry 32, 2002, pp. 25-34.

[6] Algifri, A. H, Bhardwaj, R. K, and Rao, Y.V.N. " Heat Transfer in a Turbulent Decaying Swirl Flow in a Circular Pipe" Int. J. Heat Mass Transfer 19 (1980), pp. 613-620.

[7] Legentilhomme, P., and Legrand, J., " The Effect of Inlet Conditions on Mass Transfer in Annular Swirling Decaying Flow", Int. J. Heat Mass Transfer 35 (1991), pp. 1281-1291.

[8] De Sa, M. S., Shoukry, E. and Soegiarto, I., "Mass Transfer Enhancement in the Entrance Region for Axial and Swirling Annular Flow", Canad. J. Chem. Eng. 69 (1991), pp. 294-299.

[9] Volchov, E. P., Lebedev, V. P., and Lukashov, V. V. "The LDA Study of Flow Gas-Dynamics in a Vortex Chamber", International Journal of Heat and Mass Transfer,Vol. 47, (2004) pp. 35-42.

[10] Thomson, W. (Lord Kelvin), 1880: Vibrations of a vortex column. *Phil. Mag.*, 10, 155. Also in Gray, A, and Mathews, G.B., 1922: A treatise on Bessel functions and their applications to physics. MacMillan and Co., London.

[11] Vatistas, G. H., 1990: A note on liquid vortex sloshing and Kelvin's equilibria. J. Fluid Mech., 217, 241-248.

[12] Baluev, E. D. and Troyankin, Y. V., "Study of Aerodynamic Structure of Gas Flow in a Cyclone", Thermal Engineering, Vol. 14, 1967, pp. 84-87.

[13] Georgantas, A. I., Krepec, T., and Kwok, C. K. "Vortex Flow Patterns in a Cylindrical Chamber", AIAA/ASME 4th Fluid Mechanics, Plasma Dynamics and Lasers Conference, paper no. AIAA-86-1098, Atlanta GA, May 12-14, 1986.

[14] Escudier, M.P., Bornstein, J. and Maxworthy, T., "The Dynamics of Confined Vortices", Proceedings of the Royal Society of London, Vol. A382, 1982, pp. 335-360.

[15] Mattner, T. W., Joubert, P. N., and Chong, M. S. "Vortical Flow. Part 1. Flow Through a constant Diameter Pipe", J. Fluid Mech., vol. 463, 2002, pp. 259-291.

[16] Rankine, W. J. M., Manual of Applied Mechanics, C. Griffen Co., London, 1858.

[17] Rosenhead, L., "The Spread of Vorticity in the Wake Behind a Cylinder," Proceedings of the Royal Society of London, Series A: Mathematical and Physical Sciences, Vol. 127, 1930, pp. 73-76.

[18] Burgers, J. M., "A Mathematical Model Illustrating the Theory of Turbulence," Advances in Applied Mechanics, Vol. 1, 1948, pp. 171-199.

[19] Scully, M. P., and Sullivan, J. P., "Helicopter Rotor Wake Geometry and Airloads and Development of Laser Doppler Velocimeter for Use in Helicopter Rotor Wakes," Massachusetts Institute of Technology Aerophysics Laboratory Technical Report 183, MIT DSR No. 73032, August 1972.

[20] Lamb, H., Hydrodynamics, 6th ed., Cambridge Univesity Press, Cambridge, UK, 1932.

[21] Vatistas, G., H., " New Model for Intense Self-Similar Vortices", AIAA Journal, Vol. 14, No. 4, 1998, pp. 462-469.

[22] Sullivan, R. D., "A two-Cell Vortex Solution of the Navier-Stokes Equations,"Journal of the aerospace sciences, Vol. 26, No. 11, 1959, pp.767-768.

[23] Tager, S. A., "Calculating the Aerodynamic Resistance of Cyclone Combustion Chambers". Thermal Engineering 18, No.7,pp. 120-125 (1971).

[24] Troyankin, Y.U. and E.D. Baluev, "The Aerodynamic Resistance and Efficiency of Cyclone Chamber", Thermal Engineering 16, 45-50 (1969).

[25] Lewellen, W.S., "A Review of Confined Vortex Flows", NASA Contractor Report (NASA CR-1772), July 1971.

[26] Vatistas, G. H., S.Lin and C.K. Kwork, "Theoretical and Experimental Studies on Vortex Chamber Flows", AIAA Journal, 24 No. 4, 635-642 (April 1986).

[27] Binnie, A.M. and Hookings, G.A., "Laboratory Experiments on Whirlpools", Proc. R. Soc. London. Ser. A, Vol. 194, 1948, pp. 398-415.

[28] Shakespeare, W.J. and Levy, E.K., "Pressure Drop in a Confined Vortex with High Flow Rate", Paper Presented at the Winter Annual Meeting of ASME, Chicago, Illinois, November, 1980.

[29] Vatistas, G.H., Lam, C., and Lin, S., "Similarity Relationship for the Core Radius and the Pressure Drop in Vortex Chambers", Canadian Chemical Engineering Journal , Vol. 67, August 1989, p. 540.

[30] Vatistas, G., H., Kwork C., K, Lin, S, "The Reduction of Pressure Drop Across a Vortex Chamber", AIAA Journal, Vol. 23, No. 6, 1985, pp. 974.

[31] Vatistas, G. H. and Sakaris, P., "Pressure Drop Across a Double-Oulet Vortex Chamber", AIAA, JPP, Journal, 17 No. 3, 711-716 (October 2000).

[32] Vyas. B and J. Majdalani, "The Bidirectional Vortex. Part 2: Viscous Core Corrections", 39 AIAA Conference and Exhibit, 20-23 July, 2003.

[33] Li, H, and Tomita, Y.," Characteristics of Swirling Flow in a Circular Pipe" Transactions of ASME, J. of Fluids Engineering, Vol. 116, 1994, pp. 370-373.

[34] Yang, Z., Y. and Priestman, G., H., "Internal Flow Modelling of Vortex Throttles" Proc. Instn. Mech. Engrs, Vol. 205. 1991, pp. 405-413.

[35] Escudier, M. P., Bornstein, J., and Zehender, N., "Obsevations and LDA Measurements of Confined Turbulent Vortex Flow," Journal of Fluid Mechanics, Vol. 98, pt.1, 1980, pp. 49-63.

[36] Kreith, F., and Sonju, O.,K. "The Decay of a Turbulent Swirl in a Pipe", Journal of Fluid Mechanics, vol. 22, part 2, 1965, pp. 257-271.

[37] Chang, F., and Dhir, V., K. "Turbulent Flow Field in Tangentially Injected Swirl Flows in Tubes", Int. J. Heat and Fluid Flow, vol. 15, No. 5, October 1994, pp. 346-356.

[38] Darmofal, D., L., Khan, R., Greitzer, E., M., and Tan, C., S., "Vortex Core Behaviour in Confined and Unconfined Geometries: a Quasi-One-Dimensional Model", Journal of Fluid Mechanics, vol. 449, 2001, pp. 61-84.

[39] Escudier, M. "Estimation of Pressure Loss in Ring-Type Exit Chamber", Trans. ASME I, J. Fluid Engng 101, 1979,pp 511-516

[40] Escudier, M. P., and Merkli, P. "Observations of the Oscillatory Behaviour of a Confined Ring Vortex", AIAA Journal, vol. 17, No. 3, March 1979, pp. 253-260.

[41] Lam, H. C., "An Experimental Investigation and Dimensional Analysis of Confined Vortex Flows" Ph.D. Thesis, Department of Mechanical Engineering, Concordia University, 1455 DeMaisonneuve Blvd. West, Montreal, Canada, 1993.

[42] Alekseenko, S. V., Kuibin, P. A., Okulov, V. L., and Shtork, S. I., " Helical Vortices in Swirl Flow", J. Fluid Mech., vol. 382, 1999, pp. 195-243.

[43] Love, W., J., "Prediction of Pressure Drop in Straight Vortex Tubes", AIAA Journal, vol. 12, No. 7, July 1974, pp. 959-965.

[44] Osami, K., "Experimental Study of Turbulent Swirling Flow in a Straight pipe", Journal of Fluid Mechanic, vol. 225, 1991, pp. 445-479.

[45] Steenbergen, W., and Voskamp, J. "The Rate of Decay of Swirl in Turbulent Flow", Flow Measurement and Instrumentation 9, 1998, 67-78.

[46] Nejad, A. S., S. P. Vanka, S. C. Favaloro, M. Samimy and C. Langenfeld, "Application of Laser Velocimetry for Characterization of Confined Swirling Flow", Transactions of the ASME, Journal of Engineering for Gas Turbines and Power, Vol. 111, Jan.,1989, pp. 36-45.

[47] Jakirlic, S., K. Hanjalic, C. Tropea, "Modeling Rotating and Swirling Turbulent Flows: A Perpetual Challenge", AIAA Journal, Vol. 40, No. 10, Oct. 2002, pp. 1984-1996.

[48] Orland, P and M. Fatica, "Direct Simulation of Turbulent Flow In a Pipe Rotating About Its Axis", J. Fluid Mech.,Vol. 343, 1997, pp. 43-72.

[49] Jones, W. P. and Pascau A. "Calculation of Confined Swirling Flows with a Second Momentum Closure", Transaction of the ASME, vol. 111, sep. 1989, pp. 248-255.

[50] Hoekstra, A. J., Derksen, H. E. A. and Akker, V. D. "An Experimental and Numerical Study of Turbulent Swirling Flow in Gas Cyclones", Chemical Engineering Science 54, 1999, pp. 2055-2065.

[51] Ivanov, " Increasing the Rate of Heat Transfer in a Round Air-Cooled Tube" Proceeding Second All-soviet Union Conference on Heat and Mass Transfer, Minsk, vol. 1, 1964, pp. 243-250.

[52] Chang, F., Dhir, V. K., "Mechanism of Heat Transfer Enhancement and Slow Decay of Swirl in Tubes using Tangential Injection", Int. J. Heat Fluid Flow 16 (2), 1995, pp. 78-87.

[53] Blum, F. A., Oliver, L.R. "Heat Transfer in Decaying Vortex System", ASME Paper no. 66-WA/HT- 62, 1975.

[54] Zaherzade, N. H., Jagadish, B. S., "Heat Transfer in Decaying Swirl Flow", Int. J. Heat Mass Transfer 18, 1975, pp. 941-944.

[55] Yilmaz, M., Yapici, S., Jomakli, O., and Sara, O. N., "Energy Correlation of Heat Transfer and Enhancement Efficiency in Decaying Swirl Flow", Heat Mass Transfer 38, 2002, pp. 351-358.

[56] Vatistas, G. H., Kozel, V., and Mih, W. C., "A Simpler Model for Concentrated Vortices," Experiments in Fluids, Vol., 11, 1991, pp. 73-76.

[57] Jacquin. L. and Pantano, C., "On the Persistence of Trailing Vortices", JFM, Vol. 471, 2002, pp.159-168.

[58] Han, Y.Q., Leishman, J.G., and Coyone, A.J., Measurements of the Velocity and Turbulence Structure of a Rotor Tip Vortex, AIAA J., Vol. 35, (3), March 1997, pp. 477- 485.

[59] Faler, J.H., and Leibovich, S., Disturbed States of Vortex Flow and Vortex Breakdown, Physics Fluids, Vol. 20, 1977, pp. 1385-1400.

[60] Yan, L., Vatistas, G.H., and Lin, S. "Experimental Studies on Turbulence Kinetic Energy in Confined Vortex Flows", Journal of Thermal Science, vol. 9, No. 1, March 2000, pp. 10-22.